

# THESIS CONTENTS

ABSTRACT.....	1
RÉSUMÉ.....	4
ACKNOWLEDGEMENTS.....	7
THESIS CONTENTS .....	9
FIGURE CONTENTS .....	12
TABLE CONTENTS.....	18
EQUATION CONTENTS.....	19
1. Introduction.....	20
1.1 Introduction.....	20
1.2 Definition of problem .....	23
1.3 Objectives .....	24
1.4 Methodology.....	25
Reference .....	25
2. Literature review.....	28
2.1 Fabrication of superhydrophobic coatings.....	28
2.1.1 Sol-gel process .....	28
2.1.2 Electrochemical deposition.....	29
2.2 Self-assembled monolayers (SAM).....	30
2.2.1 Preparation of SAM.....	31
2.2.2 Characterization and analysis of SAM .....	33
2.2.3 Important factors about SAM .....	34
2.3 Durable superhydrophobic coatings .....	35
2.3.1 Mechanical durability .....	36
2.3.2 UV durability .....	46
2.3.3 Thermal durability .....	56
2.3.4 Chemical durability.....	59
Reference .....	64

3. Experimental .....	69
3.1 Materials .....	69
3.2 Sample preparation .....	69
3.2.1 Fabrication of superhydrophobic cobalt stearate thin films by electrodeposition .....	69
3.2.2 Fabrication of superhydrophobic films incorporating TiO <sub>2</sub> nanoparticles by sol-gel process.....	70
3.2.3 SAM modified aluminum substrates for improved adhesion properties .....	72
3.3 Characterization: Wettability, Topography, Morphology and Structure, Chemical composition, Corrosion behavior analysis and UV degradation behavior analysis.....	73
4. Corrosion resistant superhydrophobic cobalt stearate thin films coated aluminum alloys by electrodeposition .....	80
4.1 Introduction.....	80
4.2 Experimental .....	84
4.3 Results and discussion .....	86
4.3.1 Surface morphology and wetting .....	86
4.3.2 Surface composition.....	90
4.3.3 Surface wettability .....	99
4.3.4. Mechanism.....	103
4.3.5 Corrosion resistance properties.....	107
4.4 Summary .....	123
Reference .....	124
5. Ultra-Violet durable superhydrophobic thin films coated aluminum alloys .....	128
5.1 UV durable superhydrophobic cobalt stearate thin films prepared by one-step electrodeposition .....	128
5.1.1 Introduction.....	128
5.1.2 Experimental .....	130
5.1.3 Results and discussions.....	131

5.1.4 Summary .....	134
5.2 UV durable PMHS/TiO <sub>2</sub> @CoSA superhydrophobic coatings by sol-gel/spin-coating process.....	135
5.2.1 Introduction.....	135
5.2.2 Experimental .....	138
5.2.3 Results and discussions.....	139
5.2.4 Summary .....	150
Reference .....	150
6. Superhydrophobic thin films applied on SAM modified aluminum substrates.....	154
6.1 Electrochemical impedance spectroscopy (EIS) studies of self-assembled monolayers (SAM) on aluminum substrates.....	154
6.1.1 Introduction.....	154
6.1.2 Experimental .....	156
6.1.3 Results and discussion .....	157
6.1.4 Summary .....	163
6.2 Mechanical durability test of superhydrophobic coatings on SAM modified aluminum substrates.....	164
Reference .....	166
7. Conclusions.....	169
8. Recommendations.....	172
9. Publications & Awards .....	173

# FIGURE CONTENTS

Figure 1. 1 The water drop in equilibrium state on a solid surface [2].....	20
Figure 1. 2 Superhydrophobic phenomena in nature [4, 5, 8] .....	21
Figure 2. 1 The scheme for different bonding modes of SAM with APTES [12]	30
Figure 2. 2 Two methods of making a SAM [13] .....	32
Figure 2. 3 Cross-hatch tape adhesion test for coatings with 10–20 nm silica fillers. (a-c) Hydrophobic surface and (d) superhydrophobic surface [31].....	39
Figure 2. 4 Images of the grid area of a sample before (a) and after (b) Cross-hatch tape adhesion test [32] .....	39
Figure 2. 5 Schematic illustration of adhesion strength test [33] .....	40
Figure 2. 6 Schematic diagram of the abrasion test equipment with sand paper used as an abrasive surface [34].....	41
Figure 2. 7 (a) Contact angle and sliding angle on the coating as a function of abrasion length; SEM images for the coating after abrasion length of (b) 400mm .....	42
Figure 2. 8 Contact angle and sliding angle on the metal/polymer composite surface as a function of abrasion cycles [35].....	43
Figure 2. 9 Contact angle and sliding angle on PTFE/PVDF composite surfaces as a function of abrasion cycles [36].....	44
Figure 2. 10 Image for pencil hardness test .....	45
Figure 2. 11 Solar radiation spectrum.....	47
Figure 2. 12 Photographs of water droplet shape on TiO <sub>2</sub> coatings before (left) and after (right) UV illumination for 6h [42] .....	48
Figure 2. 13 Reversible super-hydrophobic-super-hydrophilic transition of the as- prepared films under the alternation of UV irradiation and dark storage [43] .....	50
Figure 2. 14 UV stability of a PFOS-treated rough silica thin film [40] .....	51

Figure 2. 15 Changes of WCAs of the superhydrophobic coatings with different TiO <sub>2</sub> contents under QUV accelerated weathering test [45] .....	52
Figure 2. 16 Evolution of water CA on OTS-modified ZnO NW array (squares) and OTS-modified ZnO@SiO <sub>2</sub> NW array (triangles) under UV irradiation[49] .	53
Figure 2. 17 Photo degradation process of PTES based superhydrophobic surface [47].....	54
Figure 2. 18 Contact angles of three different layers of SiO <sub>2</sub> on the top of TiO <sub>2</sub> (P25)*3 coated superhydrophobic samples after certain periods of time [47] .....	55
Figure 2. 19 Contact angle as a function of temperature for organically silica coatings (black) before (blue) after modified by TMCS [53].....	57
Figure 2. 20 (a) Water contact angle plotted against the thermal treatment temperature; (b) the SEM images of FPI and PS samples before and after heating at 150 °C [56] .....	58
Figure 2. 21 Model for the anticorrosion mechanism[57] .....	60
Figure 2. 22 (a) Potentiodynamic polarization curves, (b) Nyquist plots and (c) Bode plots of the bare Al alloy substrate and the as-prepared superhydrophobic surface measured in 3.5 w.t.% NaCl solution [63] .....	62
Figure 2. 23 Typical electrical equivalent circuits used for superhydrophobic surfaces [64].....	63
Figure 3. 1 The schematic model for preparation of cobalt stearate (CoSA) by electrodeposition .....	70
Figure 3. 2 Photograph of Single Wafer Spin Processor.....	71
Figure 3. 3 The Schematic diagram of a self-assembled monolayer of GPTS .....	72
Figure 3. 4 Photograph of contact angle goniometer .....	74
Figure 3. 5 Photograph of 3D surface optical profilometer .....	74
Figure 3. 6 Photograph of scanning electron microscope.....	75
Figure 3. 7 Photograph of image analysis system.....	76
Figure 3. 8 Photograph of Attenuated Total Reflectance system .....	76

Figure 3. 9 Photograph of X-ray diffraction system .....	77
Figure 3. 10 Photograph of corrosion test.....	78
Figure 3. 11 Photograph of UV degradation test .....	78
Figure 3. 12 Photograph of UV-Vis spectroscopy .....	79
Figure 4. 1 SEM images (left column) of (a) as-received aluminum substrate and electrodeposited cathodic aluminum substrates with the application of 10V DC voltage for 10 min in the Co (II)/SA ethanolic solution with molar ratios of (c) 0, (e) 0.02, (g) 0.08, (i) 0.2, (k) 0.5 and (m) $\infty$ . The insets show the images of water drops on respective surfaces. The molar ratio $\infty$ represents a pure solution of Co(II) ions in ethanolic solution having concentration of 0.01 M. The SEM images (right column) in high magnification (b), (d), (f), (h), (j), (l), (n) correspond to those at lower magnification in the left column .....	87
Figure 4. 2 EDS spectra of different areas on the aluminum substrate modified by electrodeposition in the mixed ethanolic solution with a Co/SA molar ratio of 0.5: (a) area 1: the gray honeycomb-like framework, (b) area 2: the white clusters .....	91
Figure 4. 3 (a) low angle XRD patterns of (I) As-received aluminum, (II) 0.08/Al for 10min, (III) 0.08/Al for 60min, and (IV) Cobalt stearate drop films on aluminum substrates; (b) shows the corresponding high angle XRD patterns of (a).....	93
Figure 4. 4 (a) shows FTIR spectra of (I) as-received aluminum substrate and (III) solid stearic acid, as well as chemically modified aluminum substrates by electrodeposition in ethanolic solution with a Co/SA molar ratio of (II) 0, (IV) 0.08, (V) 0.2, (VI) 0.5; (b) compares the FTIR spectra of chemically modified aluminum substrates by electrodeposition in ethanolic solution with a Co/SA molar ratio of (I) $\infty$ , (III) 0.5 and (II) aluminum substrates dropcoated with pure cobalt stearate .....	95
Figure 4. 5 The variation in the area under (a) the hydrocarbon (-CH <sub>2</sub> and -CH <sub>3</sub> ) peaks, (b) the cobalt oxide (Co-O) peaks at the right end as a function of the	

molar ratio of Co/SA in the electrolytes; The curve (c) depicts the calculation results of (a)/(b) by peak area .....	97
Figure 4. 6 (a) Surface roughness (b) and water contact angle as well as contact angle hysteresis of as-received aluminum substrate and electrochemically modified cathodic aluminum substrates with the application of 10V DC voltage for 10 min in varied molar ratios of Co/SA ethanolic solution .....	99
Figure 4. 7 (a) Potentiodynamic polarization curves; (b) Polarization resistance; (c) Corrosion current density of as-received aluminum, and thin films prepared from a cobalt nitrite and stearic acid mixed solution with Co/SA molar ratios of 0.08, 0.2, 0.5 as well as electrodeposited films in a pure solution of stearic acid (i.e. Co/SA=0) and cobalt nitrite (i.e. Co/SA= $\infty$ ), respectively .....	108
Figure 4. 8 (a) The current-potential (I-E) curves obtained from the potential variation of $\pm 15$ mV around the corresponding corrosion potential ( $E_{\text{corr}}$ ) for the $R_p$ calculated by ohm's law; (b) the $R_p$ value calculated by ohm's law ( $R_{p1}$ ) versus by Stern-Geary equation ( $R_{p2}$ ) .....	113
Figure 4. 9 (a) The corrosion potentials ( $E_{\text{corr}}$ , black) and open circuit potentials (OCP, blue) for thin films samples Potentiodynamic polarization curves of (1) as-received aluminum, and thin films prepared from a cobalt nitrite and stearic acid mixed solution with Co/SA molar ratios of (3) 0.08, (4) 0.2, (5) 0.5 as well as electrodeposited films in a pure solution of (2) stearic acid and (6) cobalt nitrite, respectively. A horizontal dotted line has been plotted at -700 mV to guide the eyes. (b) $E_{\text{corr}}$ obtained from Stern-Geary equation versus OCP stabilized in 3.5 w.t.% sodium chloride solution for 24h.....	114
Figure 4. 10 (a)Nyquist plots (b) Bode modulus diagrams and (c) Bode phase angle diagrams of superhydrophobic thin films electrodeposited on Al from Co/SA molar ratio of 0.2 and as-received aluminum substrate. (d) Electrical equivalent circuits employed to simulate the EIS study of (d1) as-received aluminum and (d2) superhydrophobic thin films electrodeposited on Al from Co/SA molar ratio of 0.2. The inset image shows the amplified diagram in the higher frequency range .....	117

Figure 5. 1 Water contact angle (black square) and contact angle hysteresis (blue dot) on the surface of the electrodeposited cobalt stearate film as a function of UV irradiation time .....	131
Figure 5. 2 SEM images of electrodeposited cobalt stearate film (a) before and (b) after UV degradation for 60 days. The insets show the water drop on the corresponding surfaces.....	133
Figure 5. 3 ATR-FTIR spectra of (a) stearic acid powder; the electrodeposited cobalt stearate film (b) before and (c) after UV degradation for 60 days....	134
Figure 5. 4 (a) Low angle XRD patterns of (I) stearic acid powder and (II) cobalt stearate films on aluminum substrates; (b) ATR-FTIR spectra of (I) stearic acid powder and (II) cobalt stearate drop films on aluminum substrates. The inset figure in (a) shows the corresponding UV-Vis absorption spectrum of cobalt stearate .....	140
Figure 5. 5 (a) The variation of water contact angle on PMHS/TiO <sub>2</sub> and PMHS/TiO <sub>2</sub> @CoSA superhydrophobic thin films as a function of UV irradiation time. The inset images in (a) show the water drop on the corresponding surfaces respectively; (b) ATR-FTIR spectra of (I) PMHS liquid and (II) PMHS/TiO <sub>2</sub> @CoSA superhydrophobic thin films. The inset figure in (b) shows the amplificative ATR-FTIR spectra in the range from 3050 cm <sup>-1</sup> to 2750 cm <sup>-1</sup> ; (c) XRD patterns of (I) aluminum substrates (II) PMHS/TiO <sub>2</sub> and (III) PMHS/TiO <sub>2</sub> @CoSA; (d) EDS spectra of (d-I) PMHS/TiO <sub>2</sub> @CoSA and (d-II) PMHS/TiO <sub>2</sub> .....	143
Figure 5. 6 (a) SEM image and (b) The schematic model for the PMHS/TiO <sub>2</sub> @CoSA coatings on aluminum substrate. The inset image in (a) shows water drops on this superhydrophobic surface.....	147
Figure 6. 1 Left-top shows the GPTS molecule, left-down shows the self-assembled monolayer (SAM) of GPTS on Al substrate. Right of Figure 6.1 shows ATR-FTIR spectra of (a) pure GPTS organosilanes (b) SAM of GPTS on aluminum	



substrate (SAM/Al) and (c) Al substrate.....	157
Figure 6. 2 SEM images of (a) Al and (c) SAM/Al substrate; EDX spectra of (b) Al and (d) SAM/Al substrate .....	159
Figure 6. 3 (a-c) Nyquist plots for Al and SAM/Al substrates after immersion time in 10 <sup>-4</sup> M NaOH aqueous solution of 2, 4, 6, 8, 10h respectively; (d) Charge transfer resistance ( $R_{ct}$ ) of Al and SAM/Al substrates as functions of immersion time; (e) Electrical equivalent circuit model used for fitting of EIS dates of Al and SAM/Al substrates; (f) The variation of open circuit potential (OCP) with immersion time for Al and SAM/Al substrates .....	161
Figure 6. 4 Potentiodynamic polarization curves of Al and SAM/Al substrates after 10 h immersion time in 10 <sup>-4</sup> M NaOH aqueous solution.....	162
Figure 6. 5 Optical photographs of superhydrophobic PMHS/TiO <sub>2</sub> coatings on as-received aluminum substrates (a) before and (b) after adhesive tape tests; on SAM modified aluminum substrates (c) before and (d) after adhesive tape tests .....	164

# TABLE CONTENTS

Table 2. 1 Some important factors of SAMs [12, 14-19].....	34
Table 2. 2 Classification of test results .....	37
Table 4. 1 The EDS results of atomic element percentages for different areas on the aluminum substrate modified by electrodeposition in the mixed ethanolic solution with a Co/SA molar ratio of 0.5 .....	92
Table 4. 2 The open circuit potential (OCP), corrosion potential ( $E_{\text{corr}}$ ), current density ( $I_{\text{corr}}$ ) and polarization resistance ( $R_p$ ) for aluminum substrates electrodeposited in the solution of varied molar ratio of Co/SA .....	110
Table 4. 3 Electrochemical parameters obtained from electrical equivalent circuits (EEC), fitted EIS data of as-received aluminum and superhydrophobic thin films on Al substrates in 3.5 w.t. % NaCl solution .....	118
Table 6. 1 Results of EIS and potentiodynamic polarization of Al and SAM/Al substrates after the immersion time of 10 hrs in $10^{-4}$ M NaOH solution.....	163

# EQUATION CONTENTS

$\cos \theta = \frac{\gamma_{SV} - \gamma_{SL}}{\gamma_{LV}}$	(1.1).....	20
$\cos \theta_w = r \cos \theta_1$	(1.2).....	22
$\cos \theta_c = f_1(\cos \theta_1 + 1) - 1$	(1.3).....	22
$Z_{CPE} = \frac{1}{Y_0(j\omega)^n}$	(2.1) .....	63
$Z = Z_{real} + j Z_{imaginary}$	(4.1).....	86
$Z = Z' + j Z''$	(4.2) .....	86
$ Z  = \sqrt{Z'^2 + Z''^2}$	(4.3).....	86
$\varphi = \arctan \left( \frac{ Z_{imaginary} }{Z_{real}} \right)$	(4.4).....	86
$\cos \theta_w = r \cos \theta_1$	(4.5).....	101
$\cos \theta_c = f_1(\cos \theta_1 + 1) - 1$	(4.6).....	102
$\text{Co}^{2+} + 2\text{CH}_3(\text{CH}_2)_{16}\text{COOH} \rightarrow \text{Co}[\text{CH}_3(\text{CH}_2)_{16}\text{COO}]_2 + 2\text{H}^+$	(4.7.1).....	104
$2\text{H}^+ + 2\text{e}^- \rightarrow \text{H}_2$	(4.7.2).....	104
$\text{Co}^{2+} + 2\text{H}_2\text{O} \rightarrow \text{Co}(\text{OH})_2 + 2\text{H}^+$	(4.8.1).....	104
$\text{Co}(\text{OH})_2 \rightarrow \text{CoO}_x + \text{H}_2\text{O}$	(4.8.2) .....	104
$2\text{H}^+ + 2\text{e}^- \rightarrow \text{H}_2$	(4.8.3).....	104
$R_p = \frac{\beta_a \beta_c}{2.3 I_{corr}(\beta_a + \beta_c)}$	(4.9).....	109
$R_p = \frac{\Delta E}{\Delta I}$	(4.10) .....	113
$Z_{CPE} = \frac{1}{Y_0(j\omega)^n}$	(4.11) .....	121
$\eta = \frac{R_{ct} - R_{ct0}}{R_{ct}} \times 100\%$	(4.12) .....	122
$n\lambda = 2d \sin \theta$	(5.1) .....	141
$R_p = \frac{\beta_a \beta_c}{2.3 I_{corr}(\beta_a + \beta_c)}$	(6.1).....	162

# 1. Introduction

## 1.1 Introduction

Wettability of a solid surface is a macroscopic representation of the interaction between the liquid and the substrate solid material [1]. The wettability is usually expressed by the contact angle  $\theta$  (CA,  $\theta$ ) of a water droplet resting on a solid surface, which is given by Young's equation [2]:

$$\cos \theta = \frac{\gamma_{SV} - \gamma_{SL}}{\gamma_{LV}} \quad (1.1)$$

where  $\gamma_{SV}$ ,  $\gamma_{SL}$  and  $\gamma_{LV}$  refer to the interfacial surface tensions with S, L, and V as solid, liquid, and gas, respectively, as shown in Figure 1.1.

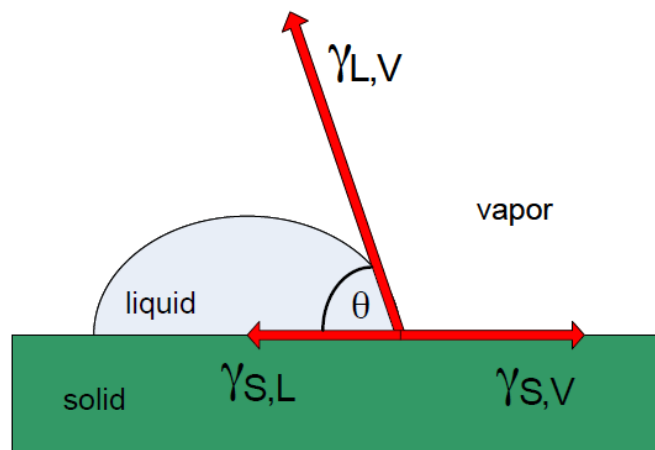


Figure 1. 1 The water drop in equilibrium state on a solid surface [2]

In addition, dynamic contact angles are measured during the growth (advancing

CA,  $\theta_a$ ) and shrinkage (receding CA,  $\theta_r$ ) of a water droplet. The difference between  $\theta_a$  and  $\theta_r$  is defined as contact angle hysteresis [3]. Depending on the value of the static contact angle, the surface properties are determined as hydrophilic ( $CA < 90^\circ$ ) or hydrophobic ( $CA > 90^\circ$ ). When the contact angle of a water droplet resting on the solid surface is greater than  $150^\circ$  and the contact angle hysteresis (CAH) is smaller than  $5-10^\circ$ , we define the surface as a superhydrophobic surface [3].

Many plants and animals show water-repellent properties with fine microstructures, such as the lotus leaf, water skippers and butterfly wings, as shown in figure 1.2 [3-5]. Those superhydrophobic surfaces in nature are dominated by micro-nano topography as well as low surface energy coatings. Inspired by the “lotus effect”, biomimetic superhydrophobic surfaces have been fabricated using various approaches. Techniques to fabricate superhydrophobic surfaces can be generally divided into two categories: making a rough surface from a low surface energy material and modifying a rough surface with a material of low surface energy [6, 7].

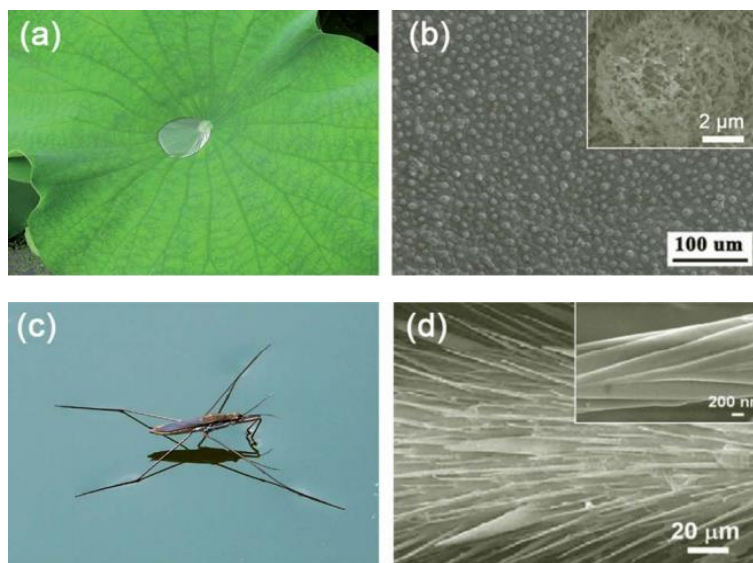


Figure 1. 2 Superhydrophobic phenomena in nature [4, 5, 8]

To understand the mechanism of superhydrophobic phenomena from a theoretical viewpoint, two classical models, namely Wenzel mode[9] and Cassie–Baxter model[10], have been established to illustrate the special wettability. The Wenzel equation is written as[9]:

$$\cos\theta_w = r \cos\theta_1 \quad (1.2)$$

where  $\theta_w$  and  $\theta_1$  are the contact angle of water drop on a rough and smooth surface respectively, having the same surface composition; and roughness factor ‘r’ is defined as the ratio of the true (on rough surfaces) and apparent (smooth) surface areas and therefore is always a positive number and ‘r’ > 1. In the Wenzel model, (i) when the true water contact angle  $\theta_1$  on a smooth surface is less than 90°, the apparent contact angle  $\theta_w$  will be less than the true contact angle  $\theta_1$  on a rough surface, and (ii) when the true contact angle  $\theta_1$  is larger than 90°, the apparent contact angle  $\theta_w$  will be greater than the true contact angle  $\theta_1$  on a rough surface.

However, in the Cassie–Baxter model, the water contact angle is determined by the composite structure of solid cobalt stearate films and the trapped air in the framework structure. The Cassie–Baxter equation is written as[10]:

$$\cos\theta_c = f_1(\cos\theta_1 + 1) - 1 \quad (1.3)$$

where  $\theta_c$  and  $\theta_1$  are the contact angle of water drop on a rough and smooth surface

respectively,  $f_1$  is the fraction of solid surface in contact with water drop.

## 1.2 Definition of problem

It is well-known that the basis of the so-called “Lotus-effect” which depicts the self-cleaning effect is caused by the presence of a rough micro-nanostructure covered with waxy materials with a high degree of resistance to wetting, resulting in a water contact angle slightly above 150 [11]. Inspired from nature, usually, the superhydrophobic surface is composed of two part: (i) optimum roughness (ii) passivation with a low-surface-energy coating.

During the past decades, there have been many ways created to prepare superhydrophobic surfaces, such as lithography and templating techniques [8, 12], plasma treatment of the surface [13], self-assembly and self-organization[14, 15], chemical bath deposition (CBD) and chemical vapor deposition (CVD)[16, 17]. Most of these methods involve rather strict conditions such as harsh chemical treatment, expensive materials ((e.g., fluoroalkylsilanes[18] and nanotubes[19]), and complex processing procedures, which are not appropriate to achieve large-scale applications in industry. Compared to these methods, electrodeposition[20, 21] and sol-gel[22] are facile, convenient and easier to handle. Moreover, even though various superhydrophobic films have fabricated using different techniques, most of them were found vulnerable to environmental attack such as chemical corrosion, mechanical scratch, ultraviolet(UV) irradiation and high temperature[23-26]. Recently, a lot of papers have been published on inhibiting corrosion behavior on metallic substrates,

which is regarded as one of the most important applications of superhydrophobic surfaces. For example, Ying *et al.*[27] has studied the corrosion resistance properties of superhydrophobic copper surface fabricated by electrochemical deposition. Superhydrophobic coatings with the properties of resisting UV degradation and mechanical scratching are two tough problems hindering the large-scale application of superhydrophobic surfaces in industry. Keeping these applications in mind, the principal objective of this research project is to fabricate durable superhydrophobic coatings on aluminum substrates.

The project will add a supplement to the various other methods of making a durable superhydrophobic coating from the perspective of chemical corrosion, mechanical scratch and UV resistance properties.

### **1.3 Objectives**

- Fabricate superhydrophobic surfaces on aluminum substrates by electrochemical process and improve the corrosion resistance properties of aluminum substrates
- Fabricate superhydrophobic coatings by sol-gel process and develop UV-durable superhydrophobic coatings on aluminum substrate.
- Prepare self-assembled monolayer (SAM) on aluminum substrates and improve the adhesion force between the superhydrophobic coatings and aluminum substrate.



## 1.4 Methodology

- Inorganic-Organic superhydrophobic coatings will be fabricated using an inorganic salt ( $\text{Co}(\text{NO}_3)_2 \cdot 6\text{H}_2\text{O}$ ) and organic acid ( $\text{CH}_3(\text{CH}_2)_{16}\text{COOH}$ ) by electrochemical process. The chemical durability of superhydrophobic coatings will be evaluated by their corrosion behavior in 3.5 w.t. % NaCl aqueous solution.
- Sol-gel process will be utilized to incorporate  $\text{TiO}_2$  nanoparticles with polymethylhydrosiloxane (PMHS) to fabricate superhydrophobic coatings. Additionally, cobalt stearate will also be incorporated into the sol-gel mixture to fabricate superhydrophobic coatings. The UV durability of superhydrophobic coatings will be evaluated in a UV chamber containing two UV lamps with the wavelengths of 302 nm and 365 nm.
- The aluminum substrates will be modified with (3-Glycidyloxypropyl) trimethoxysilan (GPTS) before the deposition of the coatings. SAMs will be used as binders between the substrates and the coatings to enhance the mechanical durability of the coatings. The adhesion test will follow the American Standard Test Method (ASTM) D 3359-02.

## Reference

- [1] Sun T. Bioinspired Surfaces with special wettability. *Acc Chem Res.* 2005;38:644-52.
- [2] Young T. An Essay on the Cohesion of Fluids. *Philosophical Transactions of the Royal Society of London.* 1805;95:65-87.
- [3] Li XM, Reinhoudt D, Crego-Calama M. What do we need for a superhydrophobic surface? A review on the recent progress in the preparation of superhydrophobic surfaces. *Chemical Society reviews.* 2007;36:1350-68.
- [4] Wang G, Guo Z, Liu W. Interfacial Effects of Superhydrophobic Plant Surfaces: A Review. *Journal of*

- Bionic Engineering. 2014;11:325-45.
- [5] Feng X, Zheng Q. Superior Water Repellency of Water Strider Legs with Hierarchical Structures: Experiments and Analysis. *Langmuir*. 2007;23:4892-6.
- [6] Huang Y, Sarkar DK, Chen XG. A one-step process to engineer superhydrophobic copper surfaces. *Materials Letters*. 2010;64:2722-4.
- [7] Ma M, Hill RM. Superhydrophobic surfaces. *Current Opinion in Colloid & Interface Science*. 2006;11:193-202.
- [8] Yan YY, Gao N, Barthlott W. Mimicking natural superhydrophobic surfaces and grasping the wetting process: a review on recent progress in preparing superhydrophobic surfaces. *Advances in colloid and interface science*. 2011;169:80-105.
- [9] Wenzel RN. RESISTANCE OF SOLID SURFACES TO WETTING BY WATER. *Industrial & Engineering Chemistry*. 1936;28:988-94.
- [10] Cassie ABD, Baxter S. Wettability of porous surfaces. *Transactions of the Faraday Society*. 1944;40:546-51.
- [11] Valipour M N, Birjandi FC, Sargolzaei J. Super-non-wettable surfaces: A review. *Colloids and Surfaces A: Physicochemical and Engineering Aspects*. 2014;448:93-106.
- [12] Sas I, Gorga RE, Joines JA, Thoney KA. Literature review on superhydrophobic self-cleaning surfaces produced by electrospinning. *Journal of Polymer Science Part B: Polymer Physics*. 2012;50:824-45.
- [13] Balamurali Balu VB. Fabrication of "Roll-off" and "Sticky" Superhydrophobic Cellulose Surfaces via Plasma Processing. *Langmuir*. 2008;24:4785-90.
- [14] Pan C, Shen L, Shang S, Xing Y. Preparation of superhydrophobic and UV blocking cotton fabric via sol-gel method and self-assembly. *Applied Surface Science*. 2012;259:110-7.
- [15] Cho WK, Park S, Jon S, Choi IS. Water-repellent coating: formation of polymeric self-assembled monolayers on nanostructured surfaces. *Nanotechnology*. 2007;18:395602.
- [16] Sarkar DK, Farzaneh M. Fabrication of PECVD-grown fluorinated hydrocarbon nanoparticles and circular nanoring arrays using nanosphere lithography. *Applied Surface Science*. 2008;254:3758-61.
- [17] Sarkar DK, Farzaneh M, Paynter RW. Wetting and superhydrophobic properties of PECVD grown hydrocarbon and fluorinated-hydrocarbon coatings. *Applied Surface Science*. 2010;256:3698-701.
- [18] Brassard JD, Sarkar DK, Perron J. Synthesis of monodisperse fluorinated silica nanoparticles and their superhydrophobic thin films. *ACS applied materials & interfaces*. 2011;3:3583-8.
- [19] Zhao L, Liu WL, Zhang LD, Yao JS, Xu WH, Wang XQ, et al. Fabrication of superhydrophobic and conductive surface based on carbon nanotubes. *Colloids and Surfaces A: Physicochemical and Engineering Aspects*. 2013;423:69-76.
- [20] Joung YS, Buie CR. Electrophoretic deposition of unstable colloidal suspensions for superhydrophobic surfaces. *Langmuir*. 2011;27:4156-63.
- [21] Besra L, Liu M. A review on fundamentals and applications of electrophoretic deposition (EPD). *Progress in Materials Science*. 2007;52:1-61.
- [22] Manca M, Cannavale A, De Marco L, Arico AS, Cingolani R, Gigli G. Durable superhydrophobic and antireflective surfaces by trimethylsilanized silica nanoparticles-based sol-gel processing. *Langmuir*.

2009;25:6357-62.

[23] Nishimoto S, Kubo A, Nohara K, Zhang X, Taneichi N, Okui T, et al. TiO<sub>2</sub>-based superhydrophobic–superhydrophilic patterns: Fabrication via an ink-jet technique and application in offset printing. *Applied Surface Science*. 2009;255:6221-5.

[24] Allen NS, Edge M, Ortega A, Sandoval G, Liauw CM, Verran J, et al. Degradation and stabilisation of polymers and coatings: nano versus pigmentary titania particles. *Polymer Degradation and Stability*. 2004;85:927-46.

[25] Ahmad Z. CHAPTER 2 - BASIC CONCEPTS IN CORROSION. *Principles of Corrosion Engineering and Corrosion Control*. Oxford: Butterworth-Heinemann; 2006. p. 50-2.

[26] Saleema N, Farzaneh M. Thermal effect on superhydrophobic performance of stearic acid modified ZnO nanotowers. *Applied Surface Science*. 2008;254:2690-5.

[27] Huang Y, Sarkar DK, Gallant D, Chen XG. Corrosion resistance properties of superhydrophobic copper surfaces fabricated by one-step electrochemical modification process. *Applied Surface Science*. 2013;282:689-94.

## 2. Literature review

### 2.1 Fabrication of superhydrophobic coatings

#### 2.1.1 Sol-gel process

As the name implies, the sol-gel process involves the evolution of inorganic networks through the formation of a colloidal suspension (sol) and gelation of the sol to form a network in a continuous liquid phase (gel) [1].

Sol-gel method has some unique advantages compared to other methods. It is a low-cost method suitable for application on large areas and complex-shaped substrates. The greatest advantage in employing the sol-gel method is fabricating superhydrophobic surfaces for all kinds of solids, such as metals, glass, silicon wafer, polymers, and textiles. There have been lots of papers published on the fabrication of superhydrophobic coating by sol-gel methods in recent years [2-6]. Material of low surface energy and micro- or nanoparticles can be added into the network to create superhydrophobic surfaces. JD. Brassard *et al.* [5] have prepared superhydrophobic thin films on flat aluminum and silicon substrates by spin-coating methods with the mono-dispersive spherical fluorinated silica nanoparticles prepared by sol-gel processes. However, most of sol-gel superhydrophobic coatings prepared by dipping, spinning or spraying processes are not very durable due to a lack of chemical bonds connected to the substrate. Therefore, we need find a medium such as self-assembled monolayers acting as binder between coatings and substrates.

## 2.1.2 Electrochemical deposition

The electrophoretic deposition (EPD) technique has been considered as an effective technique to fabricate superhydrophobic films recently due to the great advantages and easy control of the thickness and morphology of a deposited film through simple adjustments of the deposition time and applied potential[7]. During the EPD process, charged suspended particles in a liquid medium, with a DC electric field, are attracted and deposited onto an electrically conductive substrate of the opposite charge. Therefore, there are two types of electrophoretic deposition. The deposition of positively charged particles on the negative electrode (cathode) is termed as cathodic electrophoretic deposition, and in the contrary case, it will be termed anodic electrophoretic deposition.

Huang *et al.*[8] have prepared superhydrophobic ZnO thin films on aluminum alloy substrates through the electrophoretic deposition process using stearic acid functionalized zinc oxide nanoparticles suspension in ethanol. The EPD process shows great controllability of the atomic percentage of Zn and O, roughness and water contact angle of the thin films by varying the deposited bath temperature. As they reported, the 50°C deposited ZnO films showed superhydrophobic properties with water contact angle of  $155 \pm 3^\circ$ . Based on EPD technique, Ogihara *et al.*[9] reported SiO<sub>2</sub>/trimethylsiloxysilicate superhydrophobic composite coatings. Also, by changing the controllable electrophoretic deposition time, they successfully fabricated a transparent superhydrophobic coating. This result as well as work of Huang *et al.*

confirmed that EPD owns great advantage in controllability of deposited films as compared to other methods such as self-assembly [10], dip-coating [11].

## 2.2 Self-assembled monolayers (SAM)

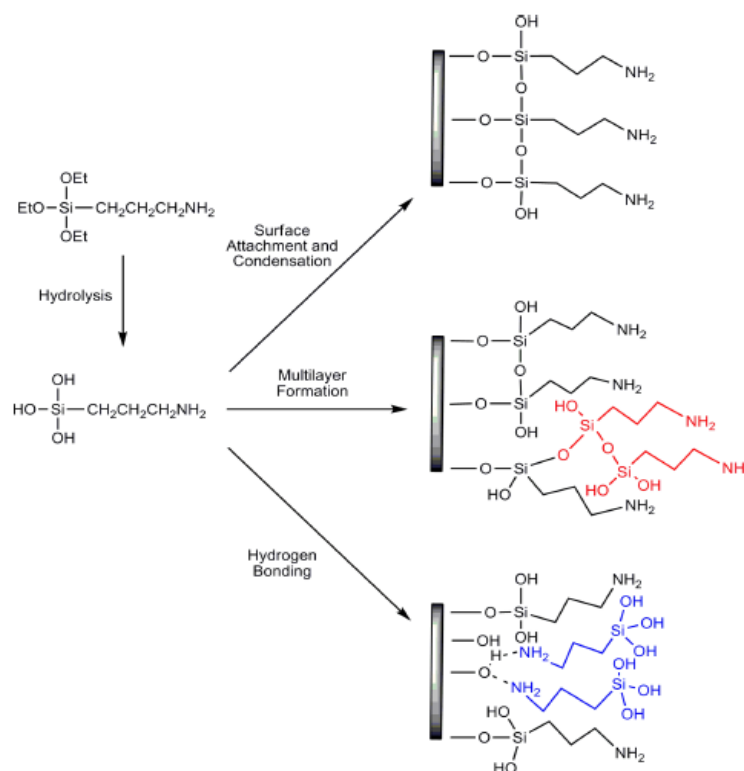


Figure 2. 1 The scheme for different bonding modes of SAM with APTES [12]

Self-assembly is defined as the spontaneous formation of complex hierarchical structures from pre-designed building blocks, typically involving multiple energy scales and multiple degrees of freedom [13]. Generally speaking, Self-assembled Monolayers (SAM) are ordered molecular assemblies formed by the adsorption of an active surfactant on a surface. SAMs are created by the chemisorption of "head groups" onto a substrate from either the vapor or liquid phase followed by a slow organization of "tail groups". Typically, head groups are connected to a molecular chain in which

the terminal end can be functionalized (i.e. adding  $-\text{OH}$ ,  $-\text{NH}_2$ ,  $-\text{COOH}$ , or  $-\text{SH}$  groups) to vary the wetting and interfacial properties [14]. An appropriate substrate is chosen to react with the head group. Substrates can be planar surfaces, such as silicon and metals, or curved surfaces, such as nanoparticles. SAMs gains two different head and tail groups, which make them real candidates as adhesion promoters for usual surface treatment process prior to painting [15]. Considering that point, we plan to use spin-coating on SAM modified aluminum substrates in the hope of building chemical bonds to connect PMHS sol-gel and aluminum. Here, we take (3-Aminopropyl)triethoxysilane (APTES) as an example to explain the scheme, as shown in the Figure 2.1 [12].

## 2.2.1 Preparation of SAM

In a general, SAMs can be prepared from both solution and gas phase, as shown in Figure 2.2 [13]. The traditional route is the solution process. It is a much easier way to build a thin monolayer on the substrate than the other method. Growth from the gas phase generally requires a more expensive experimental setup (i.e., usually a vacuum chamber) but also offers some advantages, such as a better control of the cleanliness of the environment, the substrate and the substances.

To date, there have been a large amount of papers published about how to make a SAM. Luzinov *et al.* [16] have fabricated a self-assembled monolayer with epoxy surface groups on silicon substrate. First, silicon wafers were cleaned and hydroxylated

in piranha solution. Then, the wafers were fully rinsed with ultrapure water and dried with nitrogen gas. After the rinsing, the substrates were dried under a stream of dry

- Self-Assembled Monolayers  
grown from solution



- Self-Assembled Monolayers  
grown from vapor

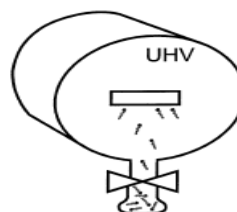


Figure 2. 2 Two methods of making a SAM [13]

nitrogen, immediately taken into the nitrogen-filled glove-box, and immersed in epoxysilane solutions of different concentrations for different periods of deposition time. After being removed from the solution, (3-glycidoxypropyl)trimethoxysilane (GPTS) the GPMS-coated wafers were ultrasonically cleaned in toluene and acetone, respectively, and dried with nitrogen gas. The film is designated as GPTS film, namely a self-assembled monolayer of epoxysilane. Li *et al.* [17] have prepared a thin polymer film covalently bonded to silicon substrate via an epoxy-terminated self-assembled monolayer. As an anchor interlayer, GPTS was self-assembled on hydroxylated silicon substrate to create epoxy-terminated surface, following the method of growing from solution.

On the other hand, more and more people begin to use the method of growth from vapor because it is easier to prevent aggregation of SAM molecules on the substrate's surface, as shown in Figure 2.2. Song *et al.* [10] have fabricated smooth amino-



functionalized surfaces by deposition of aminopropyltrimethoxysilane (APTMS) at the interface of vapor and solid. Clean and polished wafers with a thin oxide layer on the surface were placed in a sealed vessel with a container filled with toluene and APTES. It means there was no direct contact between the liquid and substrates. Then, the vessel was put in an oven maintained at 100 °C for 1h. With the reaction between APTES vapor and the hydroxyl groups of surface, they finally got APTES monolayer.

### **2.2.2 Characterization and analysis of SAM**

SAMs as a significant surface technology need to be characterized by various analytical techniques. Luzinov *et al.*[16] have analyzed the epoxysilane SAMs' surface morphology and microstructure properties on a Dimension 3000 (Digital Instruments, Inc.) Scanning Probe Microscopy (SPM) as well as utilized a COMPEL automatic ellipsometer (InOmTech, Inc.) to study ellipsometric thickness of the film. Sugimura *et al.*[18] reported that the chemical properties of organosilane self-assembled monolayers were characterized by water contact angle measurement performed at 298 K using an automatic contact angle meter (CA-X, Kyowa Interface Science), by chemical composition analysis using Mg K $\alpha$  radiation x-ray photoelectron spectroscopy (XPS, ESCA3400, Shimadzu) and  $\zeta$ -potential measurement carried on an electrophoretic light scattering spectrophotometer (ELS-600, Otsuka Electronics). F.M. Reis *et al.*[15] have studied self-assembled monolayer on Al 5052 alloy by investigating the influence of the electrochemical behavior on the SAM-treated surface by Electrochemical

Impedance Spectroscopy (EIS). This method is quite interesting as papers on SAMs characterized with EIS are rarely seen.

## 2.2.3 Important factors about SAM

Table 2. 1 Some important factors of SAMs [12, 14-19]

Substrates	Pre-treatment	Solvent	Silane	Condition/ parameter	P.S.
Si, SiO <sub>2</sub> /Si, Silicon derivatives	piranha solution ,namely 3:1 (v/v)concentrated sulfuric acid to 30% H <sub>2</sub> O <sub>2</sub> solution.	Toluene, Acetone, Benzene, anhydrous hexane, dimethyl sulfoxide (DMSO)/ethanol (under reflux), chloroform, methanol, and glacial acetic acid/methanol, DI water	-O-Si- APTES(3-Aminopropyltriethoxysilane)	1.Concentration 2.Temperature 3.Immersing time Or spinning speed	
Polymer, (e.g. polystyrene)	1% (w/v) KOH and oxygen plasma (e.g., using a reactive ion etcher)		GPTS(3-glycidoxypropyltrimethoxysilane)	4.Good solvent	
Au(1 1 1), Ag(1 1 1)	freshly prepared by evaporation of 100 nm of gold or silver (99.99% purity) onto polished single-crystal silicon (100) wafers with a 5-nm titanium interlayer to improve the adhesion		-S-Au-  alkanethiols (CH <sub>3</sub> CH <sub>2</sub> n-1SH)		
Al	NaOH(1M) aqueous solution		-O-Si-  APTES, GPTS		

It has taken a long time to develop SAM on all kinds of substrates since Bigelow *et al.* reported the successful case of alkyl-amines on Pt in 1946. Here, in table 2.1, we have discussed several important factors about SAM: substrates, silanes, solvent, etc. SAMs are particularly attractive for the following reasons: the ease of preparation; the tunability of surface properties via modification of molecular structure and functions; SAMs as building blocks for heterostructures, the use of SAMs as building blocks in more complex structures, e.g., for “docking” additional layers to a surface; the possibility of lateral structuring in the nanometer regime; the applications made possible by these features. But there are still some problems that need to solve. First,

there have been a lot of reports on SAM in recent years, but few were used on superhydrophobic surface. Second, most of the published papers focus on SAM created on Au, silicon and glass, however, it is rarely seen on Al. In this case, future work will focus on preparation of SAM on aluminum substrates and potential applications on mechanically durable superhydrophobic coatings.

### **2.3 Durable superhydrophobic coatings**

Large quantities of papers have been published on ways to fabricate superhydrophobic surfaces [2, 3, 5, 19-25]. Most of these surfaces possess the advantages of having a very great contact angle and exhibiting minimal sticking to water droplets. According to reports published, superhydrophobic surfaces have so many applications in every aspects of our lives, such as antifouling paints for boats [26], waterproof clothes [27], corrosion inhibition [28, 29], water and oil separation [4]. However, it is quite difficult to make it last for long periods. Normally, superhydrophobic surfaces are easily damaged by mechanically scratch or deformed by ultraviolet when exposed in the outdoor environment. The fragility of superhydrophobic surfaces severely limits their applicability. A durable superhydrophobic surface with easy-reparability will enable a wide range of new applications in harsh environments such as high UV irradiation, high temperature, terrible abrasion and chemical corrosion.

### **2.3.1 Mechanical durability**

Superhydrophobic surfaces maintains great potential on numerous fields such as anti-corrosion, anti-icing, non-wetting fabrics, self-cleaning windows and drag reduction to name a few. However, development of durable superhydrophobic surfaces is hindered by their poor mechanical properties due to the microscopic roughness features are easily damaged by physical force. To realize a wide range applications of superhydrophobic coatings in industrial world, we cannot ignore such an inevitable and significant problem. Many mechanical behaviors are able to cause a superhydrophobicity-loss transition. Normally, mechanically damaged superhydrophobic surfaces show a decreased contact angle and an increased contact angle hysteresis. The non-wettability of a surface patterned with topography can be reduced essentially in two ways: (a) loss of roughness increases the area of contact between water and the surface, or (b) the intrinsic hydrophobicity of the surface is reduced as a result of hydrophilic contamination or damage to a hydrophobic surface layer [30].

As for the mechanical durability of superhydrophobic surfaces, there are quite a few different aspects to test, including the adhesion test, abrasion test and hardness test. There exist various test methods for the varied aspects as given below.

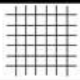
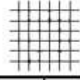
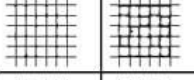
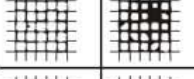
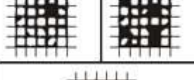

#### **(1) Adhesion test**

Adhesion test is used to test the adhesion force between the superhydrophobic coatings and the substrates. The method used for the test is carried out according to the American Standard Test Method (ASTM) D 3359-02 which is recognized worldwide.

There are two methods described in this ASTM Specification. One is to make an X-cut pattern, which is primarily intended for use at job sites. After an X-cut is made through the film to the substrate, pressure-sensitive tape is applied over the cut and then removed, and adhesion is assessed qualitatively on the 0 to 5 scale. Another is to make a crosshatch pattern, which is more suitable for use in the laboratory but not suitable for films thicker than 125  $\mu\text{m}$ .

Here, we mainly discuss the latter one. The test process is depicted as follows: A crosshatch pattern is made through the film onto the substrate. Square grids with a side length of 1mm are cut on the coated substrate with a steel blade. Detached flakes of coating are removed by brushing with a soft brush. Pressure-sensitive tape is applied over the crosshatch cut. Tape is smoothed into place by using a pencil eraser or hand to smooth over the area of the incisions. Tape is removed by pulling it off rapidly back over itself at as close to an angle of 180  $^{\circ}$  as possible. In table 2.2, the adhesion strength is assessed on a 0 to 5 scale.

Table 2. 2 Classification of test results

Surface	Description	ISO	ASTM
	The edges of the cuts are completely smooth; none of the squares of the lattice is detached.	0	5B
	Detachment of flakes of the coating at the intersections of the cuts. A cross cut area not significantly greater than 5% is affected.	1	4B
	The coating has flaked along the edges and/or at the intersections of the cuts. A cross cut area significantly greater than 5%, but not significantly greater than 15% is affected.	2	3B
	The coating has flaked along the edges of the cuts partly or wholly in large ribbons, and/or it has flaked partly or wholly on different parts of the squares. A cross cut area significantly greater than 15%, but not significantly greater than 35%, is affected.	3	2B
	The coating has flaked along the edges of the cuts in large ribbons and/or some squares have detached partly or wholly. A cross cut area significantly greater than 35%, but not significantly greater than 65%, is affected.	4	1B
	Any degree of flaking that cannot be classified even by classification 4 (1B).	5	0B

Kumar *et al.* [31] have prepared hydrophobic and superhydrophobic sol-gel coating based on a tetraethylorthosilicate (TEOS) and glycidoxypropyltriethoxysilane (GPTS) matrix with the addition of fluoroalkylsilane modified silica filler particles. According to ASTM method, the tape test result for surfaces with different amounts of silica is shown in figure 2.3. It showed that the coatings with increasing filler content progressively show higher removal of coating from the grids, which prove to have poorer adhesion strength. The reason could be that the increased surface roughness and coating porosity would increase severity of coating flaws that lead to the brittleness of coatings as observed. So it is a pity that a superhydrophobic coating with high roughness showed only 1B adhesion strength which is not good enough for practical applications.

In figure 2.4, Xu *et al.*[32] reported a perfluoroalkylsilane (FAS) passivated superhydrophobic coating on glass by colloid assembly method involving the uses of dual-sized silica particles and an acidic silica sol showing strong adhesion strength. Because FAS surface is anti-stick, they conduct the tape test before the FAS modification. The experiment demonstrated that the adhesion strength is proved as 5B according to this method. It was explained by the fact that cross-linked Si-O-Si chemical bonds were formed by the reaction between the active hydroxyl groups on the linear silica-based polymers and the hydroxyl groups on the glass substrate. It is very cheering that adhesion strength could reach 5B. The chemical bond is fairly strong. However, the substrate is limited to glass which must have plenty of -OH groups on the surface.

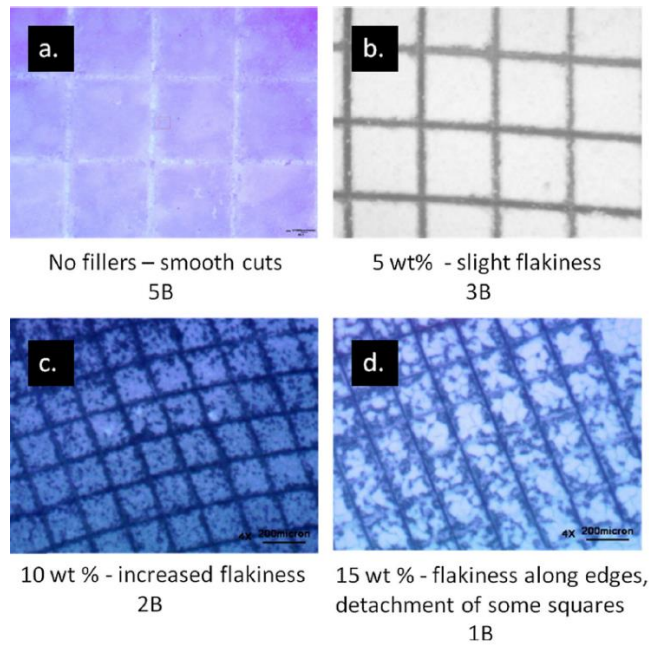


Figure 2. 3 Cross-hatch tape adhesion test for coatings with 10–20 nm silica fillers. (a-c) Hydrophobic surface and (d) superhydrophobic surface [31]

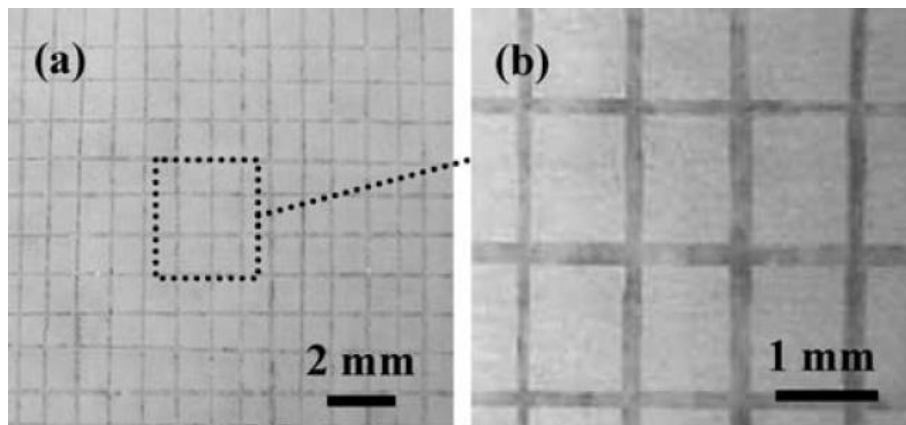


Figure 2. 4 Images of the grid area of a sample before (a) and after (b) Cross-hatch tape adhesion test [32]

Obviously, there are some other ways to test the adhesion strength. Yuan *et al.* [33] successfully dropped different ratios of mixture solution of polydimethylsiloxane

(PDMS)/CaCO<sub>3</sub> on substrates and made a superhydrophobic coating with good mechanical properties. Adhesion strength testing was performed by an electronic tensile testing machine. PDMS/CaCO<sub>3</sub> coating was cut into 2 × 1.5 cm<sup>2</sup> squares. The detached speed parameter was set as 150 mm/s. With their home-designed method (shown in figure 2.5), the adhesion test results on glass, paper and copper were all greater than 13N at the moment the double-side adhesive was detached from the coating surface. Frankly, this method is quite new and could estimate the strength in detailed number. It could be a good, mechanically stable coating, nevertheless, it is really difficult for us to compare this one with other results.

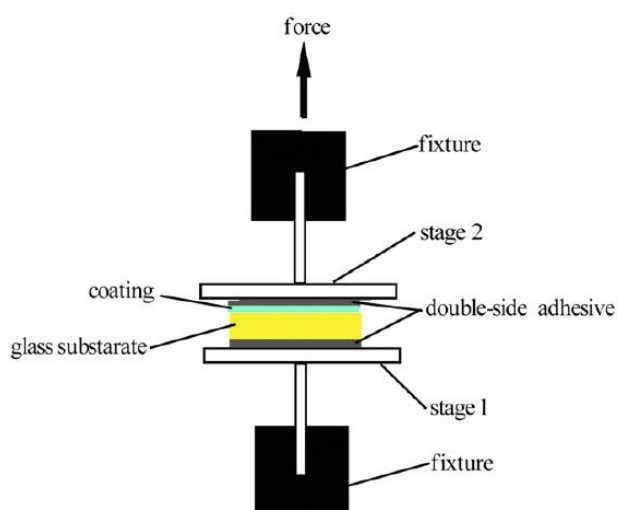


Figure 2. 5 Schematic illustration of adhesion strength test [33]

## (2) Abrasion test

The abrasion test or scratch test is used to characterize the shear resistance property of coatings by measuring the changes before and after abrasion process as applied to the weight, roughness, thickness, contact angle and contact angle hysteresis. Recently,



many reports have been published on abrasion tests on superhydrophobic coatings created with home-made equipment.

One of the most popular experiments (shown in figure 2.6) is carried out using sand paper served as an abrasion surface, with the superhydrophobic surfaces to be tested facing the material. Simultaneously, a pressure is applied on the coatings with a heavy object. Then, the coated surfaces are dragged in a horizontal line back and forth several times. Finally, measurements on contact angle, thickness, morphology and other properties are analyzed after the test. If there is no big change or the surface has maintained its superhydrophobic property, it proves that the coating shows good resistance against mechanical abrasion.

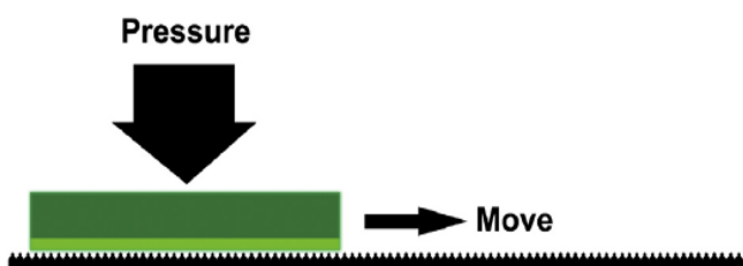


Figure 2. 6 Schematic diagram of the abrasion test equipment with sand paper used as an abrasive surface [34]

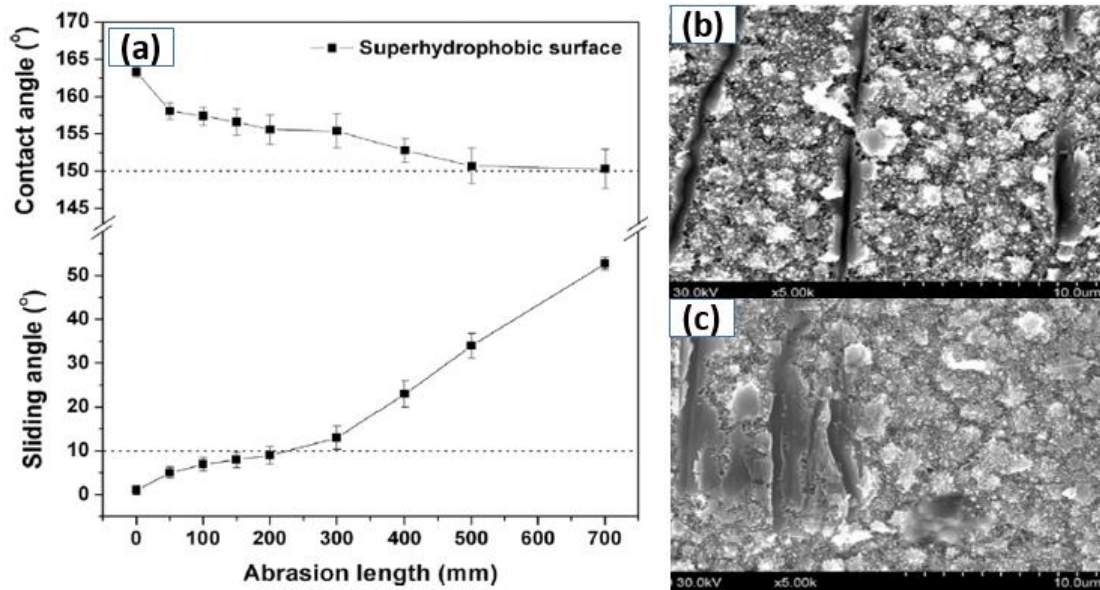


Figure 2. 7 (a) Contact angle and sliding angle on the coating as a function of abrasion length; SEM images for the coating after abrasion length of (b) 400mm  
(c) 700mm [34]

She *et al.*[34] have prepared a pinecone-like superhydrophobic surface on pre-treated magnesium substrates through a process combining both electrodeposition of nickel and stearic acid chemical modification. The scratch test is shown as figure 2.2.1(a). SiC paper (800 mesh) is the abrasive surface and pressure is 1200 Pa. The surface was dragged for 700mm with contact angle turned from 163° to 150° and sliding angle from  $1.2 \pm 0.9^\circ$  to  $52.7 \pm 1.4^\circ$ . The result is shown in figure 2.7. The obvious scratches and smoothness of the coating are the most important reason for gradually losing superhydrophobicity. It can be speculated that the coating is too hard and brittle because of the weak bond strength between the electrodeposited nickels.

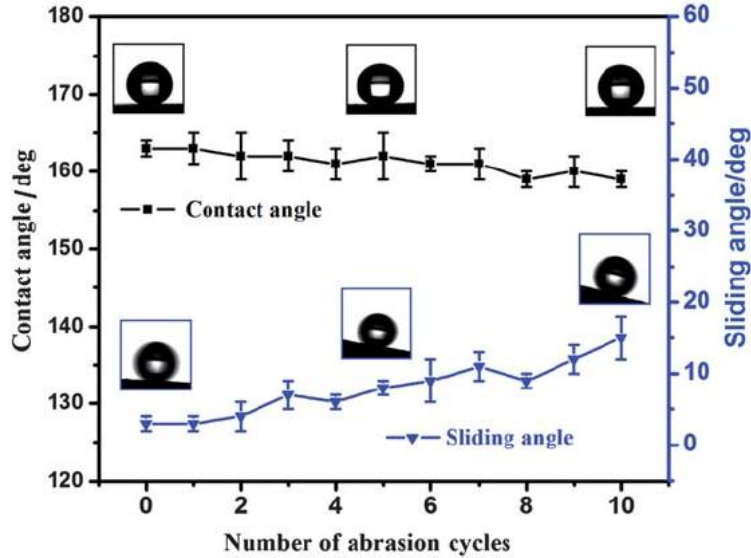


Figure 2. 8 Contact angle and sliding angle on the metal/polymer composite surface as a function of abrasion cycles [35]

Zhu *et al.* [35] have fabricated a metal/polymer composite superhydrophobic coating through mixture of UHMWPE with copper powder in a mold under pressure and a reaction with  $\text{AgNO}_3$  solution followed by fluorinated passivation. The scratch test was conducted on home-made equipment. The abrasive surface is 1500 mesh sandpaper, with the superhydrophobic surface to be tested facing the abrasive material. The superhydrophobic surface was under a pressure of 10 kPa, dragged in one direction with a speed and abrasion length of  $3 \text{ cm s}^{-1}$  and 30 cm, respectively. The results are shown in figure 2.8. It should be noted that the most essential thing for creating a durable superhydrophobic coating is the fact every freshly exposed surface created by repeated abrasion also must be superhydrophobic. Copper powder was firmly embedded inside the polymer substrate during the preparation process, and Ag which took the place of Cu was also deeply imbedded inside the polymer substrate.

Similar principals apply for abrasion resistance properties found on the polymer composite superhydrophobic disks (as shown in figure 2.9) prepared by hot-pressing the mixtures of polytetrafluoroethylene/polyvinylidene (PTFE/PVDF) powder and followed by abrasion with sandpapers, which is a well done job by Wang *et al.* [36]. Even when the surface is polluted by dust or organic contaminant, superhydrophobicity can be repaired by abrading regeneration process within a few minutes. The abrasion test was conducted on the 320 mesh sandpaper. Pressure of 30 kPa was applied to the superhydrophobic surface, the surface was dragged in a linear direction with a speed and abrasion length of  $10 \text{ cm s}^{-1}$  and 20 cm, respectively. Obviously, the polymer disk itself has low-energy surface and acquires roughness by abrading to become a superhydrophobic surface. So every freshly exposed surface is a new born superhydrophobic surface.

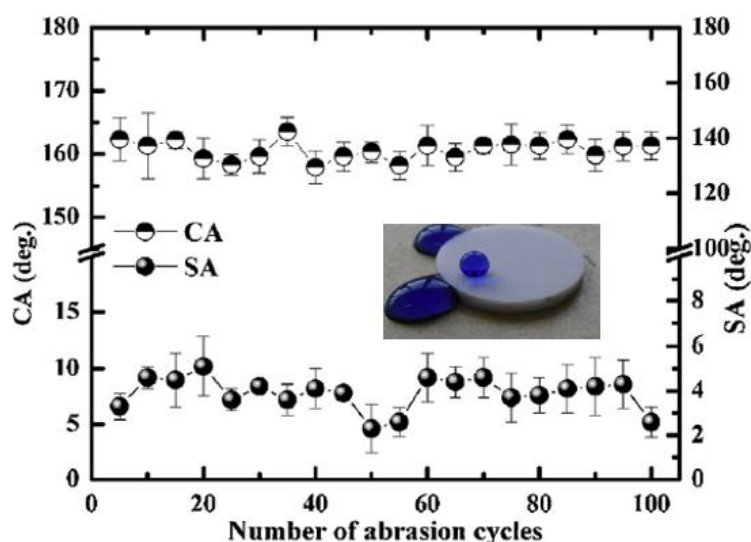


Figure 2. 9 Contact angle and sliding angle on PTFE/PVDF composite surfaces as a function of abrasion cycles [36]

### (3) Hardness test

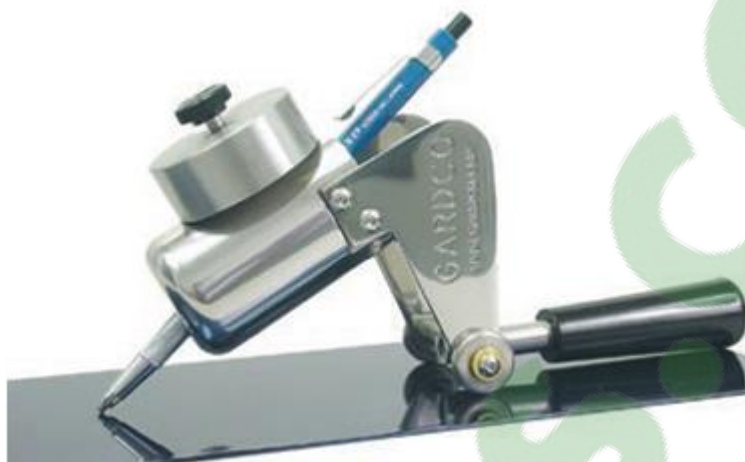


Figure 2. 10 Image for pencil hardness test

Hardness is another important factor for the mechanical durability of the non-wettability coating[11, 37]. Pencil hardness measurements are used to determine the hardness of organic coatings. The hardness of a coating, relative to a standard set of pencil leads, is determined by scratching the leads across the coating at a controlled angle of  $45^\circ$  for a distance of approximately  $\frac{1}{4}$  inch. The pencil hardness test is a constant-load scratch test (as shown in figure 2.10). It uses pencil leads of different hardness grades (9B–9H) as the scratch stylus. The same normal load with indenters of different hardness is applied on the samples. The hardest pencil grade that does not cause damage to the coated specimen is considered as the pencil hardness of the coating.

Lakshmi *et al.*[37] have prepared a sol-gel superhydrophobic coating on glass substrate by embedding fumed silica nanoparticles in a partially condensed hybrid sol of methyltriethoxysilane (MTEOS) and colloidal silica. According to the method mentioned above, the coatings with 16.58 w.t% silica exhibited water contact angles as

high as 162.5° with a pencil hardness of 5H. It is quite understandable that the silica contributes a lot to that elevated hardness value.

### **2.3.2 UV durability**

It is well known that superhydrophobic surfaces with “the lotus effect” have attracted increasing attention during the past decades due to their great potential in widespread applications including anti-corrosion and self-cleaning. When these surfaces are exposure in the ambient air, most of them are vulnerable to be damaged by the ultraviolet (UV) in the solar light, gradually losing their property of superhydrophobicity. As we may know, commercially available polymers such as polydimethyl siloxane, ethylene-vinyl acetate copolymer and Teflon, all showed surface degradation after long time UV aging tests. The longevity of those surfaces takes a really significant role in their wide application in industry. To my best knowledge, ultraviolet stability of superhydrophobic surfaces has not yet been studied extensively compared with anti-corrosion, which is a requirement for outdoor applications [38].

#### **2.3.2.1 The principal of superhydrophobic coatings destroyed by UV**

In figure 2.11, we show a solar radiation spectrum which consists of 44% infrared light, 50% visible light, 6% ultraviolet light. Among them, ultraviolet light is the most powerful part owning enough energy to break most of the chemical bonds. Considering

the unstable weather and time-consuming experiment, a UV chamber has been designed to simulate the UV part in the solar light.

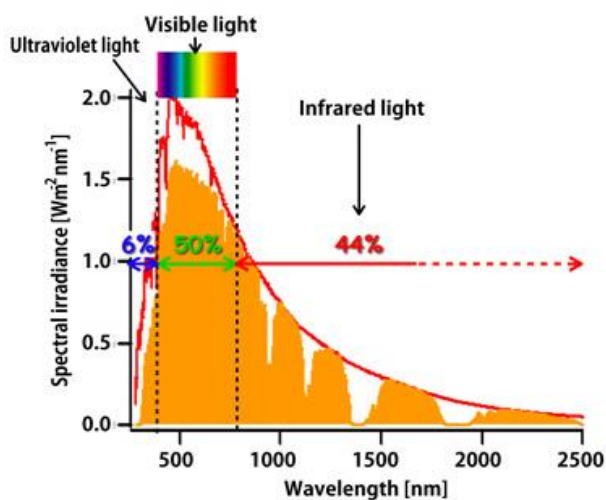


Figure 2. 11 Solar radiation spectrum

Most of superhydrophobic coatings will undergo a photo-oxidation process to form carbonyl or hydroxyl groups on the surface under UV irradiation. Those hydrophilic groups would change the wettability and reduce the contact angle of these surfaces. According to the Wenzel model [39], the creation of roughness on a flat surface with an equilibrium contact angle  $\theta$  (flat)  $> 90^\circ$  increases the contact angle, while the same roughness on a surface with  $\theta$  (flat)  $< 90^\circ$  decreases the contact angle [40]. When the surface is hydrophilic, surface roughness enhances the hydrophobicity to superhydrophilicity. That is the reason why those surfaces lose the properties of superhydrophobicity.

### 2.3.2.2 Superhydrophobic coatings under UV irradiation

Generally, when superhydrophobic surface are exposed under UV irradiation, the UV degradation behaviors could be summarized into three different categories as given below:

#### (1) Easily destroyed by UV

The first one is the most common around us. These superhydrophobic surfaces can be destroyed by UV very easily and lose function totally [41, 42]. In figure 2.12, Xia *et al.* [42] have made a self-cleaning superhydrophobic surface based on titanium dioxide nanowires combined with polydimethylsiloxane (PDMS) by a dip-coating process. Upon UV irradiation (obtained from a 8W Hg lamp with a wavelength) for 6h, the superhydrophobic surface was converted into hydrophilic one, with the contact angle changing from  $158 \pm 1^\circ$  to  $25 \pm 1^\circ$ . It could explained by the fact that  $\text{TiO}_2$  activated by UV irradiation shows a great ability of photocatalysis which can decompose PDMS and generate many hydroxyl groups.

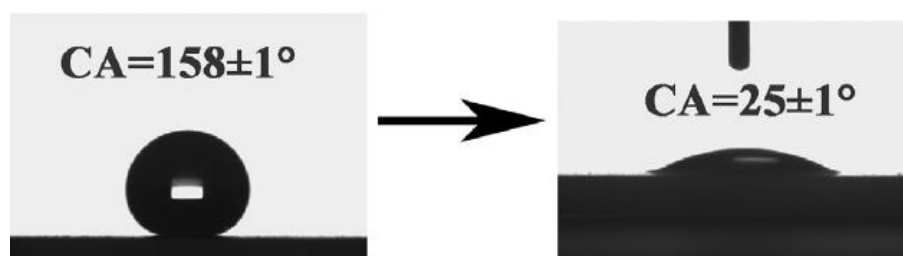


Figure 2. 12 Photographs of water droplet shape on  $\text{TiO}_2$  coatings before (left) and after (right) UV illumination for 6h [42]



## **(2) Reversible superhydrophobicity to superhydrophilicity transition**

The second one is quite interesting due to the tunable surface wettability after irradiation with UV light [43, 44]. Even though those surfaces cannot maintain their superhydrophobicity under UV, they can regain that property after being put back in darkness or by heating, a process which can be recycled many times with almost no change of contact angle. Lei Jiang's group[43] managed to prepare an aligned ZnO nanorod smart film with reversible superhydrophobicity to superhydrophilicity transition controlled by alternation of UV illumination and dark storage (as shown in figure 2.13). As reported, upon UV irradiation (obtained from a 500 W Hg lamp with a filter centered at  $365 \pm 10\text{nm}$  for 2 h), the water droplet spread out on the film, resulting in a CA of about  $0^\circ$ . After the UV irradiated films were placed in the dark for 7 days, it returned into a superhydrophobic surface again. This reversible super-hydrophobic-super-hydrophilic transition can be explained as follows: UV irradiation will generate electron-hole pairs in the ZnO surface. Some of the holes can react with lattice oxygen to form surface oxygen vacancies. The defective sites are kinetically more favorable for hydroxyl adsorption than oxygen adsorption, which turns the surface into a superhydrophilic one. But after dark storage, the hydroxyl adsorbed on the defective sites can be replaced gradually by oxygen atoms, which allows the surface to be converted back to its original superhydrophobicity.

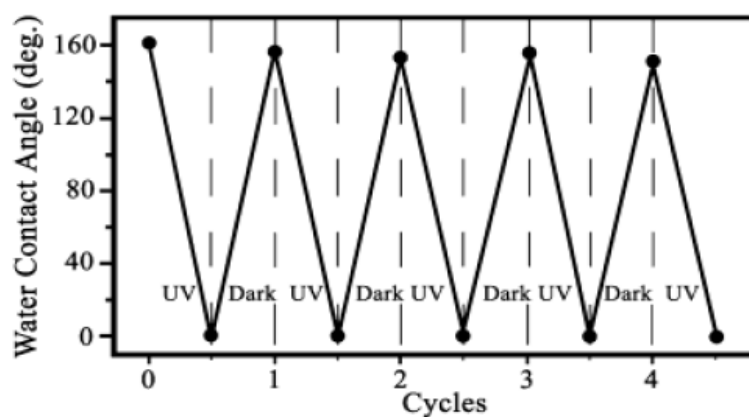


Figure 2. 13 Reversible super-hydrophobic-super-hydrophilic transition of the as-prepared films under the alternation of UV irradiation and dark storage [43]

### (3) Long-term UV stability

Those superhydrophobic surfaces have great potential in a wide range of outdoor applications because of their excellent UV durability. Xiu *et al.* [40] successfully fabricated an inorganic superhydrophobic coating, by sol-gel method, using tetramethoxysilane and isobutyltrimethoxysilane as precursors. They checked the UV stability of the as-prepared surfaces under prolonged UV tests (ASTM D 4329). A UVA-340 fluorescent lamp was used to simulate the short and middle UV wavelength region corresponding to daylight exposure. These surfaces gradually lost their superhydrophobic properties in a short time. However, after the organic parts were removed by heat treatment and then modified with fluoroalkylsilanes, the characteristics of superhydrophobicity were maintained even after 5500h UV irradiation with no degradation of either contact angle or contact angle hysteresis. The result was shown in Figure 2.14. However, they didn't illustrate the mechanism clearly. It could be explained by the presence of a linear fluorocarbon chain on the silica surface,

which improved UV stability due to the fact that C-F bonds are much stronger than the C-H bonds. Even though it could create the most effective UV stability coating, the process is really complex and the mechanism is not known clearly yet.

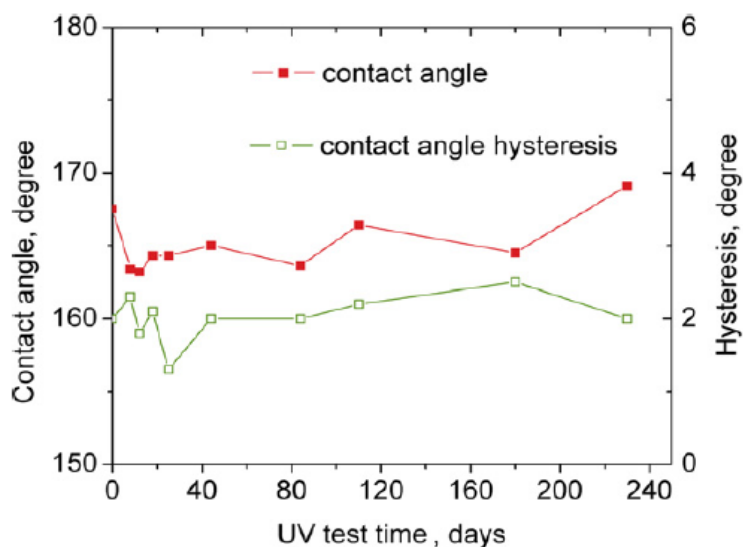


Figure 2. 14 UV stability of a PFOS-treated rough silica thin film [40]

Ding *et al.* [45] have fabricated a superhydrophobic coating by blending fluorinated polysiloxane and different weight percentages of TiO<sub>2</sub> nanoparticles. In figure 2.15, after being subjected to an accelerated weathering test for 4 weeks, all superhydrophobic coatings showed a slight decrease in water contact angle. As they explained, the chemical bond of Si-O and C-F with bonding energy up to 460 and 485 kJ mol<sup>-1</sup> respectively can neither be decomposed by photocatalytic TiO<sub>2</sub> (band gap: 3.2 eV or 309 kJ mol<sup>-1</sup>) nanoparticles nor by UV light (314-419 kJ mol<sup>-1</sup>). However, fluorinated polysiloxane is quite expensive and not appropriate for practical applications.

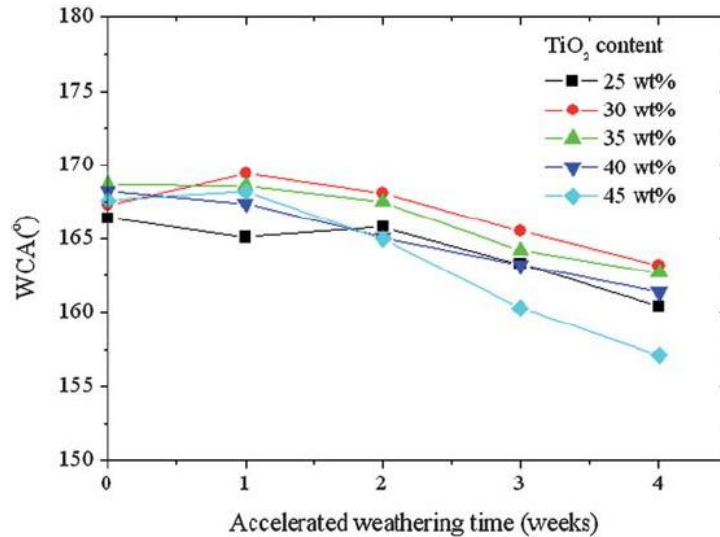


Figure 2. 15 Changes of WCAs of the superhydrophobic coatings with different TiO<sub>2</sub> contents under QUV accelerated weathering test [45]

In other words, we have already found a way to improve the UV stability of superhydrophobic coatings by grafting some chemical bonds with higher energy than that of ultraviolet and the band gap of a UV absorber (oxide nanoparticles).

As we discussed before, nanoparticles like TiO<sub>2</sub> [42, 46, 47], ZnO [39, 48-50] and CeO<sub>2</sub> [51] are well known for the role of inorganic UV absorbers. On the other hand, they could accelerate degradation of the polymer or fluoroalkyl-silane because of photocatalytic reaction. Therefore, people are becoming more and more interested in using other nanoparticles like SiO<sub>2</sub> to suppress the photoactivity of TiO<sub>2</sub>, ZnO. This should be another method that we can employ to develop UV-stable superhydrophobic coatings. Wang *et al.*[49] have successfully prepared a UV-stable superhydrophobic octadecyltrimethoxysilane (OTS) modified ZnO@SiO<sub>2</sub> nanowire array by combining the hydrothermal method and layer-by-layer technique (shown in figure 2.16). By

comparing the contact angle of substrates with OTS-modified ZnO or ZnO@SiO<sub>2</sub> NW array placed under a Hayashi LA-410 light source, we can see the greatly improved UV durability of the latter one, as shown in figure 2.3.3. The UV source emits UV light in the range of 320-400 nm, whose intensity was maintained at 5.0 m W cm<sup>-2</sup>. As for the mechanism of UV stability, it could be illustrated that the insulating ~4.17nm SiO<sub>2</sub> shell was believed to effectively suppress the surface chemical reactions or surface reconstruction initiated by photo-generated hole-electron pairs in ZnO NWs. With the confinement effect, the photocatalytic oxidation reactions which generate hydroxyl

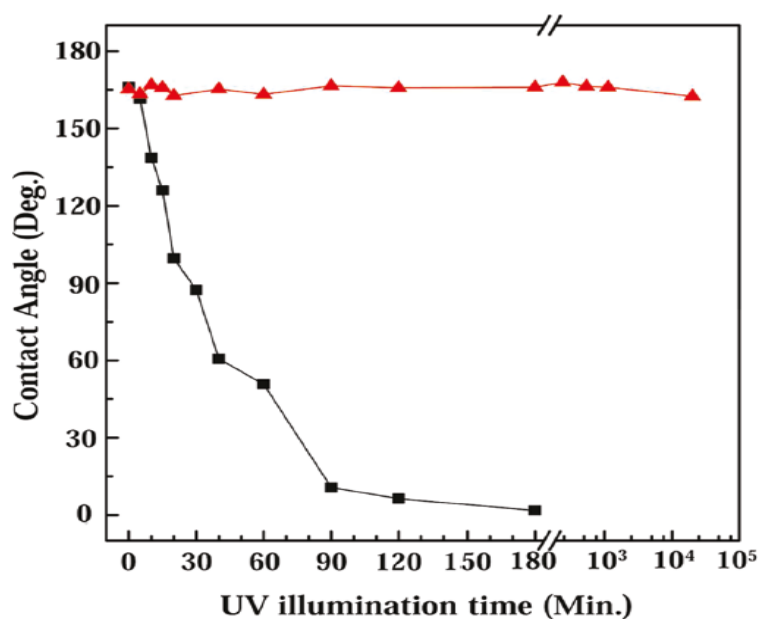


Figure 2. 16 Evolution of water CA on OTS-modified ZnO NW array (squares) and OTS-modified ZnO@SiO<sub>2</sub> NW array (triangles) under UV irradiation[49]

radicals and groups will not happen. That is the principal of maintaining superhydrophobicity. They also applied the same coating on cotton textile and it is also

an ultraviolet-blocking surface as well [50]. However, the fabricating process is a little too complex for widespread use.

As another important photocatalytic material,  $\text{TiO}_2$  also shows strong oxidative power after UV excitation with which it can completely decompose organic substances as well as UV-induced superhydrophilic transition. Isimjan *et al.*[47] revealed a superhydrophobic coating combining  $\text{TiO}_2$  nanoparticles with the low surface energy chemical 1H, 1H, 2H, 2H-perfluorodecyltriethoxysilane (PTES) on a steel surface, with water contact angles as high as  $165^\circ$ . Nevertheless, the pure P25  $\text{TiO}_2$  and PTES mixture coating cannot resist UV light (315-400 nm, 100 mW/cm<sup>2</sup>) and the contact angle switched from  $\sim 170^\circ$  to 0 in five hours.

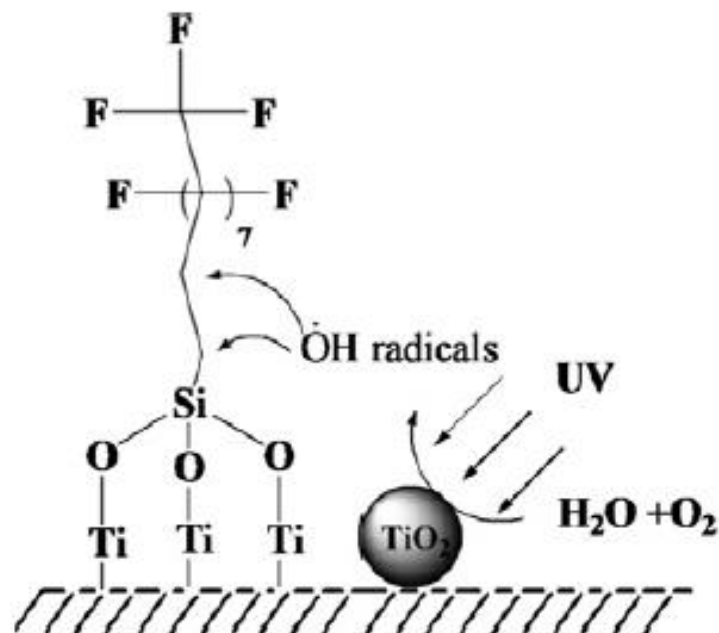


Figure 2. 17 Photo degradation process of PTES based superhydrophobic surface [47]

The reason why  $(\text{TiO}_2)_3$  coatings lost superhydrophobicity is the  $-\text{OH}$  radicals which are generated by  $\text{TiO}_2$  nanoparticles under UV irradiation oxidize the two  $\text{CH}_2$  that are located between  $-\text{Si}$  and  $-\text{CF}_2$ . The mechanism is illustrated in figure 2.17. However, after applied extra-layers of  $\text{SiO}_2$ , the coatings show long term UV-durability properties, which are indicated by the stable line of contact angles during 300 mins.

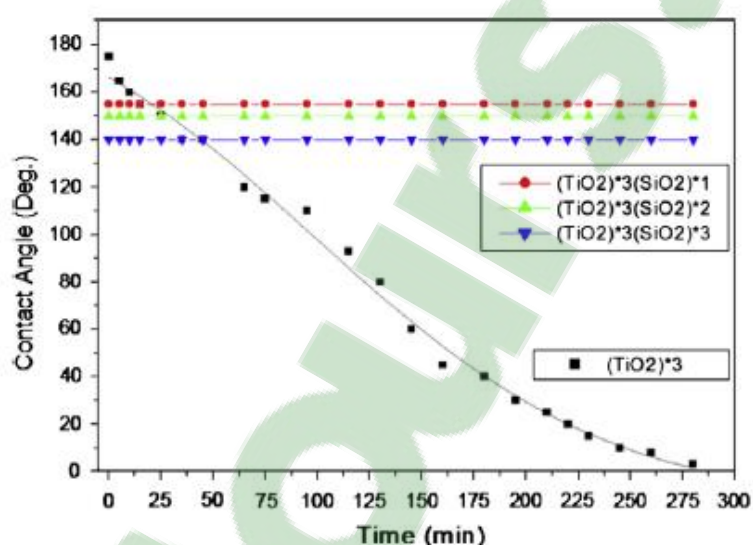


Figure 2. 18 Contact angles of three different layers of  $\text{SiO}_2$  on the top of  $\text{TiO}_2$  ( $\text{P}25$ ) $_3$  coated superhydrophobic samples after certain periods of time [47]

As shown in Figure 2. 18, 3 layers of  $\text{TiO}_2$  coatings are not UV stable while  $\text{TiO}_2/\text{SiO}_2$  coated steel surfaces strongly resist against UV radiation: the contact angles remain constant even after a period of 5h UV exposure. That is due to the presence of  $\text{SiO}_2$  nanoparticles, the high energy electrons generated by  $\text{TiO}_2$  under UV could not diffuse to the surface. Therefore, no oxidation will happen without  $-\text{OH}$  radicals being formed. However, we noticed that the initial contact angle decreased with increase of  $\text{SiO}_2$

nanoparticle layers. It can be explained by the fact that surface roughness will be reduced with smaller particles of SiO<sub>2</sub> filling up the space that was created by TiO<sub>2</sub> particles according to Cassie models.

## **2.3.3 Thermal durability**

### **2.3.3.1 Thermal damage**

For most of the studies of superhydrophobic materials, people have been keeping their main concentration on theoretical analysis of requirements and methods for creating special textures and coatings imparting hydrophobic and superhydrophobic properties to the surfaces of materials. Yet, in the practical application aspects, we can never emphasize too much that these materials can sustain harsh conditions to retain superhydrophobic character. Among those, one of the challenges is thermal damage. It is really important that those non-wettability coatings can function well over a wide range of temperatures, and especially some extreme high temperatures[52]. The thermal degradation of the coating is primarily due to a change in the surface chemical composition rather than caused by a change on surface morphology roughness. Hydrophobic functional groups could get diminished either by oxidation reaction or the breaking of chemical bonds which connect to the substrate matrix.

### **2.3.3.2 Fabrication of thermally stable superhydrophobic coatings**

There are not so many reports on the thermal stability as a mechanical aspect. To my best knowledge, the method of preparing thermally stable superhydrophobic



coatings can be summarized in two catalogs, namely the first is to utilize inorganic/organic silica or silanes and the second way is to take advantage of polymers with high melting or glass transition temperatures.

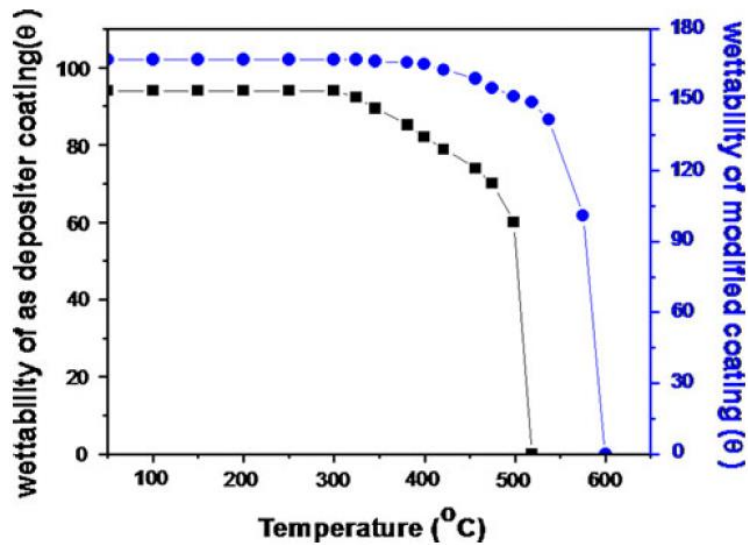


Figure 2. 19 Contact angle as a function of temperature for organically silica coatings (black) before (blue) after modified by TMCS [53]

Mahadik *et al.*[53] have prepared organic silica superhydrophobic coatings by spraying alco-sol on hot glass substrates and followed by surface modification with mono-functional trimethylchlorosilane (TMCS). The thermal durability of coatings was confirmed by placing samples in the furnace at varied temperatures and characterized by contact angle measurements. In figure 2.19, TMCS modified coatings not only showed much higher contact angles but also better performance on thermal stability with hydrophobicity that can be retained at up to 500 °C. Also, according to their TGA-DTA and FTIR analysis, the reason for better thermal stability lies in that the surface modification of as-deposited films with TMCS enhances thermal stability due to the

effective replacement of  $-\text{Si}-(\text{OCH}_3)_3$  groups with non-hydrolysable thermally stable  $-\text{Si}-(\text{CH}_3)_3$ .

Li *et al.* [54] prepared a 300 °C thermally stable superhydrophobic coating by introducing in-situ functionalized nano- $\text{SiO}_2$  into a side-amino modified hydroxyl-terminated polydimethylsiloxane curing system. X. Deng *et al.*[55] also fabricated a transparent and thermally stable superhydrophobic coating by dip-coating 50-nm-sized silica particles synthesized in Stöber-reaction on glass and followed up with chemical vapor deposition of tetraethoxysilane. The superhydrophobic coating is thermally stable up to 350 °C.

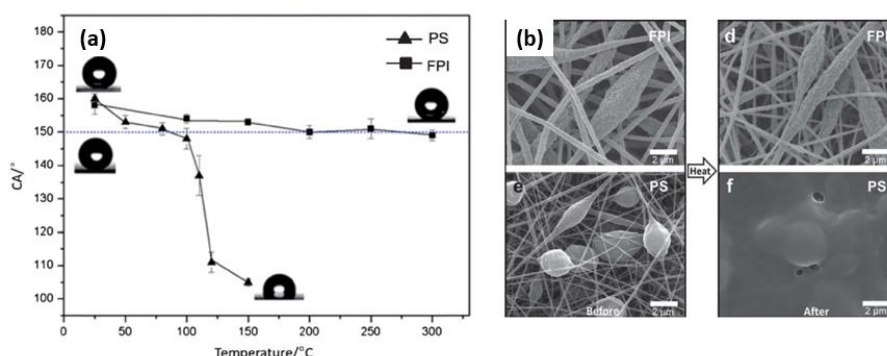


Figure 2. 20 (a) Water contact angle plotted against the thermal treatment temperature; (b) the SEM images of FPI and PS samples before and after heating at 150 °C [56]

Gong *et al.* and his partners[56] successfully turned intrinsic hydrophilic polyimide (PI) into thermally stable superhydrophobic materials by synthesizing fluorinated polyimide (FPI) and electrospinning it into a highly porous nonwoven mat. For comparison, the same method was done with polystyrene (PS). The thermal

treatment was carried out by heating them for 1 hour at varied temperatures. The results are shown in figure 2.20(a). The FPI samples can maintain superhydrophobicity up to 300°C while the contact angles of PS samples were no longer superhydrophobic after ~110°C. From the SEM images shown in figure 2.20(b), it is clearly revealed that FPI's micro structures remained while PS's micro structures had been ruined when heated at 150 °C. This phenomenon can be explained by the fact that PI has a higher glass transition temperature ( $T_g$ ), at around 243°C, than that of PS as around 100 °C. The glass transition temperature ( $T_g$ ) is defined as the temperature region where the polymer transitions from a hard, glassy material to a soft, rubbery material. This method can bring us a thermally stable superhydrophobic material, however, we have to see the fact that it is really an expensive option.

## **2.3.4 Chemical durability**

### **2.3.4.1 Chemical corrosion**

Commercial metals such as aluminum, zinc, copper are really important materials in every aspect of our daily lives, however, their alloys decay easily and are destroyed by corrosion especially when they come in contact with aggressive and corrosive environments such as alkaline, acid solution or strongly saline solutions. Corrosion is usually defined as the destruction of a metal by chemical or electrochemical reactions between the metal and its environment[38]. As we may know, metals like aluminum may gain a thin oxide layer on their surfaces which inhibits further corrosion. Nevertheless, chemically corrosive solutions can penetrate this layer and react with the

inner metal molecules. Every year, countless tons of metals are put out of function because of corrosion. Thus this situation urges people to come up with alternative solutions to avoid this waste. The development of superhydrophobic coatings on metals as a passivation layer is quite a promising scheme which may potentially be superior to the other conventional methods currently available.

### 2.3.4.2 The principal for anticorrosion properties

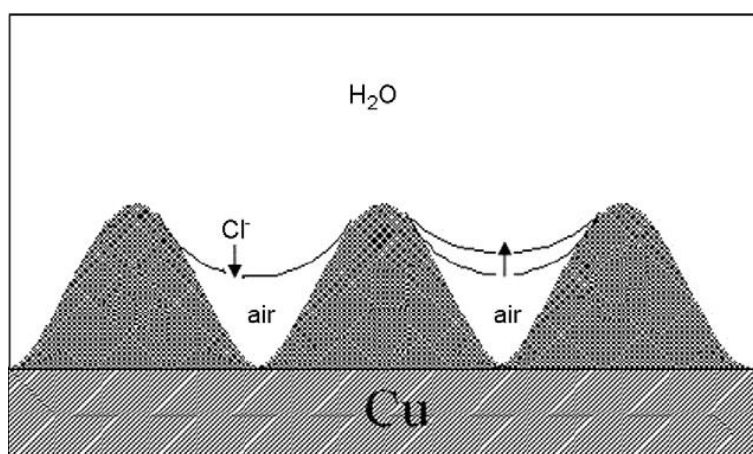


Figure 2. 21 Model for the anticorrosion mechanism[57]

A lot of different techniques have been used to fabricate superhydrophobic surfaces. But almost all of them have stated that their coatings can be utilized to inhibit corrosion on metal. Why? The mechanism lies in two aspects [28, 58].

First, superhydrophobic surfaces featuring micro-nano topography are composed of hills and valleys as shown in figure 2.21. These “valleys” trapped with air can prevent corrosive media e.g. Cl<sup>-</sup> from reaching the bare surface effectively thus providing a good corrosion protection.

Another reason for the anticorrosion property is “capillarity”. According to physical principal and Laplace pressure, when a vertical cylindrical tube is placed in a liquid, the liquid rises and forms a concave surface called a meniscus if the tube is hydrophilic; otherwise the liquid is depressed if the tube is hydrophobic. Corrosive media have a tendency to be pushed out from the pores of the superhydrophobic films. Therefore, this quality contributes to the anti-corrosion properties.

### **2.3.4.3 Fabrication of chemically stable superhydrophobic coatings**

Corrosion behavior is commonly seen on metals and alloy surfaces exposed to corrosive media such as humidity, salt, acid and base, which results in severe damages every year. In the literature, superhydrophobic coatings with rolling-off properties are attracting increasing attention due to the fact that corrosion behavior could be inhibited by the nonconductive air cushion trapped in the micro/nano structure of the superhydrophobic coatings[28, 59-62].

Huang *et al.* [28] successfully prepared superhydrophobic copper stearate surfaces by a one-step electrochemical modification process in an ethanolic stearic acid solution. The corrosion resistance of the samples was investigated via potentiodynamic polarization curves acquired by electrochemical experiments in a 3.5% NaCl solution. By comparing the potentiodynamic polarization curves of the as-received bare copper surface (CA~94°) and electrochemically modified superhydrophobic surface (CA~157°), the corrosion current density dramatically decreased from 36.10  $\mu\text{A}/\text{cm}^2$  to 0.01  $\mu\text{A}/\text{cm}^2$ . At the same time, the corrosion resistance of the superhydrophobic

surface is found to be as high as  $1220 \text{ k}\Omega \text{ cm}^2$  while the as-received bare copper surface is only  $1 \text{ k}\Omega \text{ cm}^2$ . All of the above information indicates that superhydrophobic copper stearate surfaces exhibited much better anti-corrosion properties than as-received copper surfaces.

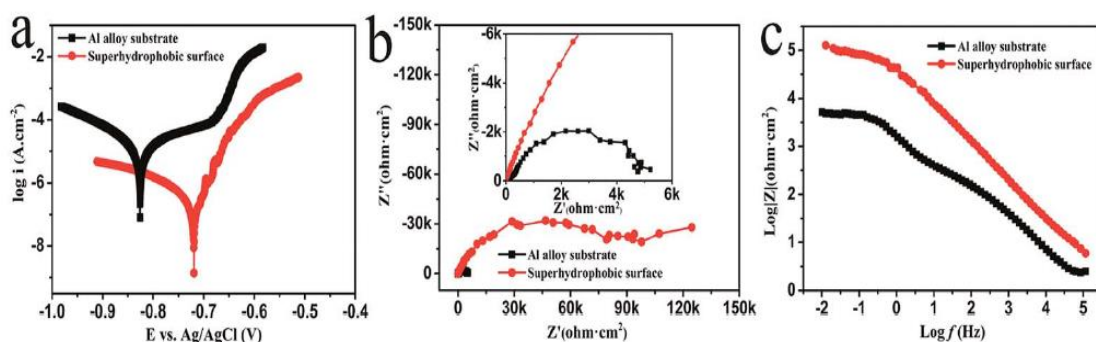


Figure 2. 22 (a) Potentiodynamic polarization curves, (b) Nyquist plots and (c) Bode plots of the bare Al alloy substrate and the as-prepared superhydrophobic surface measured in 3.5 w.t.% NaCl solution [63]

Liu *et al.* [63] fabricated a corrosion resistant superhydrophobic aluminum alloy surface via the method of aluminum anodic oxidation and a self-assembly process by immersing the anodized Al into a fluorinated solution. 3.5 w.t. % NaCl solution was taken as the corrosive medium. The test results were shown in figure 2.22. In figure 2.22 (a), it is obvious that the superhydrophobic surface owns more positive  $E_{\text{corr}}$  and a lower  $I_{\text{corr}}$ . From figure 2.22 (b) Nyquist plots and (c) Bode plots, it can be observed that the superhydrophobic surfaces exhibited larger polarization resistances and a higher impedance modulus as compared with bare Al alloy substrates. These phenomena clearly demonstrated improved corrosion resistance properties.

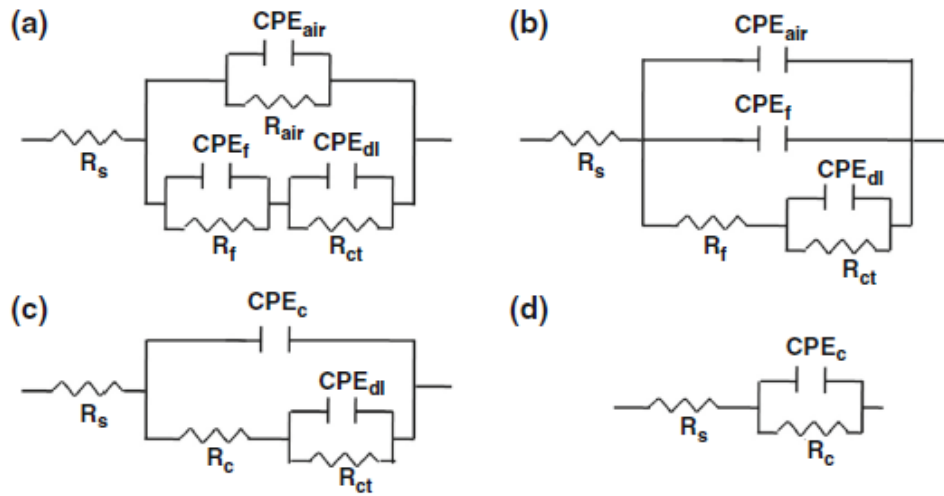


Figure 2. 23 Typical electrical equivalent circuits used for superhydrophobic surfaces [64]

Recently, electrical equivalent circuits (EEC) are frequently employed to better understand the mechanism of the corrosion processes on aluminum, copper, iron and magnesium substrates [29, 59, 61, 64-68]. Figure 2.23 shows the typical electrical equivalent circuits used for simulating the corrosion behavior on superhydrophobic surfaces. In these circuits,  $R_s$  is the solution resistance;  $CPE_{dl}$  and  $R_{ct}$  respectively stand for the capacitance and charge transfer resistances of the double layer formed at the interface between the bare aluminum surface and the corrosive solution. The impedance of the CPE can be expressed as:

$$Z_{CPE} = \frac{1}{Y_0(j\omega)^n} \quad (2.1)$$

where  $Y_0$  is a frequency-independent constant,  $j$  is an imaginary unit,  $\omega$  is an angular frequency ( $\omega = 2\pi f$ ),  $n$  is the CPE exponent ( $0 \leq n \leq 1$ ).

The exponent equals to 1 when the element is a pure capacitor. However, the practical “double layer capacitor” cells behave like a CPE instead of a pure capacitor. The exponent ( $n$ ) for a constant phase element is normally observed to be less than one, due to surface roughness, non-uniform current distribution and ‘leaky’ capacitor etc. In most cases, the constant phase element (CPE) was employed to replace the ideal electrical capacitance due to the fact that the CPE better describes the behaviors of the films having heterogeneities in the microstructure and chemical composition[59]. In order to describe the corrosion behavior correctly, it should be mentioned that electrical equivalent circuits are adjustable based on the results of electrochemical impedance spectroscopy. As an effective supplemental tool, electrical equivalent circuits will surely be used to investigate the corrosion behavior of superhydrophobic coatings fabricated on aluminum substrates in this project.

## Reference

- [1] Hench LL. The Sol-Gel Process. *Chemical reviews*. 1990;90:33-72.
- [2] Pan C, Shen L, Shang S, Xing Y. Preparation of superhydrophobic and UV blocking cotton fabric via sol–gel method and self-assembly. *Applied Surface Science*. 2012;259:110-7.
- [3] Manca M, Cannavale A, De Marco L, Arico AS, Cingolani R, Gigli G. Durable superhydrophobic and antireflective surfaces by trimethylsilanized silica nanoparticles-based sol-gel processing. *Langmuir*. 2009;25:6357-62.
- [4] Guo P, Zhai S, Xiao Z, An Q. One-step fabrication of highly stable, superhydrophobic composites from controllable and low-cost PMHS/TEOS sols for efficient oil cleanup. *Journal of colloid and interface science*. 2015;446:155-62.
- [5] Brassard JD, Sarkar DK, Perron J. Synthesis of monodisperse fluorinated silica nanoparticles and their superhydrophobic thin films. *ACS applied materials & interfaces*. 2011;3:3583-8.



- [6] Basu BJ, Hariprakash V, Aruna ST, Lakshmi RV, Manasa J, Shruthi BS. Effect of microstructure and surface roughness on the wettability of superhydrophobic sol–gel nanocomposite coatings. *Journal of Sol-Gel Science and Technology*. 2010;56:278-86.
- [7] Besra L, Liu M. A review on fundamentals and applications of electrophoretic deposition (EPD). *Progress in Materials Science*. 2007;52:1-61.
- [8] Huang Y, Sarkar DK, Chen XG. Superhydrophobic nanostructured ZnO thin films on aluminum alloy substrates by electrophoretic deposition process. *Applied Surface Science*. 2015;327:327-34.
- [9] Ogihara H, Katayama T, Saji T. One-step electrophoretic deposition for the preparation of superhydrophobic silica particle/trimethylsiloxysilicate composite coatings. *Journal of colloid and interface science*. 2011;362:560-6.
- [10] Song X, Zhai J, Wang Y, Jiang L. Self-assembly of amino-functionalized monolayers on silicon surfaces and preparation of superhydrophobic surfaces based on alkanolic acid dual layers and surface roughening. *Journal of colloid and interface science*. 2006;298:267-73.
- [11] Geng Z, He J, Yao L. Fabrication of robust high-transmittance superamphiphobic coatings through dip-coating followed by spray-coating. *RSC Adv*. 2015;5:89262-8.
- [12] Vashist SK, Lam E, Hrapovic S, Male KB, Luong JH. Immobilization of antibodies and enzymes on 3-aminopropyltriethoxysilane-functionalized bioanalytical platforms for biosensors and diagnostics. *Chemical reviews*. 2014;114:11083-130.
- [13] Schreiber F. Structure and growth of self-assembling monolayers. *Progress in Surface Science*. 2000;65:151-256.
- [14] Chauhan AK, Aswal DK, Koiry SP, Gupta SK, Yakhmi JV, Sürgers C, et al. Self-assembly of the 3-aminopropyltrimethoxysilane multilayers on Si and hysteretic current–voltage characteristics. *Applied Physics A*. 2007;90:581-9.
- [15] Reis FM, de Melo HG, Costa I. EIS investigation on Al 5052 alloy surface preparation for self-assembling monolayer. *Electrochimica Acta*. 2006;51:1780-8.
- [16] Igor Luzinov DJ. Epoxy-Terminated Self-Assembled Monolayers: Molecular Glues for Polymer Layers *Langmuir*. 2000;16:504-16.
- [17] Chen L, Yang B, Zhang J. Preparation and tribological properties of polymer film covalently bonded to silicon substrate via an epoxy-terminated self-assembled monolayer. *Journal of Adhesion Science and Technology*. 2014;28:1725-38.
- [18] Sugimura H, Hozumi A, Kameyama T, Takai O. Organosilane self-assembled monolayers formed at the vapour/solid interface. *Surface and Interface Analysis*. 2002;34:550-4.
- [19] Cho WK, Park S, Jon S, Choi IS. Water-repellent coating: formation of polymeric self-assembled monolayers on nanostructured surfaces. *Nanotechnology*. 2007;18:395602.
- [20] Valipour M N, Birjandi FC, Sargolzaei J. Super-non-wettable surfaces: A review. *Colloids and Surfaces A: Physicochemical and Engineering Aspects*. 2014;448:93-106.
- [21] Huang Y, Sarkar DK, Chen XG. A one-step process to engineer superhydrophobic copper surfaces. *Materials Letters*. 2010;64:2722-4.

- [22] Joung YS, Buie CR. Electrophoretic deposition of unstable colloidal suspensions for superhydrophobic surfaces. *Langmuir*. 2011;27:4156-63.
- [23] Zhao L, Liu WL, Zhang LD, Yao JS, Xu WH, Wang XQ, et al. Fabrication of superhydrophobic and conductive surface based on carbon nanotubes. *Colloids and Surfaces A: Physicochemical and Engineering Aspects*. 2013;423:69-76.
- [24] Yilgor I, Bilgin S, Isik M, Yilgor E. Facile preparation of superhydrophobic polymer surfaces. *Polymer*. 2012;53:1180-8.
- [25] Yan YY, Gao N, Barthlott W. Mimicking natural superhydrophobic surfaces and grasping the wetting process: a review on recent progress in preparing superhydrophobic surfaces. *Advances in colloid and interface science*. 2011;169:80-105.
- [26] Ferrari M, Benedetti A, Santini E, Ravera F, Liggieri L, Guzman E, et al. Biofouling control by superhydrophobic surfaces in shallow euphotic seawater. *Colloids and Surfaces A: Physicochemical and Engineering Aspects*. 2015;480:369-75.
- [27] Ivanova NA, Zaretskaya AK. Simple treatment of cotton textile to impart high water repellent properties. *Applied Surface Science*. 2010;257:1800-3.
- [28] Huang Y, Sarkar DK, Gallant D, Chen XG. Corrosion resistance properties of superhydrophobic copper surfaces fabricated by one-step electrochemical modification process. *Applied Surface Science*. 2013;282:689-94.
- [29] Wang P, Zhang D, Qiu R, Wan Y, Wu J. Green approach to fabrication of a super-hydrophobic film on copper and the consequent corrosion resistance. *Corrosion Science*. 2014;80:366-73.
- [30] Verho T, Bower C, Andrew P, Franssila S, Ikkala O, Ras RH. Mechanically durable superhydrophobic surfaces. *Advanced materials*. 2011;23:673-8.
- [31] Kumar D, Wu X, Fu Q, Ho JWC, Kanhere PD, Li L, et al. Development of durable self-cleaning coatings using organic–inorganic hybrid sol–gel method. *Applied Surface Science*. 2015;344:205-12.
- [32] Xu QF, Wang JN, Sanderson KD. A general approach for superhydrophobic coating with strong adhesion strength. *Journal of Materials Chemistry*. 2010;20:5961.
- [33] Yuan Z, Bin J, XianWang, Wang M, Huang J, Peng C, et al. Preparation of a polydimethylsiloxane (PDMS)/CaCO<sub>3</sub> based superhydrophobic coating. *Surface and Coatings Technology*. 2014;254:97-103.
- [34] She Z, Li Q, Wang Z, Li L, Chen F, Zhou J. Researching the fabrication of anticorrosion superhydrophobic surface on magnesium alloy and its mechanical stability and durability. *Chemical Engineering Journal*. 2013;228:415-24.
- [35] Zhu X, Zhang Z, Men X, Yang J, Wang K, Xu X, et al. Robust superhydrophobic surfaces with mechanical durability and easy repairability. *Journal of Materials Chemistry*. 2011;21:15793.
- [36] Wang FJ, Lei S, Ou JF, Xue MS, Li W. Superhydrophobic surfaces with excellent mechanical durability and easy repairability. *Applied Surface Science*. 2013;276:397-400.
- [37] Lakshmi RV, Bharathidasan T, Basu BJ. Superhydrophobic sol–gel nanocomposite coatings with enhanced hardness. *Applied Surface Science*. 2011;257:10421-6.
- [38] Mohamed AMA, Abdullah AM, Younan NA. Corrosion behavior of superhydrophobic surfaces: A review. *Arabian Journal of Chemistry*. 2014.

- [39] Wang CF, Tzeng FS, Chen HG, Chang CJ. Ultraviolet-durable superhydrophobic zinc oxide-coated mesh films for surface and underwater-oil capture and transportation. *Langmuir*. 2012;28:10015-9.
- [40] Xiu Y, Hess DW, Wong CP. UV and thermally stable superhydrophobic coatings from sol-gel processing. *Journal of colloid and interface science*. 2008;326:465-70.
- [41] Nishimoto S, Becchaku M, Kameshima Y, Shirosaki Y, Hayakawa S, Osaka A, et al. TiO<sub>2</sub>-based superhydrophobic–superhydrophilic pattern with an extremely high wettability contrast. *Thin Solid Films*. 2014;558:221-6.
- [42] Zhang X, Guo Y, Zhang Z, Zhang P. Self-cleaning superhydrophobic surface based on titanium dioxide nanowires combined with polydimethylsiloxane. *Applied Surface Science*. 2013;284:319-23.
- [43] Xinjian Feng LF, Meihua Jin, Jin Zhai, Lei Jiang,\* and Daoben Zhu. Reversible Super-hydrophobicity to Super-hydrophilicity Transition of Aligned ZnO Nanorod Films. *J AM CHEM SOC*. 2004;126:62-3.
- [44] Hou W, Wang Q. UV-driven reversible switching of a polystyrene/titania nanocomposite coating between superhydrophobicity and superhydrophilicity. *Langmuir*. 2009;25:6875-9.
- [45] Ding X, Zhou S, Gu G, Wu L. A facile and large-area fabrication method of superhydrophobic self-cleaning fluorinated polysiloxane/TiO<sub>2</sub> nanocomposite coatings with long-term durability. *Journal of Materials Chemistry*. 2011;21:6161.
- [46] Luttrell T, Halpegamage S, Tao J, Kramer A, Sutter E, Batzill M. Why is anatase a better photocatalyst than rutile?--Model studies on epitaxial TiO<sub>2</sub> films. *Scientific reports*. 2014;4:4043.
- [47] Isimjan TT, Wang T, Rohani S. A novel method to prepare superhydrophobic, UV resistance and anti-corrosion steel surface. *Chemical Engineering Journal*. 2012;210:182-7.
- [48] Mao Z, Shi Q, Zhang L, Cao H. The formation and UV-blocking property of needle-shaped ZnO nanorod on cotton fabric. *Thin Solid Films*. 2009;517:2681-6.
- [49] Wang L, Zhang X, Fu Y, Li B, Liu Y. Bioinspired preparation of ultrathin SiO<sub>2</sub> shell on ZnO nanowire array for ultraviolet-durable superhydrophobicity. *Langmuir*. 2009;25:13619-24.
- [50] Wang L, Zhang X, Li B, Sun P, Yang J, Xu H, et al. Superhydrophobic and ultraviolet-blocking cotton textiles. *ACS applied materials & interfaces*. 2011;3:1277-81.
- [51] Duan W, Xie A, Shen Y, Wang X, Wang F, Zhang Y, et al. Fabrication of Superhydrophobic Cotton Fabrics with UV Protection Based on CeO<sub>2</sub> Particles. *Industrial & Engineering Chemistry Research*. 2011;50:4441-5.
- [52] Pashinin AS, Zolotarevskii VI, Kiselev MR, Emel'yanenko AM, Boinovich LB. Thermal stability of superhydrophobic coatings. *Doklady Physical Chemistry*. 2011;436:19-22.
- [53] Mahadik SA, Mahadik DB, Kavale MS, Parale VG, Wagh PB, Barshilia HC, et al. Thermally stable and transparent superhydrophobic sol-gel coatings by spray method. *Journal of Sol-Gel Science and Technology*. 2012;63:580-6.
- [54] Li J, Weng R. Preparation of Nano-SiO<sub>2</sub> / amino-modified polysiloxane hybrid superhydrophobic coating and thermal-stability characterization. *Journal of Wuhan University of Technology-Mater Sci Ed*. 2014;29:35-9.

- [55] Deng X, Mammen L, Zhao Y, Lellig P, Mullen K, Li C, et al. Transparent, thermally stable and mechanically robust superhydrophobic surfaces made from porous silica capsules. *Advanced materials*. 2011;23:2962-5.
- [56] Gong G, Wu J, Liu J, Sun N, Zhao Y, Jiang L. Bio-inspired adhesive superhydrophobic polyimide mat with high thermal stability. *Journal of Materials Chemistry*. 2012;22:8257.
- [57] Tao Liu SC, Sha Cheng, Jintao Tian, Xueting Chang, Yansheng Yin \*. Corrosion behavior of superhydrophobic surface on copper in seawater. *Electrochimica Acta*. 2007;52:8003-7.
- [58] S. Khorsand KR, F. Ashrafizadeh. Corrosion resistance and long-term durability of superhydrophobic nickel film prepared by electrodeposition process. *Applied Surface Science*. 2014;305:498-505.
- [59] Boinovich LB, Gnedenkov SV, Alpysbaeva DA, Egorkin VS, Emelyanenko AM, Sinebryukhov SL, et al. Corrosion resistance of composite coatings on low-carbon steel containing hydrophobic and superhydrophobic layers in combination with oxide sublayers. *Corrosion Science*. 2012;55:238-45.
- [60] Esmailzadeh S, Khorsand S, Raeissi K, Ashrafizadeh F. Microstructural evolution and corrosion resistance of superhydrophobic electrodeposited nickel films. *Surface and Coatings Technology*. 2015;283:337-46.
- [61] Huang Y, Sarkar DK, Grant Chen X. Superhydrophobic aluminum alloy surfaces prepared by chemical etching process and their corrosion resistance properties. *Applied Surface Science*. 2015;356:1012-24.
- [62] Liu Q, Chen D, Kang Z. One-step electrodeposition process to fabricate corrosion-resistant superhydrophobic surface on magnesium alloy. *ACS applied materials & interfaces*. 2015;7:1859-67.
- [63] CansenLiu FaJL. Facile fabrication of a robust and corrosion resistant superhydrophobic aluminum alloy surface by a novel method. *The Royal Society of Chemistry*. 2014;4:555556-55564.
- [64] Zhang D, Wang L, Qian H, Li X. Superhydrophobic surfaces for corrosion protection: a review of recent progresses and future directions. *Journal of Coatings Technology and Research*. 2015;13:11-29.
- [65] Liu Y, Zhang J, Li S, Wang Y, Han Z, Ren L. Fabrication of a superhydrophobic graphene surface with excellent mechanical abrasion and corrosion resistance on an aluminum alloy substrate. *RSC Adv*. 2014;4:45389-96.
- [66] Ishizaki T, Hieda J, Saito N, Saito N, Takai O. Corrosion resistance and chemical stability of superhydrophobic film deposited on magnesium alloy AZ31 by microwave plasma-enhanced chemical vapor deposition. *Electrochimica Acta*. 2010;55:7094-101.
- [67] Jorcin J-B, Orazem ME, Pébère N, Tribollet B. CPE analysis by local electrochemical impedance spectroscopy. *Electrochimica Acta*. 2006;51:1473-9.
- [68] Xu N, Sarkar DK, Chen XG, Tong WP. Corrosion performance of superhydrophobic nickel stearate/nickel hydroxide thin films on aluminum alloy by a simple one-step electrodeposition process. *Surface and Coatings Technology*. 2016;302:173-84.

## **3. Experimental**

### **3.1 Materials**

AA6061 aluminum alloys (Al-Mg-Si alloys) have been widely used in the aircraft, marine and automotive industries due to their excellent strength and light weight properties, which will be principally investigated in this project. The chemical composition of AA 6061 aluminum alloy is Al 97.9 wt.%, Mg 1.08 wt.%, Si 0.63 wt.%, Mn 0.52 wt.%, Cu 0.32 wt.%, Fe 0.17 wt.%, Ti 0.02 wt.% and V 0.01 wt.%. The mechanically-polished and as-received aluminum alloy substrates were degreased by ultrasonication in dilute LIQUINOX solution (1 vol. %) for 15 min followed by rinsing in ethanol and de-ionized water for 30 min, respectively. Then the aluminum samples were dried for 24 h at 70 °C.

### **3.2 Sample preparation**

#### **3.2.1 Fabrication of superhydrophobic cobalt stearate thin films by electrodeposition**

The aluminum (AA6061 alloy) substrates with a size of one by two inches were ultrasonically degreased in a soap solution and cleaned in ethanol as well as deionized water for 30 min. Subsequently, the electrodeposition process was performed at room temperature under a voltage of 10 V (DC) for 10 min, where the cleaned aluminum substrate was used as the cathode and the graphite plate as the anode. During the electrodeposition process, the cathode and the anode were separated by a distance of

1.5 cm, as shown in Figure 3. 1. The electrolyte solution was composed of cobalt (II) nitrate hexahydrate ( $\text{Co}(\text{NO}_3)_2 \cdot 6\text{H}_2\text{O}$ ) and stearic acid ( $\text{CH}_3(\text{CH}_2)_{16}\text{COOH}$ ) in ethanol. After deposition, the sample was carefully removed from the electrolyte and dried at  $70^\circ\text{C}$  on the hotplate for 24 hours

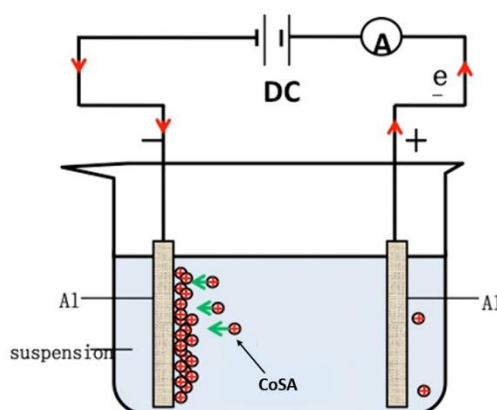


Figure 3. 1 The schematic model for preparation of cobalt stearate (CoSA) by electrodeposition

### 3.2.2 Fabrication of superhydrophobic films incorporating $\text{TiO}_2$ nanoparticles by sol-gel process

The square aluminum (AA6061 alloy) substrates with a size of one by one inches were ultrasonically degreased in a soap solution and cleaned in ethanol as well as deionized water for 30 min. First, in order to prepare the PMHS sol-gel, 2 mL PMHS and 3mL ammonia (28%) were added into ethanol and stirred at room temperature for 2 days. Second, to prepare the PMHS/ $\text{TiO}_2$  sol-gel, 1.5 g anatase  $\text{TiO}_2$  nanoparticle (average particle size: 100 nm) were dispersed into 51 mL of ethanol, followed by ultrasonication for 1h. Then 25 mL PMHS sol-gel were added into the  $\text{TiO}_2$  nanoparticles ethanolic solution. The mixture was aged for 5 days while stirring at room

temperature before being subjected to the spin-coating process. In the case of preparing PMHS/TiO<sub>2</sub>@CoSA sol-gel, TiO<sub>2</sub>, 1.5 g anatase TiO<sub>2</sub> nanoparticle (average size : 100nm) were dispersed in the same volume of 51 mL mixed ethanolic solution composed of 17 mL cobalt nitrate (0.01 M) and 34 mL stearic acid (0.01 M) as well as with 150 μL of ammonia (28%), followed by ultrasonication for 1h. The mixture was also stirred and aged for 5 days at room temperature before the spin-coating process.



Figure 3. 2 Photograph of Single Wafer Spin Processor

The spin-coating process were carried out using a Single Wafer Spin Processor (Laurell Technologies WS-650Sz-6NPP-Lite), as shown in Figure 3. 2. PMHS/TiO<sub>2</sub> and PMHS/TiO<sub>2</sub>@CoSA sol-gels were used to make spin-coatings with 600uL per layer on the clean, square aluminum substrates respectively. The spin process includes 10 seconds of 500 rounds per minute (RPM) and 10 seconds of 1000 RPM.

### 3.2.3 SAM modified aluminum substrates for improved adhesion properties

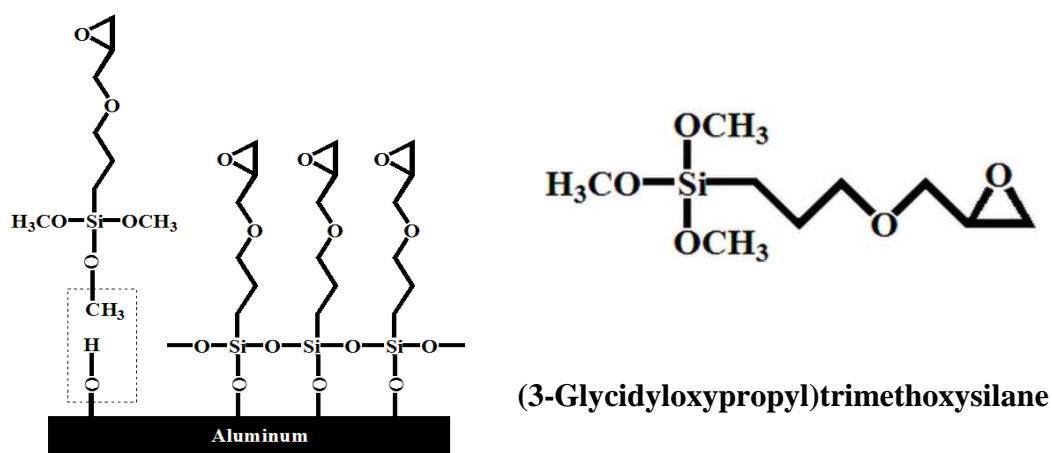


Figure 3. 3 The Schematic diagram of a self-assembled monolayer of GPTS

In Figure 3.3, One-inch-square aluminum (AA6061 alloy) substrates were ultrasonically degreased in a soap solution and cleaned in deionized water for 30 min. The clean Al substrates were prepared with etching in a 1 M sodium hydroxide alkaline solution for 5 min at room temperature, followed by oxide removal via an immersion in 10 vol. %  $\text{HNO}_3$  for one minute as well as rinsing in deionized water and ethanol followed by drying at room temperature. An ethanolic solution containing 1 vol. % GPTS organosilane was prepared by stirring the mixture for 30 min before spin-coating. This solution was poured on the Al substrates, covering them completely before the spinning was started. The spin coated GPTS films on aluminum substrates were dried at  $110^\circ\text{C}$ , on a hotplate. This sample is called SAM/Al substrate in this work.



The presence of SAMs was investigated via electrochemical experiments including open circuit potential (OCP), electrochemical impedance spectroscopy (EIS) and potentiodynamic polarization experiments (Tafel) in a  $1.0 \times 10^{-4}$  M NaOH solution (pH 10). Electrochemical experiments were carried out on a PGZ100 potentiostat and a 300 cm<sup>3</sup> –EG&G PAR flat cell (London Scientific, London, ON, Canada), equipped with a standard three-electrode system with an Ag/AgCl reference electrode, a platinum mesh as the counter electrode, and the sample as the working electrode at room temperature.

### **3.3 Characterization: Wettability, Topography, Morphology and Structure, Chemical composition, Corrosion behavior analysis and UV degradation behavior analysis**

(1) Surface wettability: The surface wettability of samples was conducted by measuring static and dynamic contact angles of 10  $\mu$ L water drops using a First Ten Angstrom contact angle goniometer at GRTB, Chicoutimi (Figure 3.4). The difference between the advancing and receding contact angles provides the contact angle hysteresis. The advancing and receding contact angles are measured by holding the needle stationary and moving the sample in one direction.

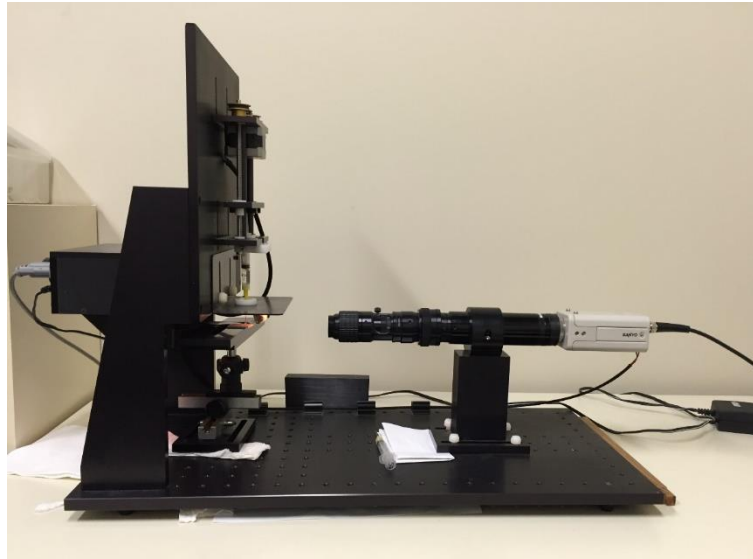


Figure 3. 4 Photograph of contact angle goniometer

(2) Surface topography: The roughness measurements were carried out on the MicroXAM-100 HR 3D surface profilometer (Figure 3.5) at CURAL, Chicoutimi.

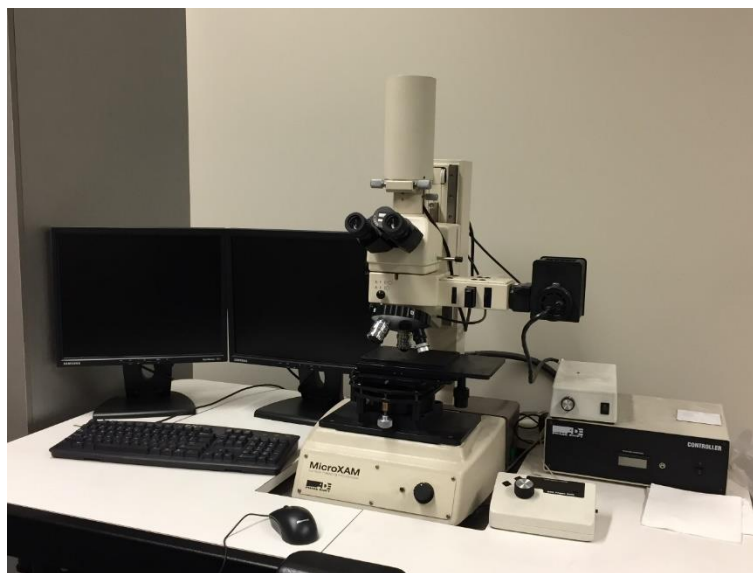


Figure 3. 5 Photograph of 3D surface optical profilometer

(3) Surface morphology: The morphological and elemental analyses of the aluminum

substrates coated by spin-coatings were performed using a scanning electron microscope (SEM, JEOL JSM-6480 LV) equipped with energy dispersive X-ray spectroscopy (EDX), as seen in Figure 3.6.



Figure 3. 6 Photograph of scanning electron microscope

(4) Image analysis: The images analysis were performed on the optical microscope equipped with a digital camera (Nikon ME 600) and an image analysis system (CLEMEX JS-2000, PE4.0), as illustrated in Figure 3.7.

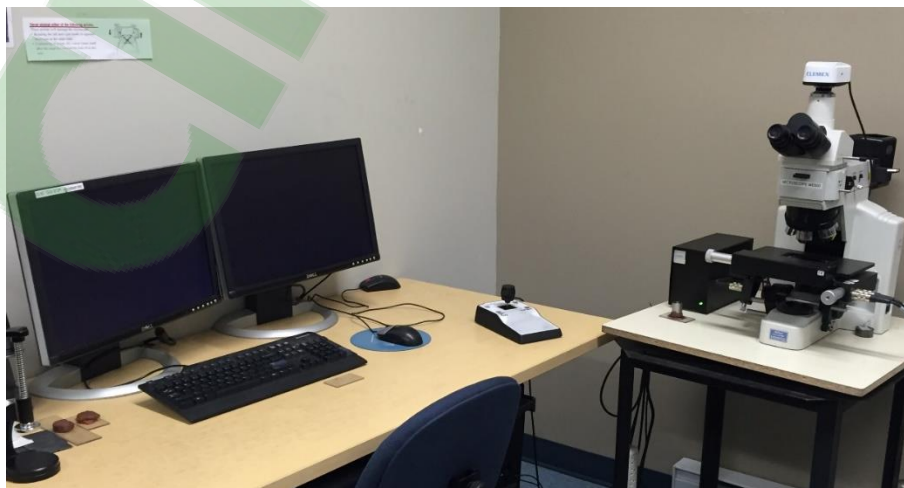


Figure 3. 7 Photograph of image analysis system

(5) Chemical composition and structure: The chemical composition and structure were analyzed by Attenuated Total Reflectance, Fourier transform infrared spectroscopy (ATR, Agilent Technologies Cary 630 FTIR) as well as by X-ray diffraction (XRD, D8 discover with Cu K $\alpha$  wavelength 0.154 nm), as shown in Figure 3.8 and Figure 3.9 respectively.

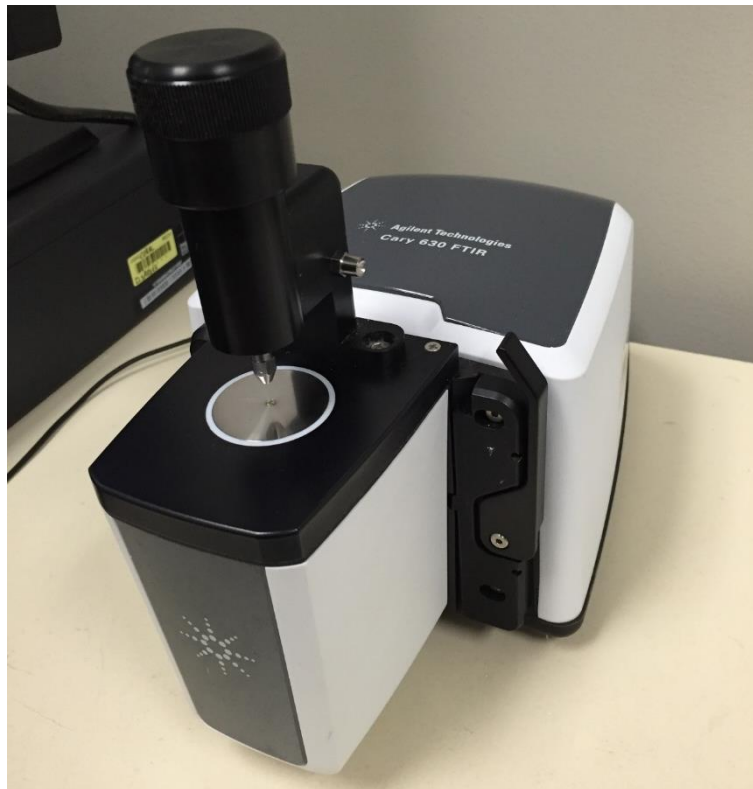


Figure 3. 8 Photograph of Attenuated Total Reflectance system

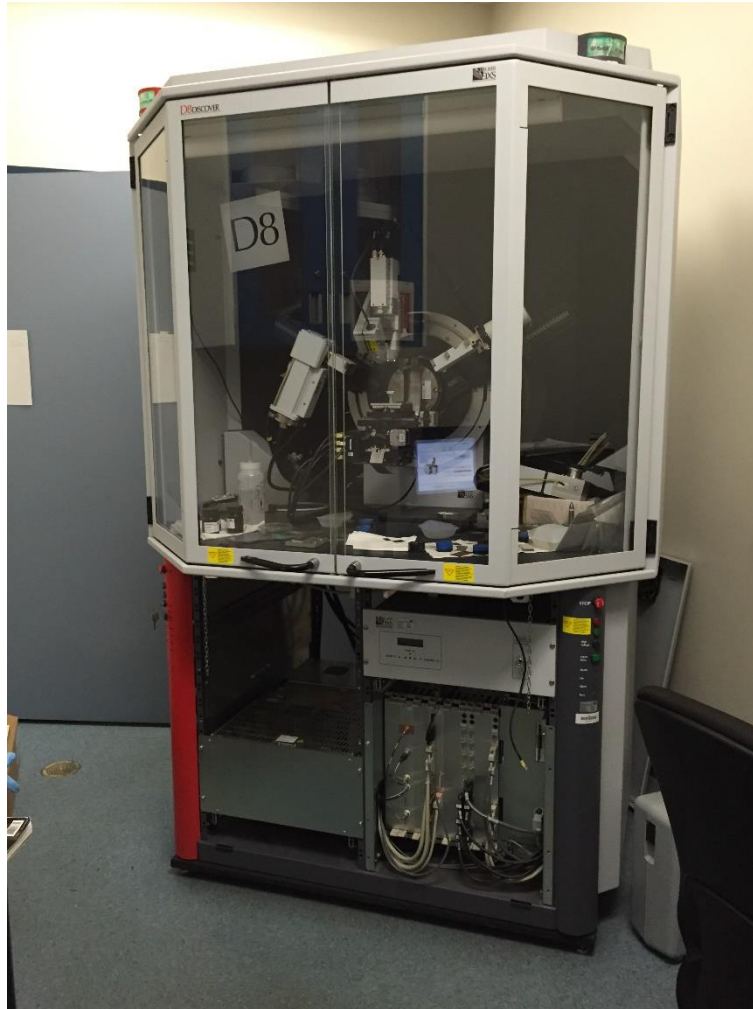


Figure 3. 9 Photograph of X-ray diffraction system

(6) Corrosion behavior analysis: The corrosion behavior of these samples was investigated via electrochemical experiments including open circuit potential (OCP), electrochemical impedance spectroscopy (EIS) and potentiodynamic polarization in a 3.5 wt.% NaCl aqueous solution (natural pH 5.9). Electrochemical experiments were carried out on a PGZ100 potentiostat and a 300 cm<sup>3</sup> –EG&G PAR flat cell (London Scientific, London, ON, Canada), equipped with a standard three-electrode system with an Ag/AgCl reference electrode, a platinum mesh as the counter electrode, and the sample as the working electrode at room temperature. The corrosion tests have been

shown in Figure 3.10.

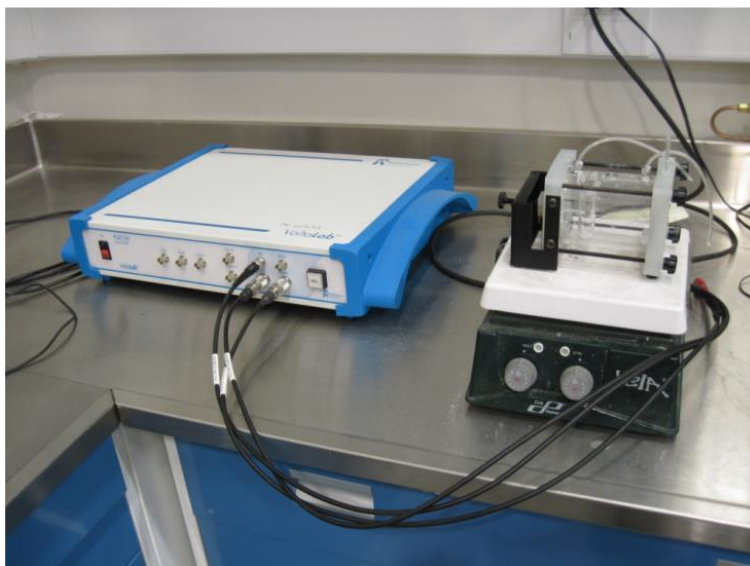


Figure 3. 10 Photograph of corrosion test

(7) UV degradation behavior analysis: A home designed UV illumination technique (15Watt, UV light wavelength of 302 nm and 365 nm) was used to understand the UV degradation behavior of the superhydrophobic coatings which incorporate TiO<sub>2</sub> nanoparticles, as illustrated in Figure 3.11.



Figure 3. 11 Photograph of UV degradation test

(8) UV-Vis absorption technique: UV-Vis spectroscopy was utilized to analyze the absorption intensity in the region of ultraviolet and visible light in the scanning range of 190nm-900nm. The instrument is shown in Figure 3. 12.



Figure 3. 12 Photograph of UV-Vis spectroscopy

# **4. Corrosion resistant superhydrophobic cobalt stearate thin films coated aluminum alloys by electrodeposition**

## **4.1 Introduction**

Superhydrophobic surfaces, inspired by the self-cleaning lotus leaf, demonstrated a water contact angle of more than 150° and a sliding angle of less than 10°. The non-wettability property is ascribed to their micro-nano topography and low-surface-energy, which can promote the entrapment of the air in the space between the rough features. Superhydrophobic surfaces have attracted a great deal of interest in the aspects of fundamental research and practical applications due to their unique characteristics such as anti-corrosion, oil-water separation, anti-icing. In recent times, various methods to construct super-hydrophobic metallic film have been reported including lithography and templating techniques [1], sol-gel[2], electrophoretic deposition[3], chemical etching[4], self-assembly and self-organization [5] *etc.*

Aluminum and its alloys, with their excellent properties including high-specific strength and low-specific weight, have attracted considerable interest for a number of applications, such as the aerospace, machinery manufacturing and electronic industries. However, due to their great affinity to water owing to the high surface energy, aluminum alloys are highly susceptible to corrosion especially in damp environments. Recently, many reports have proved that superhydrophobic surfaces are effective in preventing aluminum alloy corrosion. Liang *et al.*[6] prepared a superhydrophobic silica-based



surface on aluminum substrate in combination of tetraethylorthosilicate and vinyltriethoxysilane as co-precursor by sol-gel method. The superhydrophobic treatment was proved to be effective for improving the anti-corrosion properties of aluminum through the synergistic effect of superhydrophobic property and silica-based oxide film as corrosion barrier. N. Saleema *et al.*[7] fabricated a superhydrophobic aluminum alloy surface via one-step process by immersing the substrates into an aqueous solution containing sodium hydroxide as well as fluoralkylsilane. Similarly, in a study of Ying *et al.*[4], superhydrophobic aluminum alloy substrates with improved corrosion resistance properties were prepared by chemical etching using alkaline NaOH solution followed by passivation with ethanolic stearic acid solution. The key to fabricating these superhydrophobic films lies in a rough surface created by chemical etching which is further passivated with a low-surface-energy material. Liu *et al.*[8] reported a superhydrophobic graphene surface on aluminum by using a spin-film method. The graphene coated Al alloy showed a more positive corrosion potential and a lower current density compared with bare Al, indicating superhydrophobic surfaces play a significant role in preventing metal corrosion.

Cobalt is usually utilized in the preparation of magnetic nanoparticles and high-strength alloys. The literature also showed cobalt has great potential in the application of supercapacitors due to its electrochemical high-capacitance properties. Inspired from these, a superhydrophobic surface containing cobalt could be a terrific barrier protecting metal alloy substrates from corrosion. Nevertheless, most current cobalt films resulted in poor anti-corrosion and self-cleaning properties. Superhydrophobic

surfaces incorporating the element cobalt are rarely seen. In recent times, cobalt superhydrophobic films are gradually drawing more researchers' attention. Qiu *et al.*[9] reported that wettability property of Co crystal surfaces can be changed from hydrophilicity to superhydrophobicity via carefully controlling the film microstructures by adjusting the electrodeposition parameters including the potential, concentration and temperature. However, in a similar experiment, the as-prepared electrodeposited nanostructured cobalt film reported by Xiao *et al.*[10] was found to be superhydrophilic. In their process, stearic acid was used to modulate the wettability of the cobalt film featured of shell-like structure to superhydrophobicity. Additionally, Moulapanah *et al.* [11] have prepared hydrophilic  $\text{Co}_3\text{O}_4$  nanoparticles by sol-gel method and further modified them with stearic acid to fabricate a superhydrophobic surface on the glass substrate. However, this method required multi-steps and was time-consuming. Similar case was reported by Basu *et al.* [12], superhydrophobic cobalt hydroxide films were fabricated in the way incorporating chemical-bath deposition and immersion in stearic acid ethanolic solution. .

From these reports [9-12], it is worth mentioning that superhydrophobic films based on pure cobalt crystal are not easy to acquire and definitely require a very fine control of electrodeposition parameters. In most cases, after the formation of a surface with a micro/nanostructured roughness, a following process of modification with low-surface-energy organic acid is usually implemented.

To simplify the fabrication procedure, a simple, one-step electrodeposition method was adapted to fabricate superhydrophobic cobalt films on aluminum alloy

substrate by incorporating cobalt nitrite with stearic acid in this work. Electrodeposition is regarded as an effective technique to create artificial superhydrophobic surfaces because of its many advantage such as easy control, simplicity, low cost, and the ability to make complicated or large-area surfaces. It should be mentioned that a series of superhydrophobic surfaces synthesized in the bath of organic acid as well as inorganic salt containing metallic ions such as  $\text{Cu}^{2+}$ ,  $\text{Ce}^{3+}$ ,  $\text{Mn}^{2+}$ ,  $\text{Ni}^+$ ,  $\text{La}^{3+}$  etc. have been created, inspired from our developed one-step electrochemical method [13-17]. For example, Chen *et al.*[13] utilized one-step electrodeposition and successfully prepared a superhydrophobic manganese ( $\text{Mn}^{2+}$ ) myristate film on copper substrate in an ethanolic solution containing manganese chloride and myristic acid. Liu *et al.*[14] reported the effect of electrodeposition potential and time on the wettability as well as morphology of superhydrophobic cerium myristate films ( $\text{Ce}(\text{CH}_3(\text{CH}_2)_{12}\text{COO})_3$ ) obtained from an ethanolic solution with cerium nitrate hexahydrate and myristic acid by a one-step electrodeposition process. The anti-corrosion property of this thin film was evaluated in four different corrosive solutions,  $\text{NaCl}$ ,  $\text{Na}_2\text{SO}_4$ ,  $\text{NaNO}_3$  and  $\text{NaClO}_3$ . However, fabrication of superhydrophobic surface with cobalt salt by a one-step process is rarely seen. In another work by Chen *et al.*[18], a superhydrophobic powder films composed of cobalt myristate and pure cobalt nucleus was fabricated on cathodic stainless steel by electrodeposition under 30 V DC voltages in a mixed solution of cobalt chloride and myristic acid. Nevertheless, they did not study the corrosion behavior of their superhydrophobic cobalt powder film, which is regarded as one of the most important application of superhydrophobic surfaces.

Therefore, in the present study, a superhydrophobic surface was successfully fabricated on cathodic aluminum alloy substrates using a simple one-step process involving the electrochemical modification of the aluminum substrates in varied molar ratios of Co/SA in ethanolic solution containing cobalt nitrite and stearic acid under a DC voltage of 10V. The influences of the molar ratios of Co/SA in the electrolyte on the morphology, chemical composition and wettability of the film have been characterized carefully. A series of characterizations were used to analyze the formation of cobalt stearate and cobalt oxide during the electrodeposition process. Based on our observation, aluminum substrates modified by electrodeposition in the mixed solution with a Co/SA molar ratio of 0.2 demonstrated the best non-wetting properties and a plausible mechanism of two simultaneous reactions have been illustrated clearly to explain this phenomenon. Furthermore, we studied the corrosion resistance property of the film by potentiodynamic polarization and electrochemical impedance spectroscopy (EIS).

## **4.2 Experimental**

The aluminum (AA6061 alloy) substrates with a size of one by two inches were ultrasonically degreased in a soap solution and cleaned in ethanol as well as deionized water for 30 min. Subsequently, the electrodeposition process was performed at room temperature under a voltage of 10 V (DC) for 10 min, where the cleaned aluminum substrate was used as the cathode and the graphite plate as the anode. During the electrodeposition process, the cathode and the anode were separated by a distance of

1.5 cm. The electrolyte solution was composed of cobalt (II) nitrate hexahydrate ( $\text{Co}(\text{NO}_3)_2 \cdot 6\text{H}_2\text{O}$ ) and stearic acid ( $\text{CH}_3(\text{CH}_2)_{16}\text{COOH}$ ) in ethanol. After deposition, the sample was carefully removed from the electrolyte and dried at  $70^\circ\text{C}$  on the hotplate for 24 hours.

The morphological and elemental analyses of the modified cathodic aluminum substrates were performed using a scanning electron microscope (SEM, JEOL JSM-6480 LV) equipped with energy dispersive X-ray spectroscopy (EDX). The chemical composition as well as structure were analyzed by X-ray diffraction (XRD, D8 discover with  $\text{Cu K}\alpha$  wavelength 0.154 nm) as well as by Attenuated Total Reflectance (ATR, Agilent Technologies Cary 630 FTIR). The surface wettability of the coated samples was conducted by measuring static and dynamic contact angles of 10  $\mu\text{L}$  water drop using a First Ten Angstrom contact angle goniometer. The roughness measurements were carried out on the MicroXAM-100 HR 3D surface profilometer. The corrosion behavior of these samples was investigated via electrochemical experiments including open circuit potential (OCP), electrochemical impedance spectroscopy (EIS) and potentiodynamic polarization experiments in a 3.5 wt.% NaCl aqueous solution (natural pH 5.9). Electrochemical experiments were carried out on a PGZ100 potentiostat and a 300  $\text{cm}^3$  –EG&G PAR flat cell (London Scientific, London, ON, Canada), equipped with a standard three-electrode system with a Ag/AgCl reference electrode, a platinum mesh as the counter electrode, and the sample as the working electrode at room temperature. EIS measurements were conducted over the frequency range from 100 kHz to 10 mHz with a sinusoidal signal amplitude of 10 mV with respect to OCP

collecting 20 data per decade. The potentiodynamic polarization curves were scanned from -250 mV to +1000 mV with respect to OCP. It is to mention that the OCP was monitored approximately 24 h before performing EIS. The impedance  $Z$  of the system is composed of a real and an imaginary resistance, given by the following equations,

$$Z = Z_{real} + j Z_{imaginary} \quad (4.1)$$

Or 
$$Z = Z' + j Z'' \quad (4.2)$$

The modulus of the impedance  $|Z|$  and the phase angle  $\phi$  are defined as

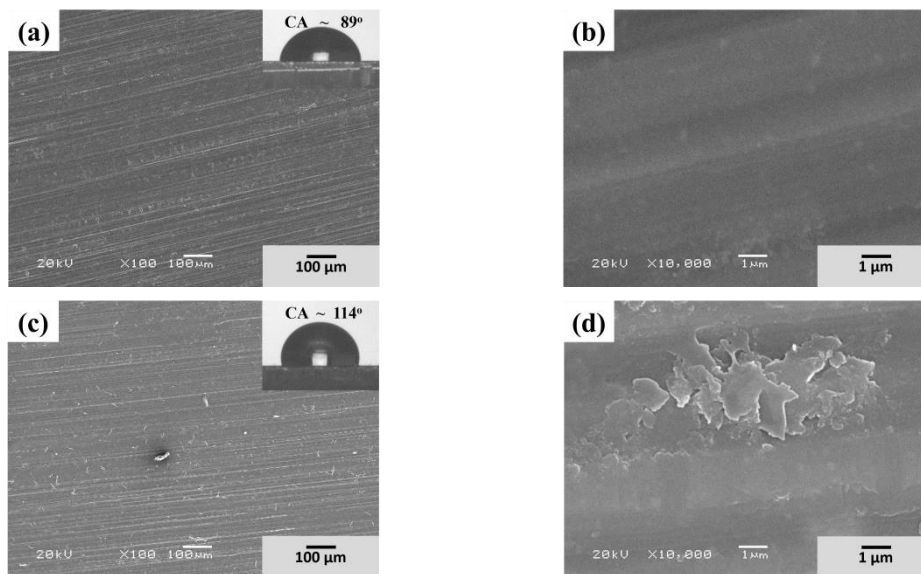
$$|Z| = \sqrt{Z'^2 + Z''^2} \quad (4.3)$$

$$\phi = \arctan\left(\frac{|Z_{imaginary}|}{Z_{real}}\right) \quad (4.4)$$

where  $j = \sqrt{-1}$ ,  $Z_{real}$  or  $Z'$  is the real impedance;  $Z_{imaginary}$  or  $Z''$  is the imaginary impedance.

## 4.3 Results and discussion

### 4.3.1 Surface morphology and wetting



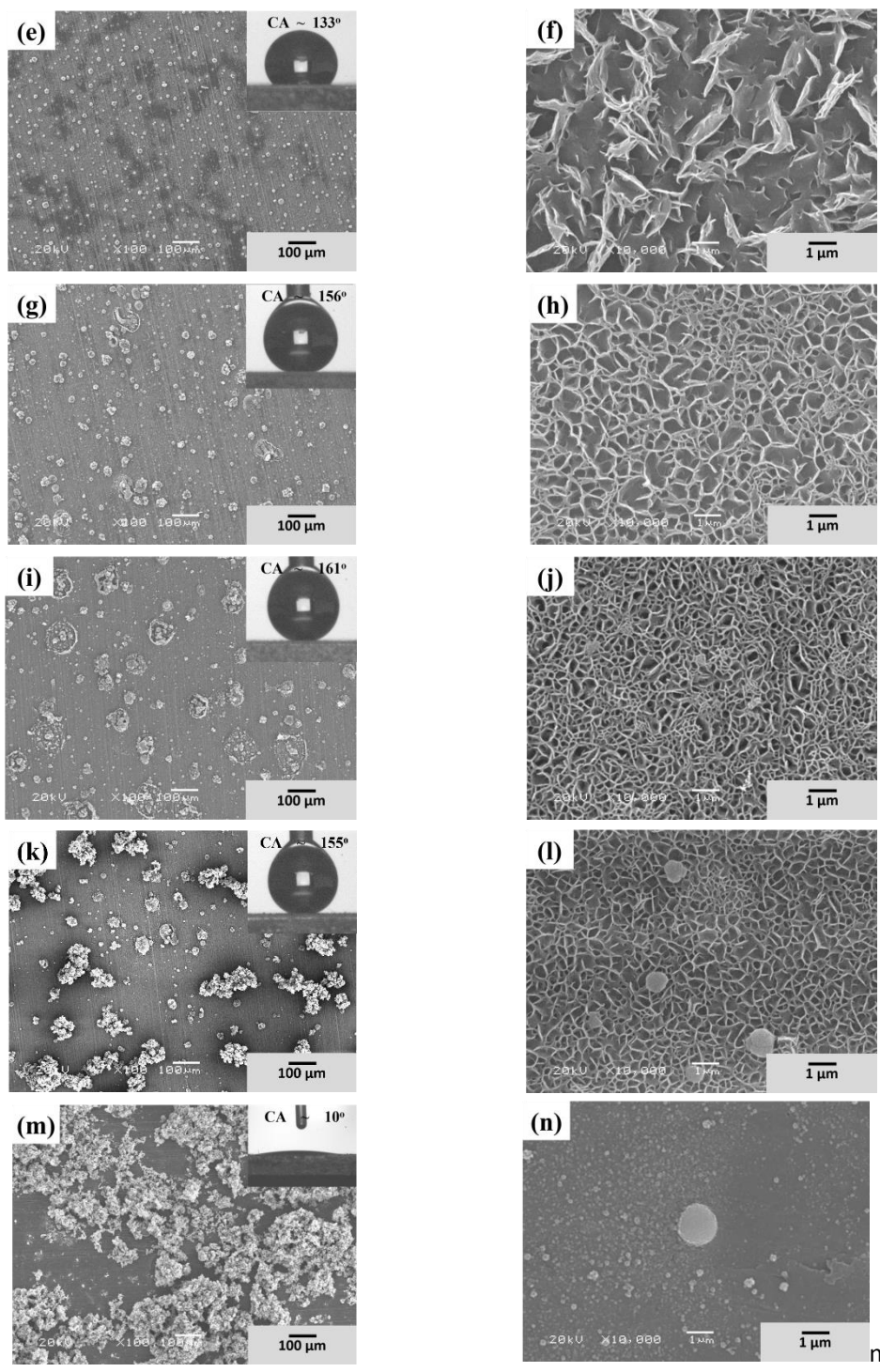


Figure 4. 1 SEM images (left column) of (a) as-received aluminum substrate and electrodeposited cathodic aluminum substrates with the application of 10V DC voltage for 10 min in the Co (II)/SA ethanolic solution with molar ratios of (c) 0, (e) 0.02, (g) 0.08, (i) 0.2, (k) 0.5 and (m)  $\infty$ . The insets show the images of water

drops on respective surfaces. The molar ratio  $\infty$  represents a pure solution of Co(II) ions in ethanolic solution having concentration of 0.01 M. The SEM images (right column) in high magnification (b), (d), (f), (h), (j), (l), (n) correspond to those at lower magnification in the left column

Figure 4.1 (a) and (b) show the SEM surface images of as-received clean aluminum substrates in low and high magnifications, respectively. The inherent rolling lines, which is common to be seen on rolled sheets, are generally seen on aluminum surfaces having a surface roughness of  $0.64 \mu\text{m}$  and a water contact angle of  $89 \pm 2^\circ$  (as shown in the inset of SEM image). Several pattern-like films were present on the clean aluminum surface after electrodeposition using 0.01 M steric acid ethanolic solution as shown in Figure 4.1 (c) and (d). The water contact angle on SA modified Al surface increased to  $114 \pm 7^\circ$  due to the low surface energy of steric acid. Interestingly, Figure. 4.1 (e) shows that the aluminum surface was covered by a thin film of discontinuous clustered morphology of approximately,  $10 \mu\text{m}$  when electrodeposited when using Co(II)/SA solution of molar ratio of 0.02. The Figure 4.1 (f) shows that each individual cluster is composed of leaf-like cobalt stearate. The contact angle of water is found to be  $132 \pm 3^\circ$  on this surface as shown in the inset of in Figure 4.1 (e). When the molar ratio of Co(II)/SA increases to 0.08, larger clusters are visible as shown in Figure 4.1 (g). In this case, the cobalt stearate thin film covers the bare aluminum surface completely, providing a water contact angle of  $156 \pm 2^\circ$ . The leaf-like cobalt stearate transitioned into a honeycomb-like framework due to the increase of Co (II)



ions in the solution. The image analysis shows that the xx solid fraction of the surface is covered by the cobalt stearate. Therefore, when the Co/SA molar ratio was increased to 0.2 (Figure. 4.1 (i) and (j)), as expected, more cobalt stearate formed a compact honeycomb-like framework on the aluminum surfaces. Under the lower magnification, when compared with a Co/SA molar ratio of 0.08, more and larger star-like clusters were assembled on top of the cobalt stearate films, and two tiny nano-sized clusters were also observed. Meanwhile, approximately ten round pits, which seemed to have denser star-like clusters inside, formed on the surface. The contact angle of water on this surface also increased to the maximum value of  $160 \pm 1^\circ$  due to the low-surface-energy netlike framework. However, when the molar ratio of Co/SA increased to 0.5, even though the roughness increased to  $1.84 \mu\text{m}$ , the water contact angle decreased to  $155 \pm 2^\circ$ . As depicted in Fig 4.1 (k), several large clusters emerged on the aluminum surface. Amazingly, the round pits disappeared. This phenomenon could be explained by the fact that the electrodeposition current density increased in the presence of the more conductive cobalt nitrate in the ethanolic solution. That is to say, when compared with a Co/SA molar ratio of 0.2, the quantity of products being generated increased and clustered together. As observed, the round pits have a larger number density than other areas on the surface in Fig 4.1 (i), these pits should be considered as prototypes which could grow into larger clusters when Co/SA molar ratios are increased from 0.2 to 0.5. Meanwhile, several micro-sized clusters were observed under high magnification (Fig 4.1 (l)). The netlike framework started to disband again but was still more compact than the case of a molar ratio of 0.08, which helps the surface retain its superhydrophobic

properties. Figures 4.1 (m) and (n) show the cleaned aluminum surfaces after modification solely with cobalt nitrate. Even though the roughness of this surface increased to 4.8  $\mu\text{m}$ , the contact angle of water decreased dramatically to around 10  $^\circ$ . Clearly, it can be seen on the left that the clusters became much larger while on the right the beautiful honeycomb-like framework disappeared. Based on these observed transitions, it is possible to deduce that the molar ratio of Co/SA in the solution has affected the morphology of the electrodeposited aluminum surface.

### 4.3.2 Surface composition

Figure 4.2 shows the EDS regional analysis of the aluminum substrate modified by electrodeposition in the mixed ethanolic solution with a Co/SA molar ratio of 0.5. The atomic percentage of each element for the superhydrophobic 0.5/Al sample is listed in Table 1. In the area 1 (Figure 4.2(a)), distinct peaks corresponding to cobalt, aluminum, carbon and oxygen were observed, and the atomic percentages were found to be 1.05, 14.81, 71.40 and 12.74% respectively. It can be deduced that the honeycomb-like framework found on aluminum substrates was composed of low-surface-energy cobalt stearate. This observation is also well supported by the XRD spectra (as given in Figure 4.3). In contrast, the content of cobalt, aluminum, carbon and oxygen of the white cluster in the area 2 was demonstrated to be completely different from area 1. As shown in Table 4.1 as well as Figure 4.2(b), the aluminum content decreased to 3.81%, while the content of cobalt and oxygen increased to 11.29% and 17.01% respectively. Plenty of cobalt atoms as well as an increased amount of

oxygen were found in the white cluster structure. Additionally, new products other than cobalt stearate may have formed on the aluminum substrate during the electrodeposition process. Further analysis by Fourier Transform Infrared spectroscopy (FTIR) confirmed the presence of cobalt oxide and hydroxide in the electrodeposited films. Apart from that, the carbon element originating from the methylated component was also present in this thin film.

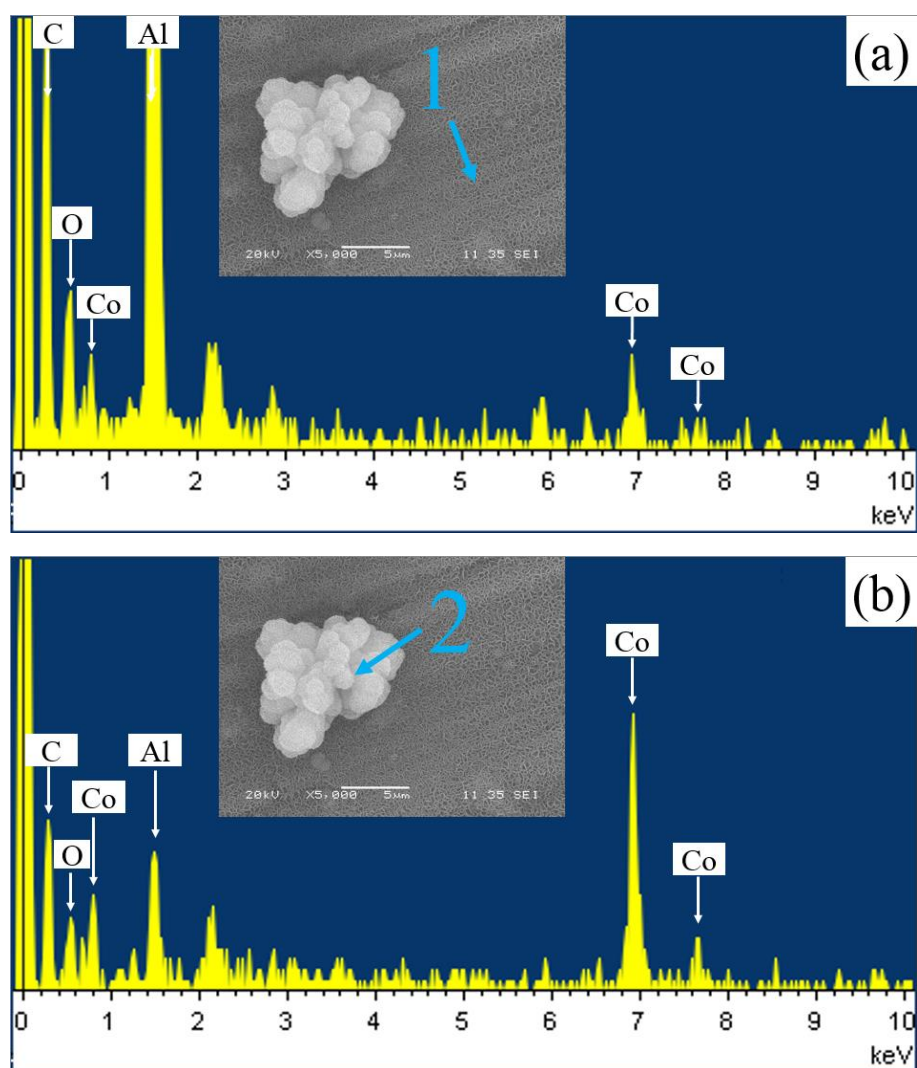


Figure 4. 2 EDS spectra of different areas on the aluminum substrate modified by electrodeposition in the mixed ethanolic solution with a Co/SA molar ratio of 0.5:

(a) area 1: the gray honeycomb-like framework, (b) area 2: the white clusters

Table 4. 1 The EDS results of atomic element percentages for different areas on the aluminum substrate modified by electrodeposition in the mixed ethanolic solution with a Co/SA molar ratio of 0.5

Element (At %)	Co	Al	C	O
<b>Area</b>				
<b>1</b>	1.05	14.81	71.40	12.74
<b>2</b>	11.29	3.81	67.89	17.01

Figure 4.3 (a) shows the low angle (3-30°) X-ray diffraction diagrams of chemically modified aluminum substrates by electrodeposition under a DC voltage of 10 V in (I) as-received aluminum, (II) Co/SA molar ratio (0.08) of mixture solution for 10min and (III) for 60min, respectively. The 0.08/Al sample prepared under 10 V for 10min (Figure 4.3(a-II)) didn't present much information on the cobalt stearate, which may be caused by an insufficient quantity of cobalt in the sample. However, when compared with as-received aluminum (Figure 4.3 (a-I)), a tiny peak near 5° as well as a broad peak at the 2θ range between 20 to 23° were still visible. To confirm the successful synthesis of cobalt stearate in the superhydrophobic film, a sample was prepared under the same Co/SA molar ratio (0.08) of mixture solution for 60 min. As obviously can be seen in Figure 4.3(a-III), the characteristic peak of cobalt stearate (200) was shown at  $2\theta = 21.76^\circ$ [19]. Another tiny peak at around  $2\theta = 5.4^\circ$  also confirmed the presence of cobalt stearate [20]. Additionally, the aluminum substrate drop-coated by cobalt stearate was also analyzed in the  $2\theta$  range of 3-30° by XRD as shown in Figure 4.3(a-

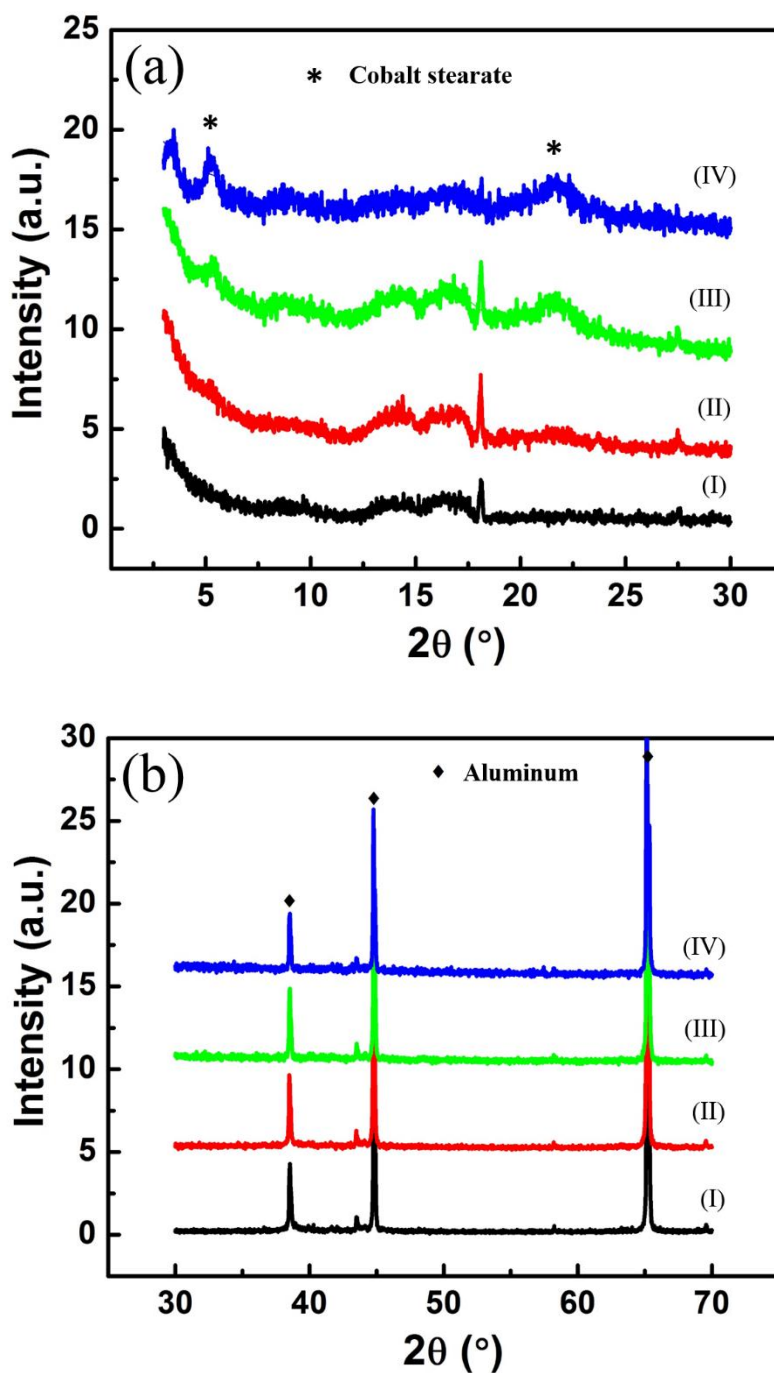


Figure 4. 3 (a) low angle XRD patterns of (I) As-received aluminum, (II) 0.08/AI for 10min, (III) 0.08/AI for 60min, and (IV) Cobalt stearate drop films on aluminum substrates; (b) shows the corresponding high angle XRD patterns of (a)

IV). The increased intensity of both the peaks mentioned above further confirmed the

generation of cobalt stearate during the electrodeposition process. In Figure 4.3(b), the corresponding high angle XRD patterns of Figure 4.3 (a) were illustrated. In the case of each sample, the distinct peaks present at  $38.47^\circ$ ,  $44.72^\circ$ , and  $65.1^\circ$  are ascribed to the characteristic peaks of Al (1 1 1), (2 0 0) and (2 2 0) due to the AA6061 aluminum alloy substrates [21].

Figure 4.4 (a) reveals the chemical composition of electrodeposited films formed in ethanolic solution with varied Co/SA molar ratios by FTIR spectra. There are four main infrared absorption zones clearly seen in these spectra. The first zone is shown as a broad absorption peak between  $3000$  and  $3600\text{ cm}^{-1}$ , which is assigned to  $\text{-OH}$  groups of cobalt hydroxide. Obviously, the peak intensity of  $\text{-OH}$  group is increasing gradually with enhanced Co/SA molar ratio. It means more and more cobalt hydroxide was formed on the electrodeposited films with the increasing amount of cobalt nitrate. In the second zone, two sharp absorption peaks at  $2850$  and  $2917\text{ cm}^{-1}$  are ascribed respectively to the asymmetric and symmetric C-H stretching modes of the  $\text{-CH}_2$  groups of cobalt stearate. In addition, a tiny peak due to the asymmetric in-plane C-H stretching mode of  $\text{-CH}_3$  groups from cobalt stearate also can be found at  $2954\text{ cm}^{-1}$  [22]. Based on the observation of the third zone, the carboxyl group  $\text{-COOH}$  from stearic acid appeared at  $1701\text{ cm}^{-1}$ , as shown in figure 4.4-a (III). However, this  $\text{-COOH}$  peak was no longer present in the case of the superhydrophobic surface, and two infrared absorption peaks which respectively appeared at  $1410$  and  $1550\text{ cm}^{-1}$  corresponding with the  $\text{-COOC}_o$  symmetric and asymmetric stretching vibrations were clearly observed [13, 19, 23]. Consequently, superhydrophobic cobalt stearate films

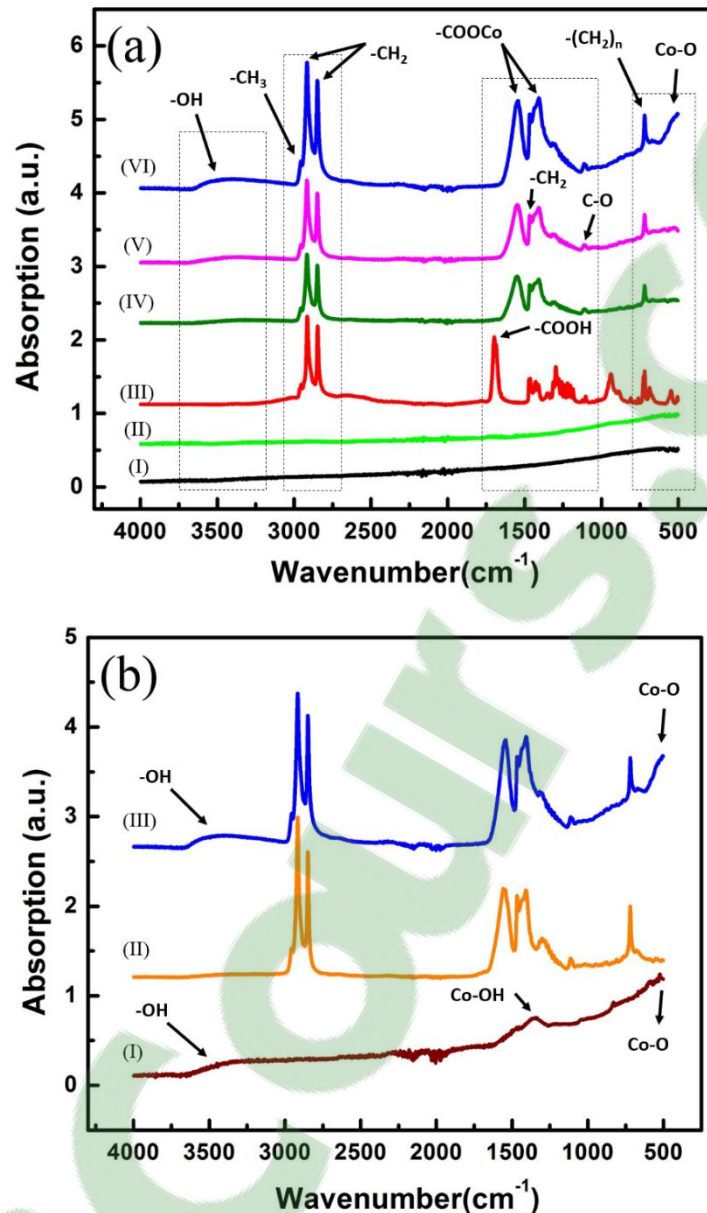


Figure 4. 4 (a) shows FTIR spectra of (I) as-received aluminum substrate and (III) solid stearic acid, as well as chemically modified aluminum substrates by electrodeposition in ethanolic solution with a Co/SA molar ratio of (II) 0, (IV) 0.08, (V) 0.2, (VI) 0.5; (b) compares the FTIR spectra of chemically modified aluminum substrates by electrodeposition in ethanolic solution with a Co/SA molar ratio of (I)  $\infty$ , (III) 0.5 and (II) aluminum substrates dropcoated with pure cobalt stearate were generated on the cathodic aluminum surface during the electrodeposition process.

Another nearby absorption peak was shown at  $1464\text{ cm}^{-1}$  due to  $-\text{CH}_2$  scissoring vibration [24]. The C-O stretching vibration of cobalt stearate was observed at  $1105\text{ cm}^{-1}$  [19]. In the last zone, we can observe a small, narrow peak at  $720\text{ cm}^{-1}$ , which is ascribed to the in-plane rocking vibration modes of  $-(\text{CH}_2)_n$  long carbon chains from cobalt stearate [19]. In addition, a broad, low frequency absorption peak is observed at the edge of the spectra around  $500\text{ cm}^{-1}$ , which corresponds with the Co-O stretching and Co-OH bending vibrations, indicating the presence of cobalt oxide and hydroxide [25-27].

Figure 4.4 (b) depicts the FTIR spectra of chemically modified aluminum substrates by electrodeposition in ethanolic solution with a Co/SA molar ratio of (I)  $\infty$ , namely with only cobalt nitrate solution, (II) aluminum substrates drop coated by pure cobalt stearate and (III) 0.5. The cobalt stearate was synthesized with diluted sodium hydroxide solution added into the mixture of cobalt nitrate and stearic acid ethanolic solution, following similar methods as reported by other researchers[19, 28]. In figure 4.4-b(I), the broad peak appearing between  $3000$  and  $3600\text{ cm}^{-1}$  corresponds to cobalt hydroxide, and cobalt oxide accounted for the low frequency absorption broad peak shown at the edge of the spectra around  $500\text{ cm}^{-1}$ . Additionally, the small peak present at  $1371\text{ cm}^{-1}$  was attributed to the Co-OH group[29]. Amazingly, 0.5/Al (figure 4.4-b(III)) exhibited not only all the characteristic absorption peaks of pure cobalt stearate (figure 4.4-b(II)), but also those of aluminum substrates by electrodeposition in only cobalt nitrate solution (figure 4.4-b(I)). In other words, the spectrum shown in figure 4.4-b (III) resulted from the overlapping of those shown in figure 4.4-b(II) and 4.4-b(I). Therefore,



the superhydrophobic aluminum substrates fabricated by electrodeposition in ethanolic solution with a Co/SA molar ratio of 0.5 contained complicated compositions consisting of cobalt stearate, cobalt oxide and hydroxide.

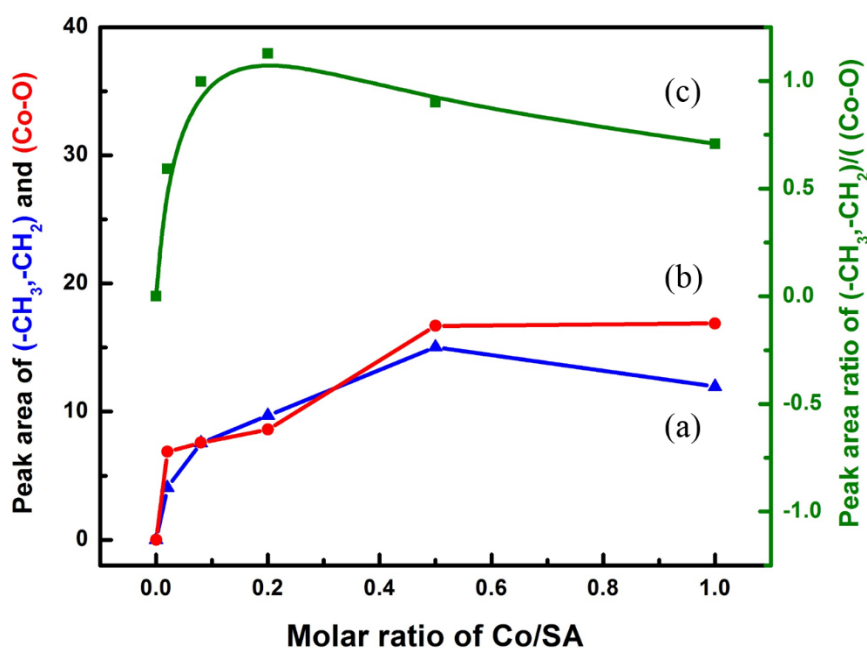


Figure 4. 5 The variation in the area under (a) the hydrocarbon (-CH<sub>2</sub> and -CH<sub>3</sub>) peaks, (b) the cobalt oxide (Co-O) peaks at the right end as a function of the molar ratio of Co/SA in the electrolytes; The curve (c) depicts the calculation results of (a)/(b) by peak area

Analysis on the integrated area under the hydrocarbon (-CH<sub>2</sub> and -CH<sub>3</sub>) peaks and the cobalt oxide (Co-O) peaks have been studied carefully based on all the FTIR spectra shown above (Figure 4.4). In Figure 4.5 (a), the hydrocarbon peak area of SA/Al (Co/SA=0) was nearly zero due to the fact that almost no current was observed during the electrodeposition process in pure stearic acid solution. With the additive of cobalt

nitrate, the hydrocarbon peak area keeps increasing until the Co/SA molar ratio reaches 0.5 which gives a maximum of 15.1, indicating more and more cobalt stearate was formed on the cathodic aluminum substrate. A slight decline was observed in the case of Co/SA molar ratio of 1.0. It could be explained by the deviation from the theoretical Co/SA molar ratio of 0.5, and a lack of stearic acid molecules. Figure 4.5 (b) shows the cobalt oxide (Co-O) peak area keeps increasing from zero to 22.5 with the gradually increasing Co/SA molar ratio in the electrolyte. In other words, more and more cobalt oxide was generated under the application of a DC voltage of 10V, which implies a second reaction, other than the formation of cobalt stearate, occurring on the cathodic aluminum surface. Furthermore, when the hydrocarbon peak area, representing hydrophobic cobalt stearate, is divided by the corresponding cobalt oxide peak area, which represents hydrophilic cobalt oxide or hydroxide, the resulting ratio depicts the competition between low and high surface energy composition on the electrodeposited films. It should be mentioned that a new analysis method is employed in order to realize a comprehensive understanding of these superhydrophobic films. The results are shown in Figure 4.5 (c). Interestingly, the curve reaches its highest point at the Co/SA molar ratio of 0.2, which is in good consistence with the fact that the greatest contact angle of  $161^\circ$  is characterized on the wettability of aluminum substrate modified in the ethanolic solution with a Co/SA molar ratio of 0.2.

### 4.3.3 Surface wettability

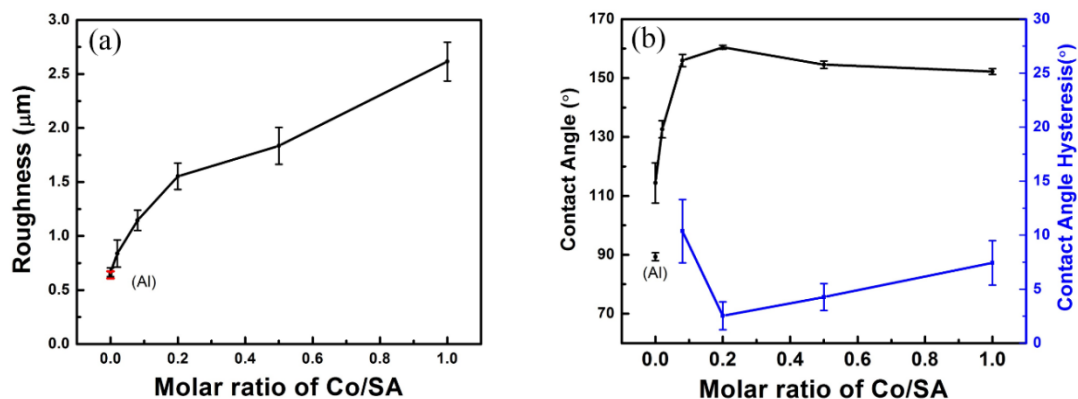


Figure 4. 6 (a) Surface roughness (b) and water contact angle as well as contact angle hysteresis of as-received aluminum substrate and electrochemically modified cathodic aluminum substrates with the application of 10V DC voltage for 10 min in varied molar ratios of Co/SA ethanolic solution

In order to study the surface wettability of modified cathodic aluminum substrates by electrodeposition in varied molar ratios of Co/SA ethanolic solution, water contact angle as well as roughness measurements were carefully carried out on these surfaces. The results are shown in Figure 4.6 (a) and (b). The as-received aluminum substrate exhibited a small surface roughness value of  $0.64 \pm 0.03 \mu\text{m}$  and a water contact angle of  $89 \pm 2^\circ$ . The aluminum substrate modified by stearic acid under 10 V DC voltage for 10min showed hardly any change in surface roughness, while the contact angle increased up to  $114 \pm 7^\circ$  due to the passivation of low-surface-energy stearic acid with long alkyl chains. The surface roughness and contact angle of aluminum substrate modified in Co/SA with a molar ratio of 0.02 were found to be  $0.84 \pm 0.13 \mu\text{m}$  and  $133 \pm 3^\circ$  respectively. With increasing the Co/SA molar ratio up to 0.08, a superhydrophobic

cathodic aluminum substrate showing a contact angle of  $156 \pm 2^\circ$  was successfully fabricated, for which the surface roughness was observed to be  $1.15 \pm 0.09 \mu\text{m}$ . It can be explained by the formation of honeycomb-like cobalt stearate films on the top layer of the aluminum surface, as evidenced by XRD, FTIR and SEM. With the further increase of the Co/SA molar ratio to 0.2, the superhydrophobic surface demonstrated a maximum contact angle of  $161 \pm 1^\circ$  and the corresponding surface roughness was  $1.55 \pm 0.12 \mu\text{m}$ . However, even though the roughness increased to  $1.84 \pm 0.17 \mu\text{m}$ , when the molar ratio of Co/SA was increased to 0.5, the water contact angle of the modified aluminum surface dropped to  $155 \pm 2^\circ$ . This effect was caused by the formation of large clusters composed of hydrophilic cobalt oxide and hydroxide, as clearly observed in the SEM images (figure 4.1(k)). As nature teaches us, a superhydrophobic surface emphasizes the importance of a combination of micro-nano roughness on the surface and low surface energy. The roughness and water contact angle of aluminum substrates modified in Co/SA molar ratio of 1.0 was  $2.62 \pm 0.18 \mu\text{m}$  and  $152 \pm 1^\circ$ , respectively. A comparative experiment was also carried out by electrodeposition of aluminum substrate in a pure cobalt nitrate ethanolic solution. The hydrophilic surface, with an elevated surface roughness of  $4.82 \pm 0.45 \mu\text{m}$ , demonstrated a water contact angle around  $10^\circ$ . Figure 4.6 (b) compares the contact angle hysteresis (blue curves) of the water drop on the samples as discussed above. The difference between advancing and receding contact angles during a relative movement of the droplet was defined as contact angle hysteresis (CAH)[30]. The CAH of aluminum substrate modified in the Co/SA molar ratio of 0.08 was found to be  $10 \pm 3^\circ$ , which then dropped dramatically to

the minimum  $3 \pm 1^\circ$  with the increase of Co/SA molar ratio to 0.2. Further increasing the Co/SA molar ratio did not reduce the contact angle hysteresis. On the contrary, there is a tendency for the CAH to slowly increase as the molar ratio of Co/SA increases. The CAH of our samples increased from  $4 \pm 1^\circ$  to  $7 \pm 2^\circ$  when the molar ratio of Co/SA increased from 0.5 to 1.0. In general, solid surfaces with lower contact angle hysteresis exhibit superior roll-off properties. Therefore, electrochemically modified cathodic aluminum substrates in Co/SA molar ratio of 0.2 ethanolic solution showed the best non-wettability properties.

In the literature, water contact angle on stearic acid impregnated with cellulose surface is  $80 \pm 1^\circ$  [31]. And water contact angle on stearic acid passivated flat ZnO films with a roughness value of 2nm was reported as  $73.5 \pm 4^\circ$  [32]. Similarly, lauric acid (LA) passivated smooth cobalt oxide surface was found to be  $75.2 \pm 6.6^\circ$  [33]. Presumably, the water contact angle on the smooth cobalt stearate surface is around  $75^\circ$ . Two basic models, namely Wenzel model and Cassie–Baxter model, are normally used to explain the contact angle behavior of water on a rough surface. The Wenzel equation is written as

$$\cos\theta_w = r \cos\theta_1 \quad (4.5)$$

where  $\theta_w$  and  $\theta_1$  are the contact angle of water drop on a rough and smooth surface respectively, having the same surface composition; and roughness factor ‘r’ is defined as the ratio of the true (on rough surfaces) and apparent (smooth) surface areas and therefore is always a positive number and ‘r’ > 1.

In the Wenzel model, (i) when the true water contact angle  $\theta_1$  on a smooth surface is less than  $90^\circ$ , the apparent contact angle  $\theta_w$  will be less than the true contact angle  $\theta_1$  on a rough surface, and (ii) when the true contact angle  $\theta_1$  is larger than  $90^\circ$ , the apparent contact angle  $\theta_w$  will be greater than the true contact angle  $\theta_1$  on a rough surface. In our case, the water contact angle on the smooth cobalt stearate surface is around  $75^\circ$  and less than  $90^\circ$ , indicating a contact angle even smaller than  $75^\circ$  to be observed on the rough surface according to Wenzel model. Obviously, it is contradicted with the fact that a superhydrophobic surface with a water contact angle as large as  $156^\circ$  was observed on the honeycomb-like rough surface on aluminum substrate. Therefore, the Wenzel model cannot explained the achievement of our electrodeposited superhydrophobic film here.

However, the wettability state of our cobalt stearate superhydrophobic surface would be possible to explain considering the Cassie–Baxter model, where contact angle of water is determined by the contact angles of the composite structure of solid cobalt stearate films and the trapped air in the framework structure. The Cassie–Baxter equation is written as:

$$\cos\theta_c = f_1(\cos\theta_1 + 1) - 1 \quad (4.6)$$

where  $\theta_c$  and  $\theta_1$  are the contact angle of water drop on a rough and smooth surface respectively,  $f_1$  is the fraction of solid surface in contact with water drop. As  $\theta_1$  is presumably as  $75^\circ$  and the surperhydrophobic surface exhibits a water contact

angle of  $156^\circ$ , the calculated  $f_1$  value is 6.87%. Similarly, A. Siddaramanna *et al.* reported the fraction of solid surfaces varied between 2% and 9% when the superhydrophobic stearic acid functionalized ZnO surfaces were fabricated in varied  $[SA]/[Zn^{2+}]$  molar ratio by one step chemical bath deposition [22]. It is generally believed that the surface free energy and surface roughness are the two main factors governing the surface wettability. The honeycomb-like cobalt stearate framework structure endows certain roughness as well as hydrophobicity on aluminum substrates. Therefore, the water drop does not fill the grooves on this rough surface and thereby the air fraction was increased.

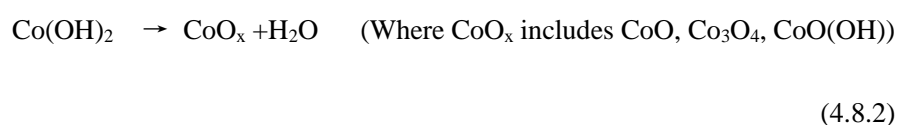
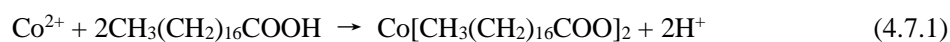
Moreover, according to the studies we have done before, the necessary roughness for fabricating superhydrophobic surfaces is dominated by the composition of the coatings. It was reported that the roughness of superhydrophobic surfaces incorporating fluoroalkylsilane (FAS) molecular was less than  $1\ \mu\text{m}$  [7, 34], while the superhydrophobic metallic stearate surface exhibited a surface roughness between 2 to  $6\ \mu\text{m}$  [4, 17, 35, 36]. It can be explained by the fact that FAS molecular composed of  $-\text{CF}_3$  has a lower surface energy than that of stearic acid composed of  $-\text{CH}_3$  in the aspect of chemical nature properties.

#### **4.3.4. Mechanism**

##### **(1). Two simultaneous reactions**

According to the FTIR analysis above, several different products were found generated on the electrodeposited films including cobalt stearate, cobalt oxide and

hydroxide. There exists two simultaneous reactions on the cathode when a 10 V DC voltage is applied to the bath solution. Here are the reactions happened on the cathode:



For the primary reaction, as shown in the equation (1), when the DC voltage is applied to the electrodes, the  $\text{Co}^{2+}$  ions near the cathode react with stearic acid to form cobalt nitrate and hydrogen ions. Meanwhile, the concentration of free hydrogen ions in the solution increases, and some of them obtain electrons to form  $\text{H}_2$ . The gradual release of  $\text{H}_2$  promotes the formation of a micro/nano structure on the cathodic aluminum surface, as we have observed with the honeycomb-like topography in the SEM images. Moreover, similar reactions have been utilized to explain the formation of cerium myristate[14] and manganese myristate[13].

For the secondary reaction in our case, as shown in the equation (2), we proposed that the formation of cobalt oxide and hydroxide could be ascribed to the reaction between  $\text{Co}^{2+}$  with  $\text{H}_2\text{O}$  under the application of an electrical field since there is 5% water in the purchased ethanol solution.  $\text{H}_2\text{O}$  instead of  $\text{EtOH}$  is engaged in this reaction



due to the superiority of H<sub>2</sub>O to EtOH, with respect to its ability to break down into free ions. It is well known that ethanol is classified as a non-electrolyte which cannot break down into free ions to conduct electricity. With the prolonged reaction time, presumably, the accumulated cobalt hydroxide on the cathodic aluminum substrates would take dehydration and oxidation reactions to form small amounts of cobalt oxide with complicated compositions including CoO, Co<sub>3</sub>O<sub>4</sub>, CoO(OH), as evidenced by FTIR spectra. Though, recently cobalt oxide was mostly reported as synthesis involving a calcination process[25, 37]. Additionally, it was found during the experiment that the black particles detached from the cathodic aluminum substrate, which were deduced to be cobalt oxide, were dragged rapidly to the magnetic stirring bar at the bottom of the beaker (see a video attached in supplemental information). Cobalt oxide is famous as a magnetic material[37], and this interesting phenomenon also confirmed the presence of magnetic cobalt oxide.

## 6.2 Discussion on the optimized Co/SA ratio

Both of the reactions proposed above occurred simultaneously in the mixed ethanolic solution of cobalt nitrate and stearic acid, in our cases of electrodeposition at 10V DC voltages for 10min, but the percent yield of cobalt stearate varied with different molar ratios of Co/SA. In other words, there exists a relative competition between these two simultaneous reactions. Generally, the higher concentration of reactants indicates the higher reacting rate from the perspective of kinetic studies. In the same environment, the rate of reactions (1) was controlled by the concentration of Co<sup>2+</sup> as well as stearic acid. However, the rate of reactions (2) was only governed by

the concentration of  $\text{Co}^{2+}$  ions. According to the formula of cobalt stearate,  $\text{Co}(\text{SA})_2$ , the theoretical amount of stearic acid is defined as two times of that of cobalt nitrate during the electrodeposition process. When the Co/SA molar ratio of the mixed solution was small (e.g. less than 0.2) and composed of few  $\text{Co}^{2+}$  with plenty of SA, the rates of each reaction were low. With stearic acid providing much more than the theoretical amount, most of the  $\text{Co}^{2+}$  ions would follow the reaction (1) to generate more cobalt stearate. On the contrary, the increase of the Co/SA molar ratio gave few SA particles with plenty of  $\text{Co}^{2+}$  ions, and the rate of reaction (2) would increase while reaction (1) would slow down due to the lack of stearic acid. In this case, the percentages of cobalt oxide and hydroxide in the electrodeposited films would also increase. The analyses above were in good agreement with the results of peak area analysis obtained from the FTIR spectra. Therefore, it should be mentioned that the molar ratio of Co/SA in the electrolyte affected the composition of electrodeposited film on the aluminum surface.

Actually, the “metallic ions/organic acid” molar ratio of 0.5 is not the best choice to synthesize an excellent low-surface-energy superhydrophobic surface due to the fact that the secondary reaction, in most case, is inevitable with the application of electric field. For example, in a study of Xu et al[38], chemically cleaned aluminum substrates were modified by electrodeposition in an ethanolic copper nitrate( $\text{Cu}(\text{NO}_3)_2$ ) and stearic acid with a varied Cu/SA molar ratio. Plenty of CuO with high-surface-energy was formed on the aluminum surface when electrodeposited in the case of 0.5 Cu/SA molar ratio, as evidenced by their EDS, XRD studies. This observation is in good agreement with our case. It further confirmed that the theoretical molar ratio of 0.5 is not the best

choice. Additionally, Liu *et al.* [14] fabricated a superhydrophobic cerium myristate film on magnesium plate in an ethanolic solution containing 0.05 M cerium nitrate ( $\text{Ce}(\text{NO}_3)_3$ ) hexahydrate and 0.2 M myristic acid, which equates to a Ce/MA molar ratio of 0.25 instead of the theoretical value 0.33. Similarly, Zhang *et al.* [39] also reported a superhydrophobic cerium myristate film formed on aluminum substrates by electrodeposition in a Ce/MA molar ratio of 0.25. All the observations above prove that the most appropriate “metallic ions/organic acid” molar ratio for the electrodeposition process is lower than the theoretical value. However, an optimized surface topography and low surface energy are generally the two important requirements for the fabrication of superhydrophobic surfaces [35, 40]. When the Co/SA molar ratio becomes extremely small, the amount of cobalt stearate is so low that it is impossible to provide enough roughness for the creation of an excellent superhydrophobic surface, as has been proved by the case of 0.02/Al and 0.08/Al. Therefore, in our cases, the aluminum substrates electrochemically modified in the mixed ethanolic solution with a Co/SA molar ratio of 0.2 instead of 0.08 or 0.5 demonstrated the best roll-off properties.

### **4.3.5 Corrosion resistance properties**

#### **(1). Potentiodynamic polarization study**

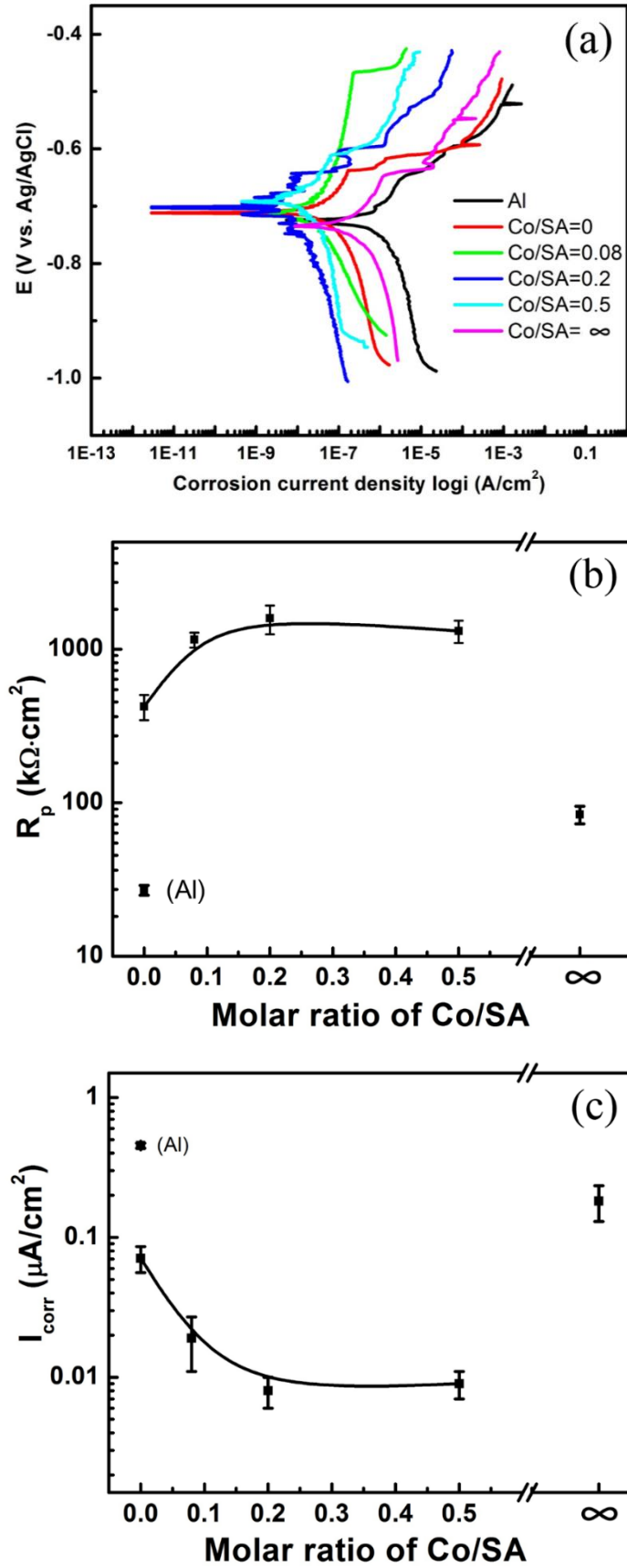


Figure 4. 7 (a) Potentiodynamic polarization curves; (b) Polarization resistance; (c)

Corrosion current density of as-received aluminum, and thin films prepared from a cobalt nitrite and stearic acid mixed solution with Co/SA molar ratios of 0.08, 0.2, 0.5 as well as electrodeposited films in a pure solution of stearic acid (i.e. Co/SA=0) and cobalt nitrite (i.e. Co/SA= $\infty$ ), respectively

To compare the corrosion resistance properties of the electrodeposited thin films on aluminum in a cobalt nitrite and stearic acid mixed solution with varied Co/SA molar ratios, potentiodynamic polarization tests have been carefully carried out after immersion of the thin films for 24h in a 3.5 w.t. % NaCl aqueous solution. Figure 4.7 (a) shows potentiodynamic polarization curves of as-received aluminum, and thin films prepared from a cobalt nitrite and stearic acid mixed solution with Co/SA molar ratios of 0.08, 0.2, 0.5 as well as electrodeposited films in a pure solution of stearic acid and cobalt nitrite, respectively. The corrosion potential ( $E_{\text{corr}}$ ), corrosion current density ( $I_{\text{corr}}$ ) and polarization resistance ( $R_p$ ) were three most pertinent and discussed parameters in polarization curves, which are presented in Table 4.2 as well as Figure 4.7 (b) and (c).  $E_{\text{corr}}$  and  $I_{\text{corr}}$  were calculated from the intersection points by extrapolating the anodic and cathodic curves. The polarization resistance ( $R_p$ ) was determined by Stern-Geary equation (eq. 1) shown below:

$$R_p = \frac{\beta_a \beta_c}{2.3 I_{\text{corr}} (\beta_a + \beta_c)} \quad (4.9)$$

where  $\beta_a$  and  $\beta_c$  are the anodic and cathodic Tafel slopes, respectively.

Table 4. 2 The open circuit potential (OCP), corrosion potential ( $E_{\text{corr}}$ ), current density ( $I_{\text{corr}}$ ) and polarization resistance ( $R_p$ ) for aluminum substrates electrodeposited in the solution of varied molar ratio of Co/SA

	Al	SA/Al	0.08/Al	0.2/Al	0.5/Al	$\infty$ /Al
<b><math>E_{\text{corr}}</math></b> <b>(mV)</b>	$-724 \pm 7$	$-699 \pm 6$	$-731 \pm 17$	$-706 \pm 8$	$-695 \pm 19$	$-756 \pm 12$
<b>OCP</b> <b>(mV)</b>	$-724 \pm 8$	$-707 \pm 10$	$-714 \pm 15$	$-709 \pm 6$	$-690 \pm 22$	$-734 \pm 17$
<b><math>R_{p1}</math></b> <b><math>k\Omega \cdot \text{cm}^2</math></b>	26	406	1057	1820	1276	86
<b><math>R_{p2}</math></b> <b><math>k\Omega \cdot \text{cm}^2</math></b>	$27 \pm 2$	$424 \pm 79$	$1153 \pm 129$	$159 \pm 340$	$1317 \pm 218$	$84 \pm 11$
<b><math>I_{\text{corr}}</math></b> <b>(<math>\mu\text{A}/\text{cm}^2</math>)</b>	$0.453 \pm 0.019$	$0.071 \pm 0.015$	$0.019 \pm 0.008$	$0.008 \pm 0.002$	$0.009 \pm 0.002$	$0.182 \pm 0.052$

The as-received aluminum exhibited a corrosion current density ( $I_{\text{corr}}$ ) of  $0.453 \pm 0.019 \mu\text{A}/\text{cm}^2$  and a polarization resistance ( $R_p$ ) of  $27 \pm 2 k\Omega \cdot \text{cm}^2$ , while the  $I_{\text{corr}}$  and  $R_p$  of SA/Al were found to be only  $0.071 \pm 0.015 \mu\text{A}/\text{cm}^2$  and  $424 \pm 79 k\Omega \cdot \text{cm}^2$  respectively. It has been proved that larger polarization resistance and a lower corrosion current density indicate superior anti-corrosion properties of the SA/Al sample. Compared with as-received aluminum, SA/Al substrates showed improved corrosion resistance properties, which resulted from a very thin film of stearic acid passivated on the partial

aluminum surface. The Co/Al sample also showed a  $I_{\text{corr}}$  value of  $182.5 \pm 52 \text{ nA/cm}^2$  as well as a  $R_p$  value of  $84 \pm 11 \text{ k}\Omega \cdot \text{cm}^2$ . This is due to the thick cobalt oxide and hydroxide clusters as evidenced by FTIR. This oxide/hydroxide thin film formation on top of the aluminum substrate has been reported as an effective, high-capacitance material[41, 42], which restricts the electron transfer between the electrolyte and aluminum substrate.

It was observed that the superhydrophobic films fabricated in a Co/SA molar ratio of 0.08 exhibited an even smaller  $I_{\text{corr}}$  of  $0.019 \pm 0.008 \text{ }\mu\text{A/cm}^2$  along with a larger polarization resistance of  $1153 \pm 129 \text{ k}\Omega \cdot \text{cm}^2$ . This can be explained by the formation of leaf-like cobalt stearate on the bare aluminum surface. With a further increase in the molar ratio of Co/SA to 0.2, the  $I_{\text{corr}}$  value of the superhydrophobic film decreased to a minimum of  $0.008 \pm 0.002 \text{ }\mu\text{A/cm}^2$ , and the  $R_p$  value increased to a maximum of  $1591 \pm 340 \text{ k}\Omega \cdot \text{cm}^2$ , which demonstrates excellent protection against corrosion. When compared with as-received aluminum, the corrosion current density of superhydrophobic thin films electrodeposited on aluminum substrates using the solution with a Co/SA molar ratio of 0.2 were sharply reduced by about two orders of magnitude. This reduced current density was attributed to trapped air on the highly-porous and homogeneous cobalt stearate films, acting as a capacitor, which prevented the penetration of chemical ions (e.g.  $\text{Na}^+$  and  $\text{Cl}^-$ ) thus inhibiting the electron transfer between the corrosive medium and aluminum substrate. Meanwhile, a restricted supply of oxygen contributed to the current reduction as well. On the other hand, the enhanced polarization resistance was due to the presence of low-surface-energy cobalt stearate,

fabricating a very compact network on the aluminum substrate, as evidenced by the SEM images as well as the increased FTIR peak intensities of  $-\text{CH}_3$ ,  $-\text{CH}_2$  and  $-\text{COOCo}$  from the cobalt stearate. When the molar ratio of Co/SA further increased from 0.2 to 0.5, the  $I_{\text{corr}}$  value was found to be  $0.009 \pm 0.002 \mu\text{A}/\text{cm}^2$  showing tiny increases while  $R_p$  values slightly decreased to  $1317 \pm 218 \text{ k}\Omega \cdot \text{cm}^2$ . As observed in the SEM images shown in Figure 4.1, the honeycomb-like cobalt stearate film of the latter was less compact than the former, indicating an inferior anti-corrosion property. However, as evidenced by FTIR, an increase of cobalt oxide and hydroxide particles, was observed on top of the cobalt stearate film and thus maintained the excellent corrosion resistance property which has been reported as an important factor for effective high-capacitance materials[26, 41]. Chen *et al.*[18] reported a Co-based superhydrophobic powder film composed of Co and cobalt myristate crystals by one-step electrodeposition under 30 V in a mixture of cobalt chloride and myristic acid solution. However, they didn't study the corrosion resistance properties of Co-based superhydrophobic films. In the study conducted by Xu *et al.*, superhydrophobic copper stearate and copper oxide thin films were fabricated on aluminum substrate in an ethanolic solution containing stearic acid and copper nitrite via a one-step electrochemical modification process. The copper stearate superhydrophobic film prepared from a copper nitrite and stearic acid mixed solution with a Cu/SA molar ratio of 0.5 exhibited a current density as low as  $0.011 \mu\text{A}/\text{cm}^2$  and polarization resistance of  $1328 \text{ k}\Omega \cdot \text{cm}^2$  in 3.0 wt.% NaCl aqueous solution[38]. This result is quite comparable with our results. In our case, the cobalt stearate-based superhydrophobic surface, in 3.5 wt.% NaCl aqueous solution,



demonstrated a lower  $I_{\text{corr}}$  value of  $0.008 \mu\text{A}/\text{cm}^2$  and larger  $R_p$  value of  $1591 \text{ k}\Omega \cdot \text{cm}^2$ . Obviously, the cobalt stearate-based superhydrophobic aluminum substrate exhibited a superior anti-corrosion property in a more corrosive environment.

In the present work, to obtain the exact polarization resistance, a novel method was utilized to calculate  $R_p$  by Ohm's law, namely the reciprocal of the slope of linear current-potential (I-E) curves as shown below:

$$R_p = \frac{\Delta E}{\Delta I} \quad (4.10)$$

where I and E are the current and potential ( $\pm 15 \text{ mV}$  variation around the corresponding  $E_{\text{corr}}$ ), respectively.

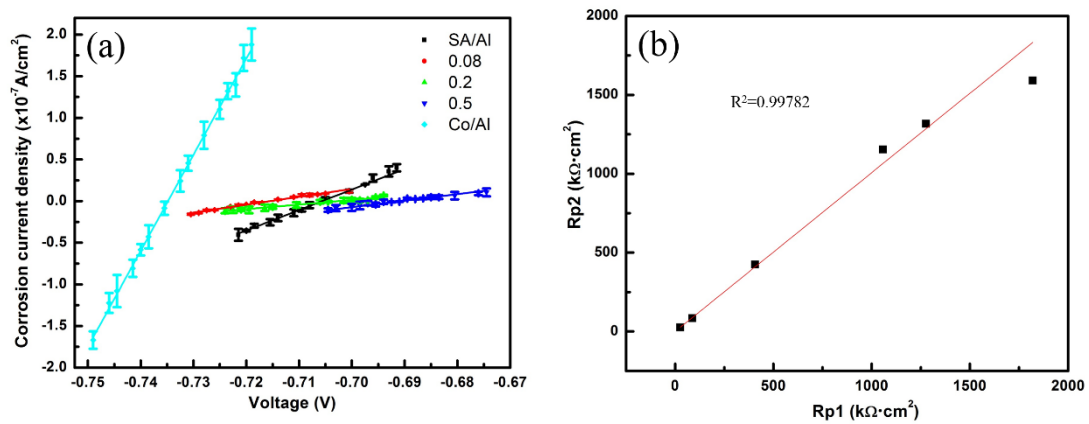


Figure 4. 8 (a) The current-potential (I-E) curves obtained from the potential variation of  $\pm 15 \text{ mV}$  around the corresponding corrosion potential ( $E_{\text{corr}}$ ) for the  $R_p$  calculated by ohm's law; (b) the  $R_p$  value calculated by ohm's law ( $R_{p1}$ ) versus by Stern-Geary equation ( $R_{p2}$ )

Figure 4.8 (a) shows the linear I-E function of SA/Al, Co/Al as well as superhydrophobic aluminum substrates electrodeposited in varied Co/SA molar ratio of 0.08, 0.2 and 0.5. The as-received aluminum, with a  $R_p$  value of  $26 \text{ k}\Omega \cdot \text{cm}^2$ , was not included in this plot due to the fact that the I-E slope was so high that it was not comparable to the other substrates (see the supplementary document). As mentioned above, the reciprocal of the I-E curves represents the value of  $R_p$ . That is to say, the larger the slope is, the smaller polarization resistance it has. Obviously, Co/Al exhibited the largest I-E slope, followed by SA/Al, in sequence of 0.08/Al, 0.5/Al and 0.2/Al. These Ohm's law  $R_p$  values were respectively,  $86 \text{ k}\Omega \cdot \text{cm}^2$ ,  $406 \text{ k}\Omega \cdot \text{cm}^2$ ,  $1057 \text{ k}\Omega \cdot \text{cm}^2$ ,  $1276 \text{ k}\Omega \cdot \text{cm}^2$  and  $1820 \text{ k}\Omega \cdot \text{cm}^2$ . Figure 4.8 (b) depicts the polarization resistance obtained from Ohm's law ( $R_{p1}$ ) versus from the Stern-Geary equation ( $R_{p2}$ ). The slope of the fit was about 1, demonstrating an acceptable correlation between those two different methods. The  $R_{p1}$  and  $R_{p2}$  values mentioned above have been shown in Table 4.2.

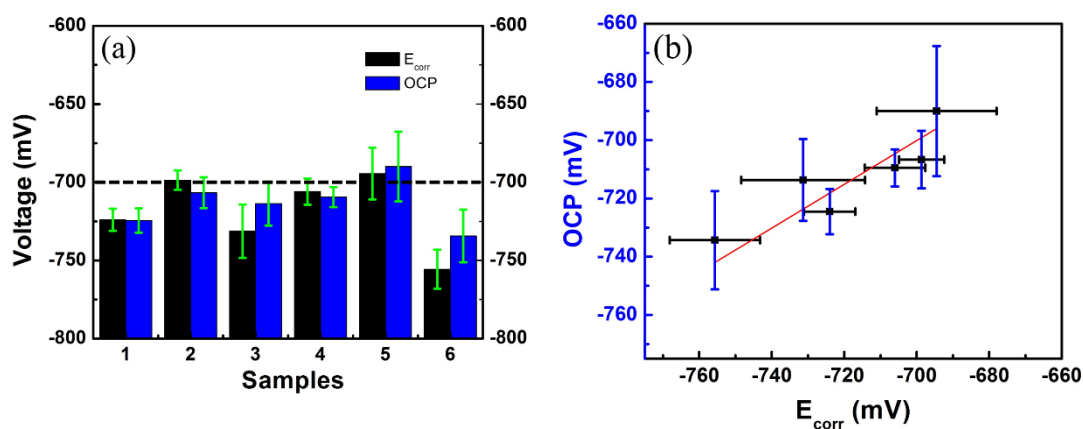


Figure 4. 9 (a) The corrosion potentials ( $E_{corr}$ , black) and open circuit potentials

(OCP, blue) for thin films samples Potentiodynamic polarization curves of (1) as-received aluminum, and thin films prepared from a cobalt nitrite and stearic acid mixed solution with Co/SA molar ratios of (3) 0.08, (4) 0.2, (5) 0.5 as well as electrodeposited films in a pure solution of (2) stearic acid and (6) cobalt nitrite, respectively. A horizontal dotted line has been plotted at -700 mV to guide the eyes.

(b)  $E_{\text{corr}}$  obtained from Stern-Geary equation versus OCP stabilized in 3.5 w.t.% sodium chloride solution for 24h

Figure 4.9 (a) depicts the comparison between corrosion potentials ( $E_{\text{corr}}$ , black) and open circuit potentials (OCP, blue) of as received aluminum and aluminum substrates electrodeposited in varied molar ratio of Co/SA in the solution under a direct voltage(DC) of 10 V for 10 min. The  $E_{\text{corr}}$  value of as-received aluminum as  $-724 \pm 7$  mV is nearly equivalent to the OCP value of  $-724 \pm 8$  mV, fitting the theoretical situation very well. This phenomenon was also observed by Pyun *et al*[43]. As for SA/Al and 0.2/Al, the  $E_{\text{corr}}$  value exhibited a slightly more negative potential than the OCP values of 8 mV and 3 mV, respectively. However, in most situations, OCP demonstrated more positive values than  $E_{\text{corr}}$  of 17 mV, 5 mV and 22 mV respectively for 0.08/Al, 0.5/Al and Co/Al. This observation was in good agreement with the study by Morks *et al*. [44]. In their case, the corrosion behavior of plasma sprayed alumina films on mild steel was investigated by means of open circuit potential as well as polarization curves. A comparison between the OCP and  $E_{\text{corr}}$  values of mild steel and coated alumina steels demonstrated that  $E_{\text{corr}}$  was always more negative than OCP. This is to mention that no

significant correlation in the  $E_{\text{corr}}$  (or OCP) is noticed due to the variation of the composition of the electrodeposited thin films on aluminum. A linear plot has been established with OCP values obtained from the stabilized surface exposed to a sodium chloride solution for 24 h versus  $E_{\text{corr}}$  obtained from Stern-Geary equation, as shown in Figure 4.9 (b).

## (2). Electrochemical impedance spectroscopy (EIS)

As a complementary electrochemical technique, electrochemical impedance spectroscopy (EIS) was also employed to evaluate the corrosion resistance properties of samples presented in the Figure 4.7 Tafel curves. The EIS studies of two samples were demonstrated, as-received aluminum and the superhydrophobic surface with the highest polarization resistance prepared with Co/SA molar ratio of 0.2 in the solution. EIS experiments were carried out after immersing the Al substrates and the superhydrophobic thin films in the 3.5 w.t. % NaCl solution for approximately 20 h. Figure 4.10 presents the Nyquist and Bode plots of as-received aluminum and superhydrophobic thin films on Al substrate based on the fitted results analyzed by ZView 2 program (see the supporting information for both original and fitted EIS plots). The corresponding electrical equivalent circuits were also plotted for a better understanding of the corrosion behavior, as shown in Figure 4.10 (d).

Figure 4.10 (a) shows the Nyquist plots, which depict the imaginary component ( $Z_{\text{imaginary}}$  or  $Z''$ ) as a function of the real component ( $Z_{\text{real}}$  or  $Z'$ ). The Nyquist plot of as-received aluminum, composed of a small semi-circle of diameter:  $8.42 \text{ k}\Omega \cdot \text{cm}^2$ , was

totally covered by that of superhydrophobic thin films on Al substrate with a large semi-circle of diameter:  $8820 \text{ k}\Omega\cdot\text{cm}^2$ , which is three orders of magnitude larger than the former. The inset image in Figure 4.10 (a) depicts the entire region of as-received aluminum as well as the high frequency region of superhydrophobic thin films on Al substrate. Interestingly, a small semi-circle was visible for superhydrophobic thin films after enlargement, which is corresponding to the  $\text{CPE}_f$  and  $R_f$  elements in the electrical equivalent circuit.

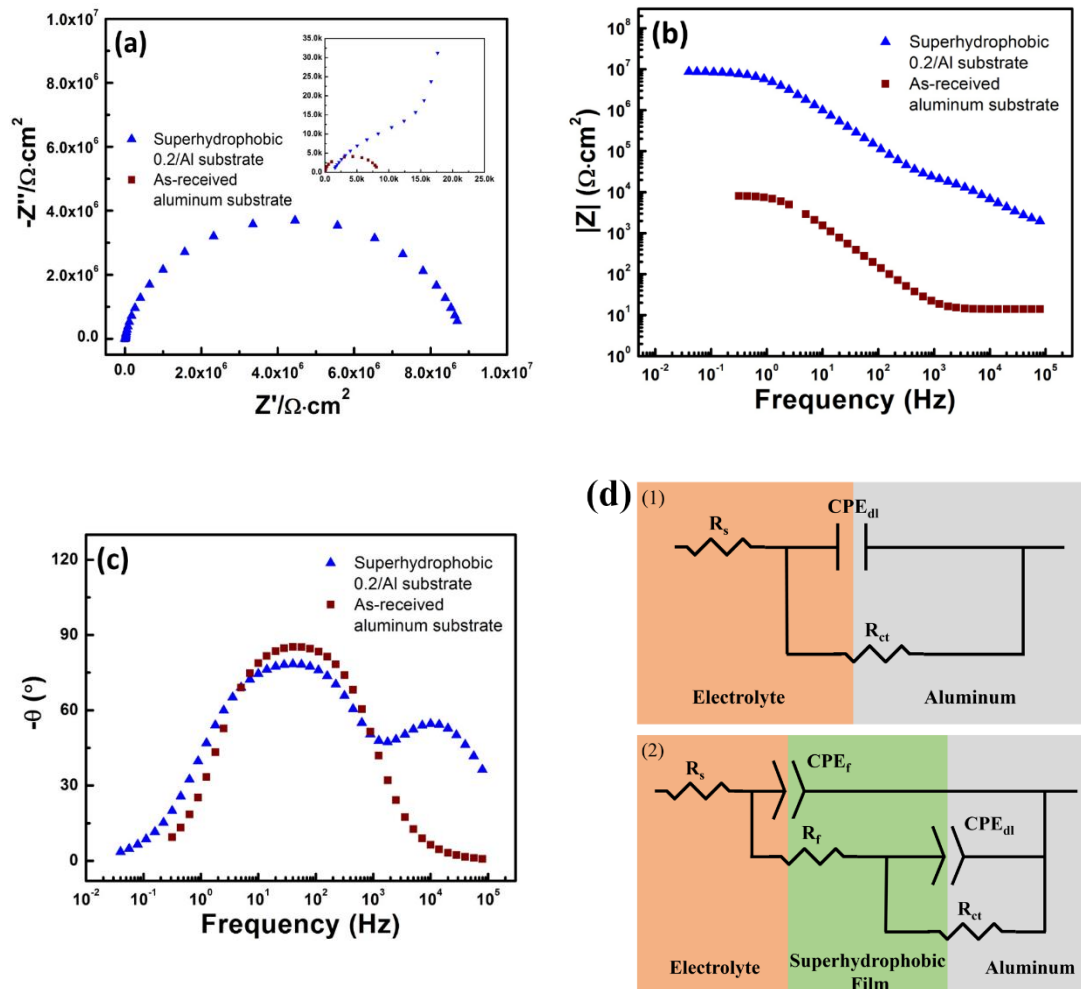


Figure 4. 10 (a)Nyquist plots (b) Bode modulus diagrams and (c) Bode phase angle

diagrams of superhydrophobic thin films electrodeposited on Al from Co/SA molar ratio of 0.2 and as-received aluminum substrate. (d) Electrical equivalent circuits employed to simulate the EIS study of (d1) as-received aluminum and (d2) superhydrophobic thin films electrodeposited on Al from Co/SA molar ratio of 0.2.

The inset image shows the amplified diagram in the higher frequency range

Table 4. 3 Electrochemical parameters obtained from electrical equivalent circuits (EEC), fitted EIS data of as-received aluminum and superhydrophobic thin films on

Al substrates in 3.5 w.t. % NaCl solution

Samples	$R_s$	$CPE_f$		$R_f$	$CPE_{dl}$		$R_{ct}$
	( $\Omega \text{ cm}^2$ )	$Y_f$	$n_f$	( $\Omega \text{ cm}^2$ )	$Y_{dl}$	$n_{dl}$	( $\Omega \text{ cm}^2$ )
		( $\Omega^{-1} \text{ s}^n \text{ cm}^{-2}$ )			( $\Omega^{-1} \text{ s}^n \text{ cm}^{-2}$ )		
<b>As-received aluminum</b>	14.13	\	\	\	$1.08 \times 10^{-5}$	1	$8.42 \times 10^3$
<b>Superhydro- phobic 0.2/Al</b>	1198	$1.72 \times 10^{-8}$	0.819	$3.33 \times 10^4$	$7.66 \times 10^{-9}$	0.98	$8.82 \times 10^6$

Furthermore, in Figure 4.10 (c), two time constants can be found in the Bode phase plot, while only one time constant was observed for as-received aluminum. As for the superhydrophobic thin films on Al substrate, the high-frequency time constant (around  $1.0 \times 10^4$  Hz) was assigned to the capacitance of superhydrophobic cobalt stearate thin films on top of the aluminum substrate. Another low-frequency time constant (around 30 Hz) was due to the capacitance of the double layer near aluminum

surface, which has been slightly shifted to a lower frequency as compared to that of as-received aluminum (around 60 Hz), indicating the anti-corrosion properties were improved by fabricating a honeycomb-like framework of cobalt stearate on aluminum surface to isolate the salt solution[45-47]. It is to mention that the use of EIS to study corrosion protection of non-superhydrophobic silane coated Mg alloys shows similar protection properties [45]. Figure 4.10 (b) shows the Bode plots, which present the modulus of impedance ( $|Z|$ ) as a function of frequency, for the as-received aluminum and superhydrophobic thin films on Al substrate, respectively. Due to the fact that the plot at low frequency was messy and illogical, the EIS plot for as-received aluminum was only obtained for a narrow range. Actually, it is quite a common problem because of poor conductivity [48-50]. As shown in Figure 4.10 (b), at the specific high frequency of  $1.0 \times 10^4$  Hz, the  $|Z|$  value of as-received aluminum (bottom section) was only  $13.8 \Omega \cdot \text{cm}^2$ , which is quite comparable to the result of  $11.6 \Omega \cdot \text{cm}^2$  reported by Ying *et al.* In contrast, the superhydrophobic thin films on Al substrate (top section) exhibited a  $|Z|$  value as high as  $10.2 \text{ k}\Omega \cdot \text{cm}^2$ . Similarly, at a low frequency of 1Hz, the modulus of impedance for as-received aluminum was found to be  $6.97 \text{ k}\Omega \cdot \text{cm}^2$ . However, superhydrophobic thin films on Al substrate reached up to  $8220 \text{ k}\Omega \cdot \text{cm}^2$ . In the whole frequency range, the impedance of the superhydrophobic surface was positively shifted by approximately three orders of magnitude. It has been proven that larger impedance values at lower frequencies lead to more effective protection against corrosion. Therefore, both the Nyquist plots (a) and Bode plots (b,c) indicate that superhydrophobic cobalt stearate films can significantly elevate the anti-corrosion

properties of aluminum alloy substrate.

He *et al.*[51] prepared a superhydrophobic surface by melting myristic acid, which was then adsorbed onto anodized aluminum. The electrochemical impedance spectroscopy measurements were conducted after 1 h immersion time in 3.2 wt% NaCl aqueous solution. When compared to an untreated aluminum surface, the  $|Z|$  value of the superhydrophobic surface was improved by approximately two orders of magnitude, demonstrating an inferior anti-corrosion effect as compared with our method. In the study conducted by Xu *et al.*[38], the  $|Z|$  value of superhydrophobic copper stearate coated aluminum was found increased by three orders of magnitude as compared to chemically cleaned aluminum. However, the  $|Z|$  value reported by Xu *et al.* was approximately one order of magnitude lower than the present study. This could be explained in two ways: our superhydrophobic surface featured of a honeycomb-like framework is more compact than the rose petal-like structure as observed in the SEM image, with the trapped air layer retarding the penetration of corrosive medium into the sub-aluminum substrate. On the other hand, as mentioned before, the high-capacitance cobalt oxide which exists in the superhydrophobic thin film could improve the impedance.

In order to better understand the mechanisms of the chemical corrosion process on the interface, two appropriate electrical equivalent circuits (EEC) were used to fit the EIS data of as-received aluminum and superhydrophobic thin films on Al substrates. The results have been shown in Figure 4.10 (d). In the present study, the constant phase element (CPE) was employed to replace the ideal electrical capacitance in the circuits



due to the fact that the CPE better describes behaviors of the films having heterogeneities in the microstructure and in the chemical composition[52]. In Figure 4.10 (d1), the EEC for as-received aluminum was illustrated as an ohmic resistance  $R_s$  in series followed by a  $CPE_{dl}$ - $R_{ct}$  parallel combination. In this circuit,  $R_s$  is the solution resistance;  $CPE_{dl}$  and  $R_{ct}$  respectively stand for the capacitance and charge transfer resistances of the double layer formed at the interface between bare aluminum surface and the corrosive solution. The impedance of the CPE can be expressed as:

$$Z_{CPE} = \frac{1}{Y_0(j\omega)^n} \quad (4.11)$$

where  $Y_0$  is a frequency-independent constant,  $j$  is an imaginary unit,  $\omega$  is an angular frequency ( $\omega = 2\pi f$ ),  $n$  is the CPE exponent ( $0 \leq n \leq 1$ ).

The exponent equals to 1 when the element is a pure capacitor. However, the practical “double layer capacitor” cells behave like a CPE instead of a pure capacitor. The exponent ( $n$ ) for a constant phase element is normally observed to be less than one, due to surface roughness, non-uniform current distribution and ‘leaky’ capacitor *etc.* As for the as-received aluminum, the  $CPE_{dl}$  was considered as a pure capacitor because the  $n_{dl}$  value is unitary in the present study. The capacitance was calculated to be  $1.08 \times 10^{-5}$  F/cm<sup>2</sup>.  $R_s$  and  $R_{ct}$  were calculated as  $14.13 \Omega \cdot \text{cm}^2$  and  $8.42 \text{ k}\Omega \cdot \text{cm}^2$  in this circuit respectively, and have been summarized in Table 3. Additionally, another electrical equivalent circuit including two  $CPE_{dl}$ - $R_{ct}$  parallel combinations, corresponding with

the two time constant as shown in Figure 4.10 (c), was employed to describe the situation of the superhydrophobic thin films on Al. The  $CPE_f-R_f$  couple, related to the high-frequency time constant, was attributed to the dielectric character of the superhydrophobic cobalt stearate films ( $CPE_f$ ) as well as the resistance dictated by the ionic path/pores through the superhydrophobic film ( $R_f$ ). Additionally, the  $CPE_{dl}-R_{ct}$  couples, related to the low-frequency time constant, were ascribed to the double layer capacitance at the interface near the aluminum surface ( $CPE_{dl}$ ) and the charge transfer resistance at the bottom of pores in the superhydrophobic film ( $R_{ct}$ ). It is to mention that, the use of EIS to study corrosion protection of non-superhydrophobic silane coated Mg alloys shows similar protection properties [45]. All the values of those corresponding electrochemical elements were summarized in Table 2. The inhibition efficiency ( $\eta$ ) of the superhydrophobic film can be defined by the following equation[50, 53]:

$$\eta = \frac{R_{ct} - R_{ct0}}{R_{ct}} \times 100\% \quad (4.12)$$

where  $R_{ct}$  is the charge transfer resistance of the aluminum substrate coated by superhydrophobic films, and  $R_{ct0}$  is the charge transfer resistance of as-received aluminum substrate.

In our case, with  $R_{ct}$  ( $8820 \text{ k}\Omega \cdot \text{cm}^2$ ) and  $R_{ct0}$  ( $8.42 \text{ k}\Omega \cdot \text{cm}^2$ ), the inhibition effect is calculated as 99.91%. Moreover, the  $R_f$  of the superhydrophobic cobalt stearate film is calculated as high as  $33.3 \text{ k}\Omega \cdot \text{cm}^2$ . All of these observations indicate excellent barrier

properties of the thin film by inhibiting the penetration of ions such as  $\text{Na}^+$  and  $\text{Cl}^-$  through the pores into the inner aluminum substrate. It is well known that the CPE can be used to account for the roughness of the solid electrode, whereby the lower the value of the exponent ( $n$ ), the rougher the electrode surface[53]. In this circuit for superhydrophobic thin films on Al substrate, the  $n_{\text{dl}}$  was found to be 0.998. That is to say, the inner film/aluminum interface was approximately an ideal capacitor due to the flat surface of as-received aluminum. In contrast, the  $n_{\text{f}}$  value was demonstrated as 0.819, indicating the electrolyte/film interface was characterized by heterogeneities in the microstructure and the chemical composition as shown in the literatures [8, 48, 53]. These results are in good agreement with the fact that the superhydrophobic cobalt stearate film features honeycomb-like topography, as evident by SEM, XRD and FTIR spectra. Huang *et al.* studied the corrosion behavior of a superhydrophobic etched aluminum surface passivated by stearic acid with electrically equivalent circuits. They also employed two couples of R-CPE elements to represent two time constants as observed clearly in their bode plot. However, the fitted results for their two electrical circuits were not shown in details. Finally, the assumption of the electrical equivalent circuits was well supported by other researchers [45, 48, 52].

## 4.4 Summary

A simple, one-step and environment-friendly method was utilized to fabricate a superhydrophobic surface on aluminum alloy substrate via a simple electrodeposition process in an ethanolic solution containing stearic acid and cobalt nitrate. The

cooperation of rough honeycomb-like framework and cobalt stearate with low surface energy plays a significant role in the formation of the superhydrophobic surface. It was found that the surface morphology, composition and wetting properties varied according to the molar ratio of Co/SA in the electrolyte. The optimum superhydrophobic surface was obtained from the cathodic aluminum substrate electrochemically modified in the mixed solution with a Co/SA molar ratio of 0.2, with a maximum contact angle of  $161^\circ$  and a largest polarization resistance of  $1591 \text{ k}\Omega \cdot \text{cm}^2$ . A plausible mechanism of two simultaneous reactions have been illustrated clearly to explain this phenomenon. Moreover, two appropriate electrical equivalent circuits were utilized to analyze the EIS data of as-received aluminum and superhydrophobic aluminum substrate. The corresponding charge transfer resistance increased sharply from  $8.42 \text{ k}\Omega \cdot \text{cm}^2$  to  $8820 \text{ k}\Omega \cdot \text{cm}^2$ , indicating superhydrophobic cobalt stearate coated aluminum has a superior anti-corrosion property than as as-received aluminum. It is also expected that such a technique may open a new approach to expand the applications of aluminum alloys.

## Reference

- [1] Sas I, Gorga RE, Joines JA, Thoney KA. Literature review on superhydrophobic self-cleaning surfaces produced by electrospinning. *Journal of Polymer Science Part B: Polymer Physics*. 2012;50:824-45.
- [2] Manca M, Cannavale A, De Marco L, Arico AS, Cingolani R, Gigli G. Durable superhydrophobic and antireflective surfaces by trimethylsilanized silica nanoparticles-based sol-gel processing. *Langmuir*. 2009;25:6357-62.
- [3] Huang Y, Sarkar DK, Chen XG. Superhydrophobic nanostructured ZnO thin films on aluminum alloy substrates by electrophoretic deposition process. *Applied Surface Science*. 2015;327:327-34.
- [4] Huang Y, Sarkar DK, Grant Chen X. Superhydrophobic aluminum alloy surfaces prepared by chemical etching process and their corrosion resistance properties. *Applied Surface Science*. 2015;356:1012-24.

- [5] Cho WK, Park S, Jon S, Choi IS. Water-repellent coating: formation of polymeric self-assembled monolayers on nanostructured surfaces. *Nanotechnology*. 2007;18:395602.
- [6] Liang J, Hu Y, Wu Y, Chen H. Facile formation of superhydrophobic silica-based surface on aluminum substrate with tetraethylorthosilicate and vinyltriethoxysilane as co-precursor and its corrosion resistant performance in corrosive NaCl aqueous solution. *Surface and Coatings Technology*. 2014;240:145-53.
- [7] Saleema N, Sarkar DK, Gallant D, Paynter RW, Chen XG. Chemical nature of superhydrophobic aluminum alloy surfaces produced via a one-step process using fluoroalkyl-silane in a base medium. *ACS applied materials & interfaces*. 2011;3:4775-81.
- [8] Liu Y, Zhang J, Li S, Wang Y, Han Z, Ren L. Fabrication of a superhydrophobic graphene surface with excellent mechanical abrasion and corrosion resistance on an aluminum alloy substrate. *RSC Adv*. 2014;4:45389-96.
- [9] Qiu R, Zhang D, Wang P, Zhang XL, Kang YS. Tunable electrochemical preparation of cobalt micro/nanostructures and their morphology-dependent wettability property. *Electrochimica Acta*. 2011;58:699-706.
- [10] Xiao H, Hu A, Hang T, Li M. Electrodeposited nanostructured cobalt film and its dual modulation of both superhydrophobic property and adhesiveness. *Applied Surface Science*. 2015;324:319-23.
- [11] Moulapanah-Konaroi M, Aliahmad M, Saravani H. Fabrication of superhydrophobic surface by Co<sub>3</sub>O<sub>4</sub> nanoparticles. *Indian Journal of Physics*. 2012;87:211-5.
- [12] Basu BJ, Manasa J. Reversible switching of nanostructured cobalt hydroxide films from superhydrophobic to superhydrophilic state. *Applied Physics A*. 2011;103:343-8.
- [13] Chen Z, Li F, Hao L, Chen A, Kong Y. One-step electrodeposition process to fabricate cathodic superhydrophobic surface. *Applied Surface Science*. 2011;258:1395-8.
- [14] Liu Q, Chen D, Kang Z. One-step electrodeposition process to fabricate corrosion-resistant superhydrophobic surface on magnesium alloy. *ACS applied materials & interfaces*. 2015;7:1859-67.
- [15] Chen Z, Hao L, Chen A, Song Q, Chen C. A rapid one-step process for fabrication of superhydrophobic surface by electrodeposition method. *Electrochimica Acta*. 2012;59:168-71.
- [16] Chen Z, Hao L, Chen C. A fast electrodeposition method for fabrication of lanthanum superhydrophobic surface with hierarchical micro-nanostructures. *Colloids and Surfaces A: Physicochemical and Engineering Aspects*. 2012;401:1-7.
- [17] Huang Y, Sarkar DK, Chen XG. A one-step process to engineer superhydrophobic copper surfaces. *Materials Letters*. 2010;64:2722-4.
- [18] Chen Z, Hao L, Duan M, Chen C. Electrodeposition fabrication of Co-based superhydrophobic powder coatings in non-aqueous electrolyte. *Applied Physics A*. 2012;111:581-5.
- [19] Gönen M, Egbuchunam TO, Balköse D, İnal F, Ülkü S. Preparation and characterization of magnesium stearate, cobalt stearate, and copper stearate and their effects on poly(vinyl chloride) dehydrochlorination. *Journal of Vinyl and Additive Technology*. 2015;21:235-44.
- [20] Liu Q, Guo X, Li Y, Shen W. Synthesis of Hollow Co Structures with Netlike Framework. *Langmuir*. 2009;25:6425-30.
- [21] Aluminum JCPDS # 01-085-1327.

- [22] Siddaramanna A, Saleema N, Sarkar DK. A versatile cost-effective and one step process to engineer ZnO superhydrophobic surfaces on Al substrate. *Applied Surface Science*. 2014;311:182-8.
- [23] Liu Q, Kang Z. One-step electrodeposition process to fabricate superhydrophobic surface with improved anticorrosion property on magnesium alloy. *Materials Letters*. 2014;137:210-3.
- [24] Luo X. Structure of Cobalt Stearate and Cobalt Sulfide-Stearic Acid Langmuir-Blodgett Films. *Langmuir*. 1994;10:3213-6.
- [25] Tang C-W, Wang C-B, Chien S-H. Characterization of cobalt oxides studied by FT-IR, Raman, TPR and TG-MS. *Thermochimica Acta*. 2008;473:68-73.
- [26] Ghosh D, Giri S, Das CK. Preparation of CTAB-Assisted Hexagonal Platelet Co(OH)<sub>2</sub>/Graphene Hybrid Composite as Efficient Supercapacitor Electrode Material. *ACS Sustainable Chemistry & Engineering*. 2013;1:1135-42.
- [27] Athar T, Hakeem A, Topnani N, Hashmi A. Wet Synthesis of Monodisperse Cobalt Oxide Nanoparticles. *ISRN Materials Science*. 2012;2012:1-5.
- [28] Li J, Wu R, Jing Z, Yan L, Zha F, Lei Z. One-step spray-coating process for the fabrication of colorful superhydrophobic coatings with excellent corrosion resistance. *Langmuir*. 2015;31:10702-7.
- [29] Xie H, Tang S, Gong Z, Vongehr S, Fang F, Li M, et al. 3D nitrogen-doped graphene/Co(OH)<sub>2</sub>-nanoplate composites for high-performance electrochemical pseudocapacitors. *RSC Adv*. 2014;4:61753-8.
- [30] Gao L. Contact Angle Hysteresis Explained. *Langmuir*. 2006;22:6234-7.
- [31] Garoff N, Zauscher S. The Influence of Fatty Acids and Humidity on Friction and Adhesion of Hydrophilic Polymer Surfaces. *Langmuir*. 2002;18:6921-7.
- [32] Saleema N, Farzaneh M. Thermal effect on superhydrophobic performance of stearic acid modified ZnO nanotowers. *Applied Surface Science*. 2008;254:2690-5.
- [33] Hosono E, Fujihara S, Honma I, Zhou H. Superhydrophobic Perpendicular Nanopin Film by the Bottom-Up Process. *J AM CHEM SOC*. 2005;127:13458-9.
- [34] Brassard JD, Sarkar DK, Perron J. Synthesis of monodisperse fluorinated silica nanoparticles and their superhydrophobic thin films. *ACS applied materials & interfaces*. 2011;3:3583-8.
- [35] Huang Y, Sarkar DK, Gallant D, Chen XG. Corrosion resistance properties of superhydrophobic copper surfaces fabricated by one-step electrochemical modification process. *Applied Surface Science*. 2013;282:689-94.
- [36] Xu N, Sarkar DK, Chen XG, Tong WP. Corrosion performance of superhydrophobic nickel stearate/nickel hydroxide thin films on aluminum alloy by a simple one-step electrodeposition process. *Surface and Coatings Technology*. 2016;302:173-84.
- [37] Makhoulouf SA. Magnetic properties of Co<sub>3</sub>O<sub>4</sub> nanoparticles. *Journal of Magnetism and Magnetic Materials*. 2002;246:184-90.
- [38] Na Xu, D. K. Sarkar, X. Grant Chen, Zhang' H, Tong W. Superhydrophobic copper stearate/copper oxide thin films by a simple one-step electrochemical process and their corrosion resistance properties. *RSC Adv*. 2016;6:35466-78.
- [39] Zhang B, Li Y, Hou B. One-step electrodeposition fabrication of a superhydrophobic surface on an

aluminum substrate with enhanced self-cleaning and anticorrosion properties. *RSC Adv.* 2015;5:10000-10.

[40] Besra L, Liu M. A review on fundamentals and applications of electrophoretic deposition (EPD). *Progress in Materials Science.* 2007;52:1-61.

[41] Shinde VR, Mahadik SB, Gujar TP, Lokhande CD. Supercapacitive cobalt oxide (Co<sub>3</sub>O<sub>4</sub>) thin films by spray pyrolysis. *Applied Surface Science.* 2006;252:7487-92.

[42] Liu Q-c, Xu J-j, Chang Z-w, Zhang X-b. Direct electrodeposition of cobalt oxide nanosheets on carbon paper as free-standing cathode for Li-O<sub>2</sub>battery. *J Mater Chem A.* 2014;2:6081-5.

[43] Pyun SI, Moon SM. Corrosion mechanism of pure aluminium in aqueous alkaline solution. *J Solid State Electrochem.* 2000;4:267-72.

[44] Morks MF, Cole I, Corrigan P, Kobayashi A. Electrochemical Characterization of Plasma Sprayed Alumina Coatings. *Journal of Surface Engineered Materials and Advanced Technology.* 2011;01:107-11.

[45] Liu Y, Li S, Zhang J, Liu J, Han Z, Ren L. Corrosion inhibition of biomimetic super-hydrophobic electrodeposition coatings on copper substrate. *Corrosion Science.* 2015;94:190-6.

[46] Hashemzadeh M, Raeissi K, Ashrafizadeh F, Khorsand S. Effect of ammonium chloride on microstructure, super-hydrophobicity and corrosion resistance of nickel coatings. *Surface and Coatings Technology.* 2015;283:318-28.

[47] Shen GX, Chen YC, Lin L, Lin CJ, Scantlebury D. Study on a hydrophobic nano-TiO<sub>2</sub> coating and its properties for corrosion protection of metals. *Electrochimica Acta.* 2005;50:5083-9.

[48] Jie H, Xu Q, Wei L, Min Y. Etching and heating treatment combined approach for superhydrophobic surface on brass substrates and the consequent corrosion resistance. *Corrosion Science.* 2016;102:251-8.

[49] Lu Z, Wang P, Zhang D. Super-hydrophobic film fabricated on aluminium surface as a barrier to atmospheric corrosion in a marine environment. *Corrosion Science.* 2015;91:287-96.

[50] Wang P, Zhang D, Qiu R, Wan Y, Wu J. Green approach to fabrication of a super-hydrophobic film on copper and the consequent corrosion resistance. *Corrosion Science.* 2014;80:366-73.

[51] He T, Wang Y, Zhang Y, Lv Q, Xu T, Liu T. Super-hydrophobic surface treatment as corrosion protection for aluminum in seawater. *Corrosion Science.* 2009;51:1757-61.

[52] Boinovich LB, Gnedenkov SV, Alpysbaeva DA, Egorkin VS, Emelyanenko AM, Sinebryukhov SL, et al. Corrosion resistance of composite coatings on low-carbon steel containing hydrophobic and superhydrophobic layers in combination with oxide sublayers. *Corrosion Science.* 2012;55:238-45.

[53] Liu T, Yin Y, Chen S, Chang X, Cheng S. Super-hydrophobic surfaces improve corrosion resistance of copper in seawater. *Electrochimica Acta.* 2007;52:3709-13.

## **5. Ultra-Violet durable superhydrophobic thin films coated aluminum alloys**

In the current research, two different approaches have been employed to develop UV durable superhydrophobic coatings. Firstly, the UV durable superhydrophobic cobalt stearate (CoSA) coatings have been fabricated on aluminum alloy substrates by one-step electrodeposition in a mixed ethanolic solution containing cobalt nitrate and stearic acid. Furthermore, by sol-gel/spin-coating process, another UV-durable superhydrophobic PMHS/TiO<sub>2</sub>@CoSA nanocomposite coating has been prepared on aluminum substrates by embedding TiO<sub>2</sub> nanoparticles, which are coated by our chemically synthesized cobalt stearate, in a hydrophobic polymethylhydrosiloxane matrix. These approaches to the generation of superhydrophobic coatings with UV resistance properties will contribute to the potential applications in harsh environments.

### **5.1 UV durable superhydrophobic cobalt stearate thin films prepared by one-step electrodeposition**

#### **5.1.1 Introduction**

Superhydrophobic surfaces with “the lotus effect” have attracted increasing attention during the past decades due to their great potential in widespread applications such as anti-corrosion[1, 2], self-cleaning[3], drag reduction[4] etc. However, most of them are vulnerable and lose their superhydrophobic properties in the solar light due to the effect of photo-triggered degradation, especially by ultraviolet light (UV). It has



been known that commercially available polymers, organic silanes and acids can be decomposed gradually under UV irradiation [5-8]. Therefore, to realize a wide application in our real life, it is extremely significant to impart the property of UV durability to the superhydrophobic coatings, because the longevity of superhydrophobic coatings will dramatically decrease under the irradiation of UV light which commonly exists in the solar light.

As reported, most of the superhydrophobic coatings will lose their superhydrophobicity as a consequence of photo-oxidation processes by forming hydroxyl groups on the surface under UV irradiation. For example, Xia *et al.*[9] have fabricated a self-cleaning superhydrophobic surface based on titanium dioxide nanowires combined with polydimethylsiloxane (PDMS) by a dip-coating process. It could be explained by the fact that TiO<sub>2</sub> activated by UV irradiation shows a great ability of photocatalysis which can decompose PDMS and generate plenty of hydroxyl groups. To date, several approaches have been developed to fabricate UV durable superhydrophobic surfaces. Ding *et al.*[10] reported creating a superhydrophobic coating with UV resistance properties by blending fluorinated polysiloxane and different weight percents of TiO<sub>2</sub> nanoparticles. As they explained, the chemical bond of Si-O and C-F with bonding energy up to 460 and 485 kJ mol<sup>-1</sup> respectively can neither be decomposed by photocatalytic TiO<sub>2</sub> (band gap: 3.2 eV or 309 kJ mol<sup>-1</sup>) nanoparticles nor by UV light (314-419 kJ mol<sup>-1</sup>). Similarly, Xiu *et al.*[11] fabricated an UV durable inorganic superhydrophobic coating using tetramethoxysilane and isobutyltri-methoxysilane as precursors by sol-gel method and further modification

with fluoroalkylsilanes. However, it should be pointed out that fluorinated silanes are quite expensive, not friendly to the environment and inappropriate for large scale applications.

In this present work, a UV durable superhydrophobic cobalt stearate surface has been fabricated on aluminum alloy substrates simply by one-step electrodeposition. The water contact angle and contact angle on our non-fluorine superhydrophobic surfaces hysteresis exhibited almost no change during two continuous months of UV degradation testing, indicating excellent UV resistance properties.

### **5.1.2 Experimental**

The aluminum (AA6061 alloy) substrates with a size of one by two inches were ultrasonically degreased in a soap solution and cleaned in ethanol as well as deionized water for 30 min. Subsequently, the electrodeposition process was performed at room temperature under a voltage of 10 V (DC) for 10 min, where the cleaned aluminum substrate was used as the cathode and the graphite plate as the anode. During the electrodeposition process, the cathode and the anode were separated by a distance of 1.5 cm. The electrolyte solution was composed of cobalt (II) nitrate hexahydrate ( $\text{Co}(\text{NO}_3)_2 \cdot 6\text{H}_2\text{O}$ ) and stearic acid ( $\text{CH}_3(\text{CH}_2)_{16}\text{COOH}$ ) in ethanol. After deposition, the sample was carefully removed from the electrolyte and dried at  $70^\circ\text{C}$  on the hotplate for 24 hours.

The morphological and elemental analyses of the modified cathodic aluminum substrates were performed using a scanning electron microscope (SEM, JEOL JSM-

6480 LV) equipped with energy dispersive X-ray spectroscopy (EDX). The chemical composition as well as structure were analyzed by X-ray diffraction (XRD, D8 discover with Cu K $\alpha$  wavelength 0.154 nm) as well as by Attenuated Total Reflectance (ATR, Agilent Technologies Cary 630 FTIR). The surface wettability of the coated samples was conducted by measuring static and dynamic contact angles of a 10  $\mu$ L water drop using a First Ten Angstrom contact angle goniometer. The roughness measurements were carried out on the MicroXAM-100 HR 3D surface profilometer.

### 5.1.3 Results and discussions

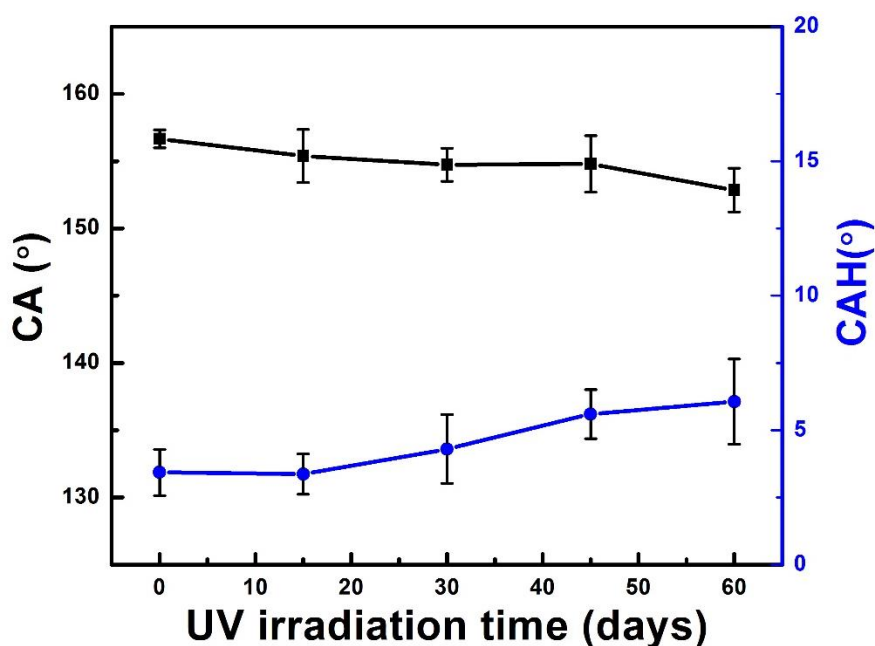


Figure 5. 1 Water contact angle (black square) and contact angle hysteresis (blue dot) on the surface of the electrodeposited cobalt stearate film as a function of UV irradiation time

Figure 5.1 shows the evolution of the water contact angle (CA, black square) and

contact angle hysteresis (CAH, blue dot) on the surface of the electrodeposited cobalt stearate film over the course of the UV degradation test. Initially, the superhydrophobic cobalt stearate-based surface exhibited a water contact angle of  $156.6 \pm 0.6^\circ$  as well as a contact angle hysteresis of  $3.4 \pm 0.8^\circ$ . After keeping the sample under UV irradiation with two UV lamps having the corresponding wavelengths of 302 nm and 365 nm for two month, the contact angles and contact angle hysteresis' were found to be  $152.4 \pm 1.4^\circ$  and  $6.0 \pm 1.6^\circ$  respectively. These results indicate that the surface can resist UV degradation and sustain rolling-off properties. In the past decades, many UV durable superhydrophobic coatings are fabricated based on fluoroalkylsilanes with very strong bonds like Si-O, C-F etc. Compared with these coatings, our CoSA superhydrophobic coatings have great advantages such as simple and low-cost fabrication, which is expected to be appropriate for a wide range of applications. Moreover, further analyses also confirmed the superhydrophobic cobalt stearate-based surfaces are UV-durable by ATR-FTIR and SEM.

Figure 5.2(a) shows the SEM image of the superhydrophobic cobalt stearate film fabricated on aluminum substrates by electrodeposition before UV degradation test. This superhydrophobic cobalt stearate surface exhibited a surface roughness value of  $1.8 \mu\text{m}$  as well as a water contact angle value of  $156^\circ$  (shown in the inset). It is worth noting that, in our case, the rolling-off properties are governed by the

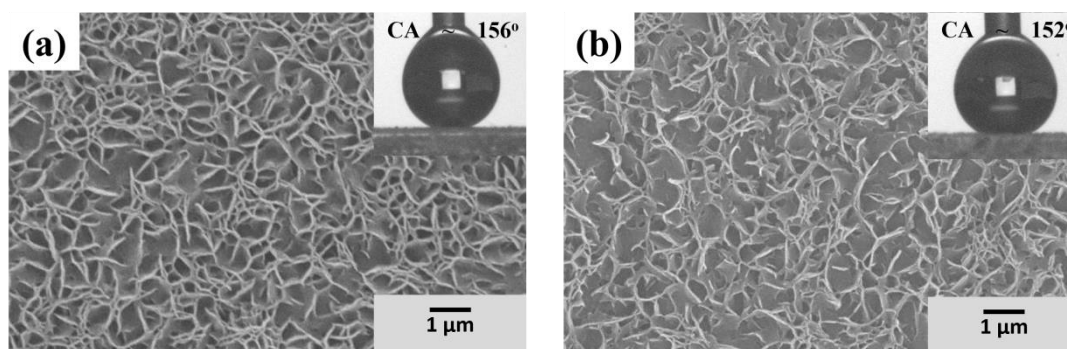


Figure 5. 2 SEM images of electrodeposited cobalt stearate film (a) before and (b) after UV degradation for 60 days. The insets show the water drop on the corresponding surfaces

honeycomb-like rough structure and low-surface-energy cobalt stearate. Figure 5.2(b) shows the morphology of our superhydrophobic cobalt stearate film after UV degradation for 60 days. Though a few fibers in the honeycomb structure of cobalt stearate were broken up due to the exposure in the UV light for quite a long time, this cobalt stearate-based surface was still superhydrophobic with the surface roughness and water contact angle slightly decreasing to 1.6 $\mu$ m and 152 $^{\circ}$  respectively. Moreover, the UV degradation effect has also been evaluated by the image analysis technique. The fractions of the solid surface before and after UV irradiation were found to be 10.19% and 9.49%, respectively. This implies that only 0.7% of the solid surface area was lost during the 2 months of UV degradation testing.

Figure 5.3 reveals the ATR-FTIR spectra of (a) pure SA powder, and electrodeposited CoSA (b) before and (c) after UV degradation. In the high frequency region of the two spectra, the adsorption peaks at 2847 $\text{cm}^{-1}$  and 2914  $\text{cm}^{-1}$  are attributed to the asymmetric and symmetric stretching vibrations of  $-\text{CH}_2$  groups,

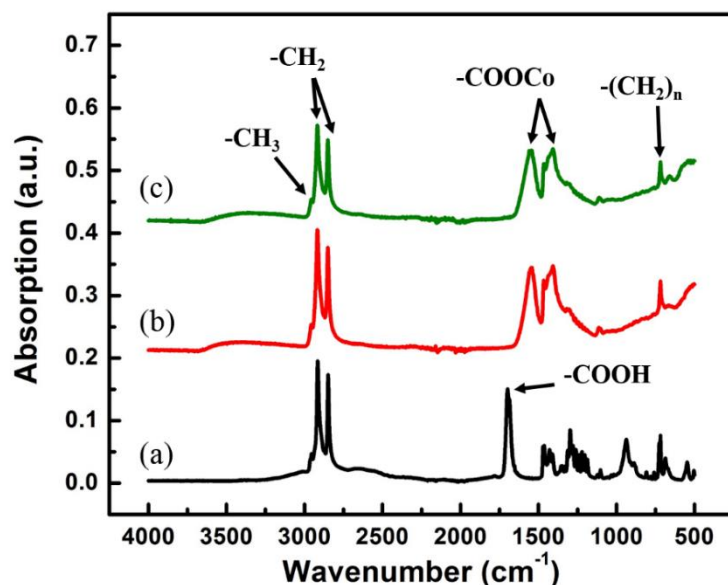


Figure 5. 3 ATR-FTIR spectra of (a) stearic acid powder; the electrodeposited cobalt stearate film (b) before and (c) after UV degradation for 60 days

respectively. One tiny peak is assigned to the asymmetric stretching of  $-\text{CH}_3$  which is present at  $2939\text{ cm}^{-1}$ . In the low frequency region, the peak for the carboxyl ( $-\text{COOH}$ ) group of stearic acid at  $1701\text{ cm}^{-1}$  is no longer present at the spectrum of cobalt stearate. In addition, two new peaks centered at  $1410\text{ cm}^{-1}$  and  $1550\text{ cm}^{-1}$  corresponding with the carboxylate ( $-\text{COOCo}$ ) symmetric and asymmetric stretching vibrations were clearly observed. A sharp absorption peak at  $720\text{ cm}^{-1}$  is ascribed to the in-plane rocking vibrations of  $-(\text{CH}_2)_n$  long carbon chains in cobalt stearate molecule [12].

### 5.1.4 Summary

In summary, a simple and low-cost method has been developed to fabricate UV tolerant superhydrophobic cobalt stearate coatings on aluminum alloy substrates simply by one-step electrodeposition in a mixed ethanolic solution containing cobalt nitrate

and stearic acid. This non-fluorine superhydrophobic surface demonstrated excellent UV resistance properties during the accelerated UV degradation test with no change in wettability, morphology and chemical compositions as confirmed by contact angle test, SEM as well as ATR-FTIR, respectively.

## **5.2 UV durable PMHS/TiO<sub>2</sub>@CoSA superhydrophobic coatings by sol-gel/spin-coating process**

### **5.2.1 Introduction**

Superhydrophobicity, inspired by the “Lotus effect” in nature, is featured of having a water contact angle above 150°. The water repellency of a surface is governed by a combination of chemical composition and geometrical surface structure. Superhydrophobic thin films have attracted great attentions on a wide range of applications including antifouling paints [13], waterproof clothes[14], corrosion inhibition[1], water and oil separation[15] *etc.* Recently, superhydrophobic thin films incorporated wide band gap semiconductor oxide nanoparticles such as TiO<sub>2</sub> (Band gap: 3.2 eV), ZnO (3.4 eV), CeO<sub>2</sub> (3.1 eV) *etc.* have attracted increased interest due to their UV absorption and self-cleaning properties [16-23]. However, most of them can be easily converted into hydrophilic surfaces under UV irradiation as a consequence of highly photocatalytic activity, with the corresponding wetting state from Cassie mode[24] to Wenzel mode[25]. For example, Nishimoto *et al.*[26] reported a superhydrophobic TiO<sub>2</sub>-based porous surface passivated by a self-assembled

monolayer of octadecylphosphonic acid, exhibiting a water contact angle (WCA) of 154°. However, the surface rapidly lost its hydrophobicity and was transformed to a superhydrophilic state in 30 min, with a CA of nearly 0°, due to the photocatalytic decomposition of the ODP monolayer. Similarly, the work of PDMS coated TiO<sub>2</sub> nanoparticles become hydrophilic in six hours due the UV-exposure as reported by Zhang *et al.*[9].

To date, several approaches have been reported on fabricating UV durable superhydrophobic coatings which incorporate photocatalytic nanoparticles. Kim *et al.*[27] utilized polydimethylsiloxane (PDMS) to confine the photocatalytic activity of TiO<sub>2</sub> and obtained a UV durable superhydrophobic coating in a test period of 24 hours. However, in a study conducted by Zhang *et al.*[9], the superhydrophobic surface based on TiO<sub>2</sub> nanowires combined with PDMS turned into a hydrophilic one after UV irradiation for 6 hours. From the reports above, it can be seen that PDMS may not be strong enough for the confinement of the photocatalytic effect of TiO<sub>2</sub> in long term applications.

Ding *et al.*[10] reported a UV durable superhydrophobic fluorinated polysiloxane/TiO<sub>2</sub> nanocomposite coating due to the fact that Si-O and C-F bands in the fluorinated polymer matrix can't be decomposed by photocatalytic TiO<sub>2</sub> nanoparticles. However, fluorinated silanes are quite expensive, non-environmentally friendly and therefore not appropriate for practical applications. Wang *et al.*[18] prepared a SiO<sub>2</sub> coated ZnO nanowire array using a layer-by-layer deposition and obtained UV resistant superhydrophobicity after modification with an



octadecyltrimethoxysilane(OTS) monolayer. It was explained by the confinement effect of the insulating SiO<sub>2</sub> layer on the photo-generated electron-hole pairs by ZnO nanowires. Similarly, in a study of Gao *et al.*[16], a transparent and UV-durable superhydrophobic surface was fabricated by passivating the arrays of SiO<sub>2</sub>-coated ZnO nanorods with perfluorodecyltriethoxysilane (PTES). The physical barrier of the SiO<sub>2</sub> layer is responsible for the UV resistance properties. However, both of their fabrication processes are complex and a further modification of the hydrophilic SiO<sub>2</sub> shell with low surface energy materials is always inevitable.

In the present study, a simple, low-cost and effective method has been developed to fabricate UV durable superhydrophobic coatings. Initially, we prepared a superhydrophobic polymethylhydrosiloxane (PMHS)/TiO<sub>2</sub> nanocomposite coating by embedding TiO<sub>2</sub> nanoparticles in the hydrophobic PMHS matrix by sol-gel process, which was totally transitioned into superhydrophilic after UV irradiation for 4 hours due to the photocatalytic decomposition of PMHS. However, inspired by our previous work of UV durable superhydrophobic cobalt stearate coatings prepared by electrodeposition, a long-term UV-durable superhydrophobic coating was successfully fabricated simply by covering TiO<sub>2</sub> nanoparticles with our synthesized cobalt stearate and following the same steps above by sol-gel process. The PMHS/TiO<sub>2</sub>@CoSA superhydrophobic coatings exhibited a nearly constant water contact angle of 160° under continuous UV irradiation for 1 month. A plausible model has been suggested to explain the UV durable mechanism of superhydrophobic TiO<sub>2</sub> coatings. It is worth mentioning that UV-durable superhydrophobic coatings incorporating TiO<sub>2</sub>

nanoparticles can be functional as superhydrophobic surfaces as well as UV absorber layers simultaneously.

## 5.2.2 Experimental

The square aluminum (AA6061 alloy) substrates with a size of one by one inches were ultrasonically degreased in a soap solution and cleaned in ethanol as well as deionized water for 30 min. First, in the process of preparation of PMHS sol-gel, 2mL PMHS and 3mL ammonia (28%) were added into ethanol and stirred at room temperature for 2 days. Second, to prepare the PMHS/TiO<sub>2</sub> sol-gel, 1.5g anatase TiO<sub>2</sub> nanoparticle (average particle size: 100 nm) were dispersed in 51mL of ethanol, followed by ultrasonication for 1h. Then 25 mL of PMHS sol-gel were added into the TiO<sub>2</sub> nanoparticle ethanolic solution. The mixture was stirred and aged for 5 days at room temperature before the application of the spin-coating process. In the case of preparing PMHS/TiO<sub>2</sub>@CoSA sol-gel, 1.5 g anatase TiO<sub>2</sub> nanoparticle (average size : 100nm) was dispersed in the same volume of 51 mL mixed ethanolic solution composed of 17 mL cobalt nitrate (0.01 M) and 34 mL stearic acid (0.01 M) as well as with 150 μL of ammonia (28%), followed by ultrasonication for 1h. The mixture was also stirred and aged for 5 days at room temperature before the spin-coating process.

The spin-coating processes were carried out using Single Wafer Spin Processor (Laurell Technologies WS-650Sz-6NPP-Lite). PMHS/TiO<sub>2</sub> and PMHS/TiO<sub>2</sub>@CoSA sol-gels were utilized to make spin-coatings with 600uL per layer on the clean square aluminum substrates respectively. The spin process includes 10 seconds of 500 rounds

per minute (RPM) and 10 seconds of 1000 RPM.

The morphological and elemental analyses of the aluminum substrates coated by spin-coatings were performed using a scanning electron microscope (SEM, JEOL JSM-6480 LV) equipped with energy dispersive X-ray spectroscopy (EDX). The chemical composition as well as structure were analyzed by X-ray diffraction (XRD, D8 discover with Cu K $\alpha$  wavelength 0.154 nm) as well as by Attenuated Total Reflectance Fourier Transform Infrared (ATR, Agilent Technologies Cary 630 FTIR). The surface wettability of the coated samples was conducted by measuring static and dynamic contact angles of 10  $\mu$ L water drops using a First Ten Angstrom contact angle goniometer. The roughness measurements were carried out on the MicroXAM-100 HR 3D surface profilometer. A home designed UV degradation technique (15Watt, UV light wavelength of 302 nm and 365 nm) was used to understand the UV-absorption quality of the two sets of nanoparticle incorporated coatings.

### **5.2.3 Results and discussions**

Figure 5.4 (a) shows the X-ray diffraction (XRD) patterns of (a-I) pure stearic acid (SA) powder and (a-II) cobalt stearate films on aluminum substrates in the  $2\theta$  scan range of 3-30°. The XRD pattern (a-I) shows the SA characteristic peaks at the  $2\theta$  values of 6.76, 20.35, 21.61 and 24.29, respectively. Those characteristic peaks are no longer present in the XRD spectrum (a-II), indicating the formation of cobalt stearate. The XRD pattern of cobalt stearate, as shown in Figure 5.4 (a-II), shows a series of equidistant diffraction peaks situated at 3.61°, 5.42°, 7.22°, 9.02°, 10.81°, 12.62°, 14.44°

and 16.24°,

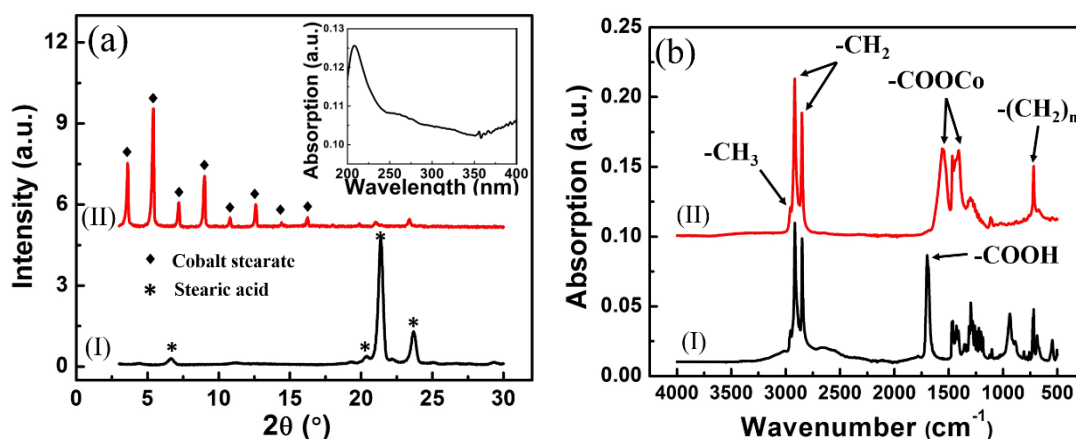


Figure 5. 4 (a) Low angle XRD patterns of (I) stearic acid powder and (II) cobalt stearate films on aluminum substrates; (b) ATR-FTIR spectra of (I) stearic acid powder and (II) cobalt stearate drop films on aluminum substrates. The inset figure in (a) shows the corresponding UV-Vis absorption spectrum of cobalt stearate

respectively. The initial peak is found at 1.81 by extrapolation since the average equidistance between neighboring diffraction peaks is calculated as  $1.80 \pm 0.01$  in our studies though it is invisible in the XRD spectrum of our synthesized cobalt stearate due to the limited  $2\theta$  scan range of 3-30°. Moreover, in a study by Luo *et al.*[28], a distinct peak was observed at similar position (approximately 1.8) in the XRD patterns of 25-layers Langmuir-Blodgett film of cobalt stearate, indicating our extrapolation result is logical and plausible. Compared with their results, our synthesized cobalt stearate showed more distinct X-ray diffraction peaks, which is more qualified for the existence of cobalt stearate.

In this study, the cobalt stearate (CoSA) XRD spectrum has been carefully analyzed through comparing with the previous work of zinc stearate (ZnSA)[4], copper

stearate (CuSA)[1] in our group as well as the XRD spectra of CoSA reported by other groups[12, 29]. As we all know, the bilayer distance of metal stearate can be determined by X-ray diffraction using Bragg equation[30]:

$$n\lambda = 2d \sin \theta \quad (5.1)$$

where  $\lambda$  is the wavelength of the X-ray, 0.154 nm for Cu K $\alpha$  radiation;  $n$  is the order of diffraction;  $d$  is the bilayer distance; and  $\theta$  is the diffraction peak angle.

The first four x-ray diffraction peaks for ZnSA (JCPDS # 00-055-1618) are shown at 2.08, 4.16, 6.27 and 8.75 respectively. According to the Bragg equation, the corresponding bilayer distances are calculated as 42.44 (theoretical value: 42.48), 21.22(21.32), 14.09(14.20) and 10.10(10.65). In addition, CuSA (JCPDS # 00-055-1622) shows its first four peaks at  $2\theta$  values of 21.91, 3.81, 5.82 and 7.75, whose bilayers are calculated as 46.34(47.52), 23.17(23.75), 15.17 (15.83) and 11.40 (11.85) respectively. Similarly, in the XRD pattern (a-II) of cobalt stearate, the distinct peaks at the  $2\theta$  values of 1.81 (by extrapolation), 3.61, 5.42 and 7.22 belong to the first four peaks, which are associated with the bilayer distances of 48.91, 24.46, 16.29 and 12.23 in sequence. Interestingly, the bilayer distances of metal stearates are found to be in a perfect order of ZnSA < CuSA < CoSA. It could be explained by the fact that Zn has the strongest electron negativity, indicating a strongest attraction and a shortest bilayer distance, followed by Cu and finally Co. The inset shows the UV-Vis absorption spectrum of our synthesized cobalt stearate in the light wavelength range of 200-400

nm. Based on the previous reports[31, 32], the distinct absorption peak centered at 220 nm is likely attributed to cobalt oxide (CoO), which is decomposed from cobalt stearate under UV excitation. It indicates that cobalt stearate poses a good potential for use as an organic UV absorber.

Figure 5.4(b) reveals the ATR-FTIR spectra of (b-I) pure SA powder and (b-II) the synthesized CoSA. In the high frequency region of the two spectra, the adsorption peaks at  $2847\text{ cm}^{-1}$  and  $2914\text{ cm}^{-1}$  are attributed to the asymmetric and symmetric stretching vibrations of  $-\text{CH}_2$  groups, respectively. One tiny peak assigned to the asymmetric stretching of  $-\text{CH}_3$  is present at  $2939\text{ cm}^{-1}$ [1, 33]. In the low frequency region, the peak for the carboxyl ( $-\text{COOH}$ ) groups of stearic acid at  $1701\text{ cm}^{-1}$  is no longer present in the spectrum of cobalt stearate[1]. In addition, two new peaks centered at  $1410\text{ cm}^{-1}$  and  $1550\text{ cm}^{-1}$  correspond with the carboxylate ( $-\text{COOCo}$ ) symmetric and asymmetric stretching vibrations which were clearly observed[12]. A sharp absorption peak at  $720\text{ cm}^{-1}$  is ascribed to the in-plane rocking vibrations of  $-(\text{CH}_2)_n$  long carbon chains in cobalt stearate molecule [12]. In other words, cobalt stearate has been successfully synthesized by incorporation of cobalt nitrate and stearic acid as evident by XRD and ATR-FTIR analysis.

Anatase phase of  $\text{TiO}_2$  nanoparticle is a well-known material to induce photo degradation [3, 22, 34] due to the self-cleaning properties. However, it has interesting UV-protection properties due to the wide photonic bandgap of 3.2 eV. Therefore, in this study, the classical material like anatase  $\text{TiO}_2$  nanoparticles of size 100 nm is used to study the photo-degradation as well as counter the photodegrading using our

synthesized CoSA in the mixture. It is extremely important to develop UV durable

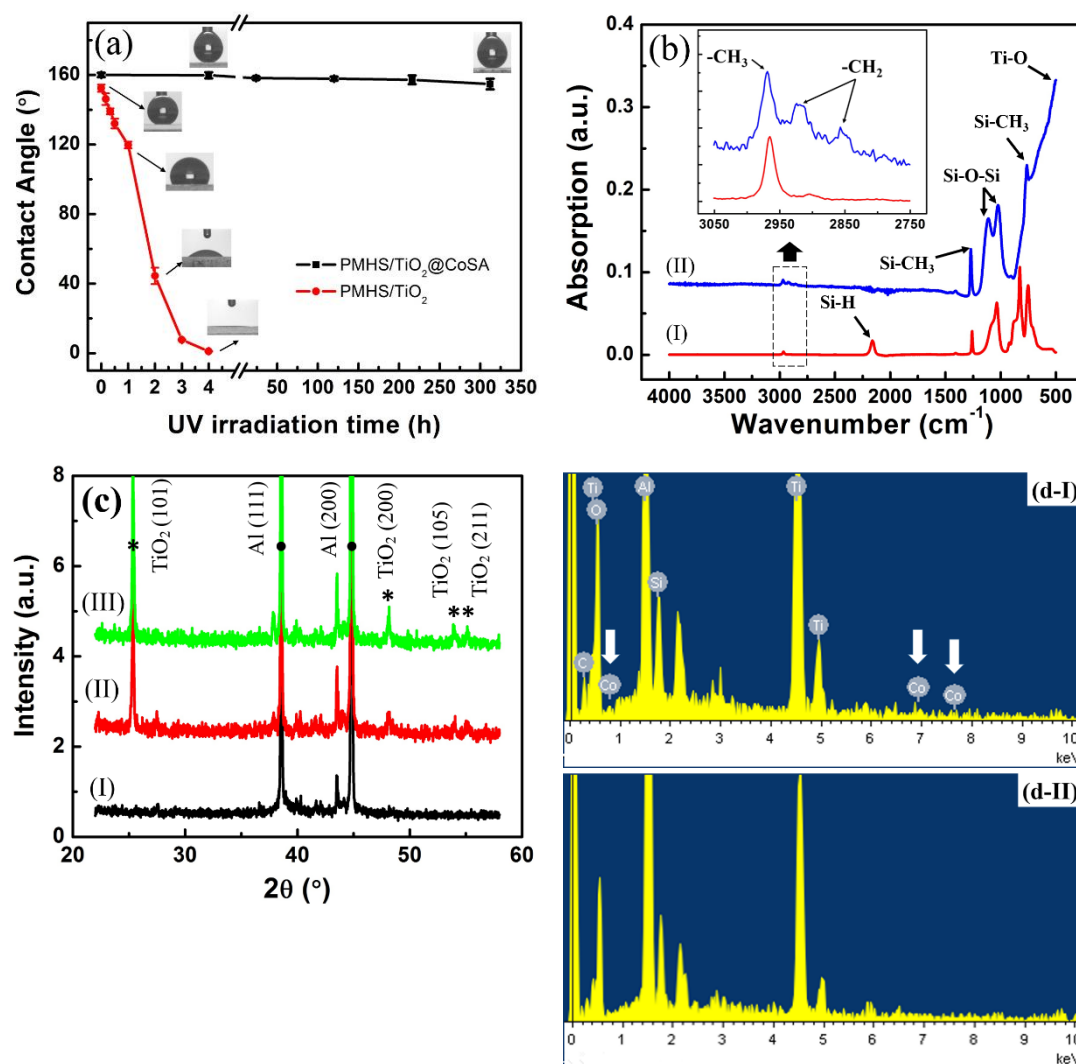


Figure 5. 5 (a) The variation of water contact angle on PMHS/TiO<sub>2</sub> and PMHS/TiO<sub>2</sub>@CoSA superhydrophobic thin films as a function of UV irradiation time. The inset images in (a) show the water drop on the corresponding surfaces respectively; (b) ATR-FTIR spectra of (I) PMHS liquid and (II) PMHS/TiO<sub>2</sub>@CoSA superhydrophobic thin films. The inset figure in (b) shows the amplificative ATR-FTIR spectra in the range from 3050 cm<sup>-1</sup> to 2750 cm<sup>-1</sup>; (c) XRD patterns of (I) aluminum substrates (II) PMHS/TiO<sub>2</sub> and (III) PMHS/TiO<sub>2</sub>@CoSA superhydrophobic thin films; (d) EDS spectra of (d-I)

## PMHS/TiO<sub>2</sub>@CoSA and (d-II) PMHS/TiO<sub>2</sub> superhydrophobic thin films

superhydrophobic coatings especially for exterior surfaces which are normally exposed to UV light. A comparative UV degradation study was conducted between PMHS/TiO<sub>2</sub> and PMHS/TiO<sub>2</sub>@CoSA superhydrophobic coatings in our homemade UV chamber. Figure 5.5 (a-red) shows the water contact angle on PMHS/TiO<sub>2</sub> coatings decreased gradually as a function of the extending UV irradiation time in 4 hours. The initial superhydrophobic PMHS/TiO<sub>2</sub> surface exhibits a water contact angle (WCA) of ~152° (shown in the inset) and contact angle hysteresis (CAH) of 6°. After one hour exposure in the UV irradiation, the water contact angle of this surface decreased to ~119°, losing the rolling-off properties. With the UV irradiation time increasing to 2 hours, the WCA of the PMHS/TiO<sub>2</sub> coatings were found to be only ~44°. The superhydrophobic PMHS/TiO<sub>2</sub> coatings were completely converted into superhydrophilicity after UV irradiation for 4 hours due to the photocatalytic effect of the anatase TiO<sub>2</sub> nanoparticles[3]. The low-surface-energy polymethylhydrosiloxane (PMHS) was decomposed by highly oxidizing O<sub>2</sub><sup>-</sup> and OH radicals generated by TiO<sub>2</sub> nanoparticles under the UV irradiation. A model has been presented at Figure. 5.6(b) to explain the degradation process. However, in Figure 5.5(a-black), the PMHS/TiO<sub>2</sub>@CoSA superhydrophobic coatings demonstrated UV-stable superhydrophobicity for more than 300 hours. Though the data has been presented for 300 hrs (apprx. 15 days) these coatings are still superhydrophobic after 30 days. Note that the intensity of the as-used UV light is much more intense than that in the sunlight, suggesting that our



PMHS/TiO<sub>2</sub>@CoSA superhydrophobic coatings may have potential applications in some extreme environmental applications, especially those exposed in intensive solar light. The initial and final water contact angles of this surface were found to be 160° (CAH=2°) and 156° (CAH=5°) respectively during the UV degradation test. This highly UV-durable superhydrophobic coating with small rolling-off angle and low-stick surface can be regarded as a good candidate of applications requiring excellent self-cleaning properties.

Figure 5.5(b) reveals the chemical groups of pure PMHS organosilanes in the liquid state and the superhydrophobic PMHS/TiO<sub>2</sub>@CoSA coatings with ATR-FTIR spectra. In the high frequency region, the spectrum of PMHS displays a single peak at 2969 cm<sup>-1</sup> (shown in the inset figure) which is assigned to the asymmetric stretching mode of the -CH<sub>3</sub> group in PMHS molecule. In the spectrum of superhydrophobic PMHS/TiO<sub>2</sub>@CoSA surfaces before UV degradation (Figure 5.5(b-II)), besides the absorption peak of -CH<sub>3</sub>, another two peaks attributed to the symmetric and asymmetric stretching mode of the -CH<sub>2</sub> group from cobalt stearate are observed at 2914 cm<sup>-1</sup> and 2853 cm<sup>-1</sup> respectively. In the low frequency region, the peak for the Si-H group of PMHS at 2162 cm<sup>-1</sup> (Figure 5.5 (b-I)) is no longer present in the spectrum of superhydrophobic PMHS/TiO<sub>2</sub>@CoSA surfaces (Figure 5.5 (b-II))[35]. This indicates that the cross-linked polymer matrix has been formed by PMHS organosilanes through the condensation reactions of Si-H groups during the sol-gel process[35]. The two peaks at 1270cm<sup>-1</sup> and 764cm<sup>-1</sup> correspond to Si-CH<sub>3</sub> groups. In addition, the double peaks present at 1112 cm<sup>-1</sup> and 1026 cm<sup>-1</sup> are ascribed to the Si-O-Si groups of PMHS

organosilanes [35]. The absorption peak of the Ti-O group is displayed at quite a low frequency region near  $500\text{ cm}^{-1}$ , confirming the existence of  $\text{TiO}_2$  nanoparticles in our UV-durable superhydrophobic coatings.

Figure. 5.5 (c) depicts the X-ray diffraction (XRD) spectra of (I) as-received aluminum substrates (II) PMHS/ $\text{TiO}_2$  and (III) PMHS/ $\text{TiO}_2$ @CoSA superhydrophobic thin films in the scan range of  $22\text{-}58^\circ$ . Two distinct peaks shown at  $38.4^\circ$  and  $44.7^\circ$  on the XRD pattern of (I) aluminum substrates are in good agreement with the characteristic peaks of Al (111) and Al (200). In addition, the XRD patterns of (II) PMHS/ $\text{TiO}_2$  and (III) PMHS/ $\text{TiO}_2$ @CoSA superhydrophobic thin films on aluminum substrates show all the characteristic peaks of aluminum as mentioned above as well as the characteristic peaks of  $\text{TiO}_2$  (101),  $\text{TiO}_2$  (200),  $\text{TiO}_2$  (105) and  $\text{TiO}_2$  (211) at  $25.3^\circ$ ,  $48.1^\circ$ ,  $53.9^\circ$  and  $55.1^\circ$ , confirming the incorporation of  $\text{TiO}_2$  nanoparticles in the thin films. In Figure. 5.5 (d), the element analysis of the superhydrophobic thin films (d-I) PMHS/ $\text{TiO}_2$ @CoSA and (d-II) PMHS/ $\text{TiO}_2$  were performed using EDS spectra. The common elements in both of the two thin films includes C, Ti, O and Si. Specially, the Co element can only be detected in the EDS spectra of (Figure. 5.5 (d-I)) PMHS/ $\text{TiO}_2$ @CoSA, indicating the existence of cobalt stearate in this superhydrophobic nanocomposite film.

The morphology of the superhydrophobic PMHS/ $\text{TiO}_2$ @CoSA coatings on aluminum substrate is evaluated using SEM, as shown in Figure 5.6(a). It is seen that a lot of micro-sized clusters, formed by the aggregation of  $\text{TiO}_2$  nano-sized particles (Diameter: 100nm) and embedded in the PMHS hydrophobic matrix, and distributed

randomly on the aluminum substrates. The binary rough micro–nanostructures passivated with cobalt stearate as well as PMHS organosilanes layers, similar to the

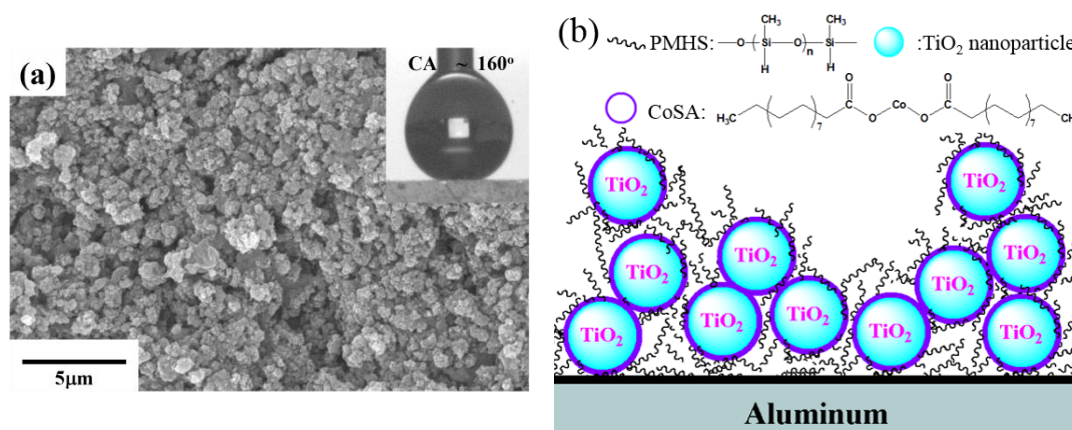


Figure 5. 6 (a) SEM image and (b) The schematic model for the

PMHS/TiO<sub>2</sub>@CoSA coatings on aluminum substrate. The inset image in (a) shows

water drops on this superhydrophobic surface

surface structure of Lotus leaves, exhibit a surface roughness of 3.3 μm and a water contact angle as high as 160°. Figure 5.6(b) shows a plausible schematic model for the PMHS/TiO<sub>2</sub>@CoSA coatings on the aluminum substrate. The surface of hydrophilic anatase TiO<sub>2</sub> nanoparticles are occupied with plenty of hydroxyl groups. When modified with cobalt stearate, those hydroxyl groups on TiO<sub>2</sub> nanoparticles surfaces were replaced by methylated stearate groups and lowered the surface energy. This is consistent with the empirical observation that superhydrophobic PMHS/TiO<sub>2</sub>@CoSA surfaces (160°) showed a larger water contact angle than superhydrophobic PMHS/TiO<sub>2</sub> surfaces (152°). The increased amount of methylated components assembled on the TiO<sub>2</sub> surfaces contribute to the longevity of the superhydrophobic PMHS/TiO<sub>2</sub>@CoSA surfaces.

Moreover, it should be emphasized that cobalt oxide (CoO), resulting from cobalt stearate decomposition under UV irradiation, also plays a vital role in the UV-durability of superhydrophobic coatings which incorporate TiO<sub>2</sub> nanoparticles. As we may know, charge electron-hole pairs are created within the anatase TiO<sub>2</sub> nanoparticles (Band gap: 3.2 eV) under UV excitation. The active electrons transfer from the conduction band to the molecular oxygen to produce superoxide anion radicals, and holes transfer to the adsorbed –OH groups to produce hydroxyl radicals of high oxidation potential. These reactions yield highly oxidizing O<sub>2</sub><sup>•-</sup> and OH radicals, which will decompose organic molecules into CO<sub>2</sub> and H<sub>2</sub>O, are the main cause for photocatalytic degradation and superhydrophilic transition. When cobalt stearate transitions into CoO, the new CoO shell on TiO<sub>2</sub> nanoparticles could form a physical barrier to inhibit the diffusion of photo-generated electron-hole pairs. In addition, the CoO shell can absorb most of the UV light, as evident by UV-Vis spectroscopy above. It indicated that almost no UV light penetrated the CoO shell to the surface of TiO<sub>2</sub> nanoparticles, thus inhibiting the photo-induced decomposition of hydrophobic PMHS matrix.

It is generally believed that inert materials like silica and alumina can be utilized to suppress the photocatalytic activity[5, 36]. In the literature, SiO<sub>2</sub> has been frequently employed to confine the photo-induced degradation and fabrication of UV durable superhydrophobic coatings incorporating photocatalytic metal oxide (e.g. TiO<sub>2</sub>, ZnO, and CeO<sub>2</sub>). The insulating SiO<sub>2</sub> shell can effectively suppress the photoactivity of the TiO<sub>2</sub> nanoparticles via the confinement effect of photogenerated electron-hole pairs due to the fact that the valence and conduction band edges of SiO<sub>2</sub> lie far lower and higher

in energy than the corresponding bands of TiO<sub>2</sub>. Wang *et al.* [18] prepared a ZnO@SiO<sub>2</sub> core-shell structure by a layer-by-layer deposition and obtained UV durable superhydrophobicity after modification with an octadecyltrimethoxysilane (OTS) monolayer. This discovery was explained by the confinement effect of insulating SiO<sub>2</sub> layer on the photogenerated electron-hole pairs by ZnO nanowires. Isimjan *et al.*[37] reported a superhydrophobic surface composed of perfluorodecyltriethoxysilane (PTES) and TiO<sub>2</sub> nanoparticles. An improved UV resistant property for the superhydrophobic surface was observed by covering TiO<sub>2</sub> surface with layers of SiO<sub>2</sub> nanoparticles, because the high energy electrons that are generated by TiO<sub>2</sub> under UV irradiation can't diffuse to the surface with the existence of physical barrier and trigger the photodegradation process of PTES. In a study by Siddiquey *et al.*[5], CeO<sub>2</sub> nanoparticles were encapsulated in silica shells by using sol-gel method assisted with microwave irradiation and the photocatalytic properties of this material were effectively inhibited by silica shells as evaluated by the sluggish oxidation of methylene blue.

However, it should be pointed out that the adoption of hydrophilic SiO<sub>2</sub> shells will affect superhydrophobic wetting state of the surface and a further modification with low surface energy material is always needed. In our case, the naturally-hydrophobic CoSA shell covering on TiO<sub>2</sub> cores not only improved hydrophobic properties of the nanocomposite surface, but also inhibited the photo-induced degradation by TiO<sub>2</sub> nanoparticles. The dual protections include methylated components assembled on the TiO<sub>2</sub> surface and a physical barrier of CoO absorbing UV as well as inhibiting photogenerated hole-electron pairs. As a result, the hydrophobic PMHS matrix will not

be decomposed by the photo-induced degradation reactions. Therefore, our superhydrophobic nanocomposite coatings, with TiO<sub>2</sub>@CoSA core-shell structure embedded in hydrophobic PMHS matrix can sustain UV irradiation and keep the superhydrophobic properties in the long term.

## 5.2.4 Summary

In summary, we have successfully prepared a UV-durable superhydrophobic nanocomposite coating simply by embedding CoSA-coated TiO<sub>2</sub> nanoparticles in a hydrophobic polymethylhydrosiloxane matrix on AA6061 aluminum substrates. Compared to the dramatic decrease of the water contact angle on the PMHS/TiO<sub>2</sub> surfaces, the PMHS/TiO<sub>2</sub>@CoSA superhydrophobic coatings exhibited a nearly constant water contact angle of 160° under continuous UV irradiation for 1 month. Our synthesized cobalt stearate not only increased the hydrophobicity of the TiO<sub>2</sub> nanoparticles surface, but also confined the photocatalytic efficiency of TiO<sub>2</sub> when it was decomposed to cobalt oxide. A plausible model has been suggested to explain the UV durable mechanism of superhydrophobic TiO<sub>2</sub> coatings. It is promising that UV-durable superhydrophobic coatings incorporating TiO<sub>2</sub> nanoparticles can be utilized in wide practical applications e.g. non-wetting UV shielding.

## Reference

- [1] Huang Y, Sarkar DK, Gallant D, Chen XG. Corrosion resistance properties of superhydrophobic copper surfaces fabricated by one-step electrochemical modification process. *Applied Surface Science*. 2013;282:689-94.
- [2] Huang Y, Sarkar DK, Grant Chen X. Superhydrophobic aluminum alloy surfaces prepared by chemical

- etching process and their corrosion resistance properties. *Applied Surface Science*. 2015;356:1012-24.
- [3] Parkin IP, Palgrave RG. Self-cleaning coatings. *Journal of Materials Chemistry*. 2005;15:1689.
- [4] Brassard J-D, Sarkar DK, Perron J. Studies of drag on the nanocomposite superhydrophobic surfaces. *Applied Surface Science*. 2015;324:525-31.
- [5] Siddiquey IA, Furusawa T, Hoshi Y-i, Ukaji E, Kurayama F, Sato M, et al. Silica coating of CeO<sub>2</sub> nanoparticles by a fast microwave irradiation method. *Applied Surface Science*. 2008;255:2419-24.
- [6] Allen NS, Edge M, Ortega A, Sandoval G, Liauw CM, Verran J, et al. Degradation and stabilisation of polymers and coatings: nano versus pigmentary titania particles. *Polymer Degradation and Stability*. 2004;85:927-46.
- [7] Allen NS, Edge M, Sandoval G. Photocatalytic Coatings for Environmental Applications. *Photochemistry and Photobiology*. 2005;81:279-90.
- [8] Nishimoto S, Kubo A, Nohara K, Zhang X, Taneichi N, Okui T, et al. TiO<sub>2</sub>-based superhydrophobic–superhydrophilic patterns: Fabrication via an ink-jet technique and application in offset printing. *Applied Surface Science*. 2009;255:6221-5.
- [9] Zhang X, Guo Y, Zhang Z, Zhang P. Self-cleaning superhydrophobic surface based on titanium dioxide nanowires combined with polydimethylsiloxane. *Applied Surface Science*. 2013;284:319-23.
- [10] Ding X, Zhou S, Gu G, Wu L. A facile and large-area fabrication method of superhydrophobic self-cleaning fluorinated polysiloxane/TiO<sub>2</sub> nanocomposite coatings with long-term durability. *Journal of Materials Chemistry*. 2011;21:6161.
- [11] Xiu Y, Hess DW, Wong CP. UV and thermally stable superhydrophobic coatings from sol-gel processing. *Journal of colloid and interface science*. 2008;326:465-70.
- [12] Gönen M, Egbuchunam TO, Balköse D, İnal F, Ülkü S. Preparation and characterization of magnesium stearate, cobalt stearate, and copper stearate and their effects on poly(vinyl chloride) dehydrochlorination. *Journal of Vinyl and Additive Technology*. 2015;21:235-44.
- [13] Chapman J, Regan F. Nanofunctionalized superhydrophobic antifouling coatings for environmental sensor applications—advancing deployment with answers from nature. *Advanced Engineering Materials*. 2012;14:B175-B84.
- [14] Zou H, Lin S, Tu Y, Liu G, Hu J, Li F, et al. Simple approach towards fabrication of highly durable and robust superhydrophobic cotton fabric from functional diblock copolymer. *Journal of Materials Chemistry A*. 2013;1:11246.
- [15] Guo P, Zhai S, Xiao Z, An Q. One-step fabrication of highly stable, superhydrophobic composites from controllable and low-cost PMHS/TEOS sols for efficient oil cleanup. *Journal of colloid and interface science*. 2015;446:155-62.
- [16] Gao Y, Gereige I, El Labban A, Cha D, Isimjan TT, Beaujuge PM. Highly transparent and UV-resistant superhydrophobic SiO<sub>2</sub>-coated ZnO nanorod arrays. *ACS applied materials & interfaces*. 2014;6:2219-23.
- [17] Qing Y, Yang C, Yu N, Shang Y, Sun Y, Wang L, et al. Superhydrophobic TiO<sub>2</sub>/polyvinylidene fluoride composite surface with reversible wettability switching and corrosion resistance. *Chemical Engineering Journal*. 2016;290:37-44.

- [18] Wang L, Zhang X, Fu Y, Li B, Liu Y. Bioinspired preparation of ultrathin SiO<sub>2</sub> shell on ZnO nanowire array for ultraviolet-durable superhydrophobicity. *Langmuir*. 2009;25:13619-24.
- [19] Nishimoto S, Becchaku M, Kameshima Y, Shirosaki Y, Hayakawa S, Osaka A, et al. TiO<sub>2</sub>-based superhydrophobic–superhydrophilic pattern with an extremely high wettability contrast. *Thin Solid Films*. 2014;558:221-6.
- [20] Xu QF, Liu Y, Lin FJ, Mondal B, Lyons AM. Superhydrophobic TiO<sub>2</sub>-polymer nanocomposite surface with UV-induced reversible wettability and self-cleaning properties. *ACS applied materials & interfaces*. 2013;5:8915-24.
- [21] Duan W, Xie A, Shen Y, Wang X, Wang F, Zhang Y, et al. Fabrication of Superhydrophobic Cotton Fabrics with UV Protection Based on CeO<sub>2</sub> Particles. *Industrial & Engineering Chemistry Research*. 2011;50:4441-5.
- [22] Kamegawa T, Shimizu Y, Yamashita H. Superhydrophobic surfaces with photocatalytic self-cleaning properties by nanocomposite coating of TiO<sub>2</sub> and polytetrafluoroethylene. *Advanced materials*. 2012;24:3697-700.
- [23] Feng X, Zhai J, Jiang L. The fabrication and switchable superhydrophobicity of TiO<sub>2</sub> nanorod films. *Angewandte Chemie*. 2005;44:5115-8.
- [24] Cassie ABD, Baxter S. Wettability of porous surfaces. *Transactions of the Faraday Society*. 1944;40:546-51.
- [25] Wenzel RN. RESISTANCE OF SOLID SURFACES TO WETTING BY WATER. *Industrial & Engineering Chemistry*. 1936;28:988-94.
- [26] Nishimoto S, Kubo A, Nohara K, Zhang X, Taneichi N, Okui T, et al. TiO<sub>2</sub>-based superhydrophobic–superhydrophilic patterns: Fabrication via an ink-jet technique and application in offset printing. *Applied Surface Science*. 2009;255:6221-5.
- [27] Kim K-D, Seo HO, Sim CW, Jeong M-G, Kim YD, Lim DC. Preparation of highly stable superhydrophobic TiO<sub>2</sub> surfaces with completely suppressed photocatalytic activity. *Progress in Organic Coatings*. 2013;76:596-600.
- [28] Luo X. Structure of Cobalt Stearate and Cobalt Sulfide-Stearic Acid Langmuir-Blodgett Films. *Langmuir*. 1994;10:3213-6.
- [29] Luo X, Zhang Z, Liang Y. Structure of Cobalt Stearate and Cobalt Sulfide-Stearic Acid Langmuir-Blodgett Films. *Langmuir*. 1994;10:3213-6.
- [30] Pope CG. X-Ray Diffraction and the Bragg Equation. *Journal of Chemical Education*. 1997;74:129.
- [31] Athar T, Hakeem A, Topnani N, Hashmi A. Wet Synthesis of Monodisperse Cobalt Oxide Nanoparticles. *ISRN Materials Science*. 2012;2012:1-5.
- [32] He X, Zhong W, Du Y. Phase- and Size-Dependent Optical and Magnetic Properties of CoO Nanoparticles. *J Phys Chem C*. 2015;119:9550-9.
- [33] Siddaramanna A, Saleema N, Sarkar DK. A versatile cost-effective and one step process to engineer ZnO superhydrophobic surfaces on Al substrate. *Applied Surface Science*. 2014;311:182-8.
- [34] Patrocínio AO, Paula LF, Paniago RM, Freitag J, Bahnemann DW. Layer-by-layer TiO<sub>2</sub>/WO<sub>3</sub> thin films as efficient photocatalytic self-cleaning surfaces. *ACS applied materials & interfaces*.



2014;6:16859-66.

[35] Zhang J, Hu X, Zhang J, Cui Y, Yuan C, Ge H, et al. A fast thermal-curing nanoimprint resist based on cationic polymerizable epoxysiloxane. *Nanoscale Res Lett.* 2012;7:380.

[36] Egerton T. The Influence of Surface Alumina and Silica on the Photocatalytic Degradation of Organic Pollutants. *Catalysts.* 2013;3:338-62.

[37] Isimjan TT, Wang T, Rohani S. A novel method to prepare superhydrophobic, UV resistance and anti-corrosion steel surface. *Chemical Engineering Journal.* 2012;210:182-7.

## **6. Superhydrophobic thin films applied on SAM modified aluminum substrates**

In the first section of this chapter, self-assembled monolayers (SAM) have been deposited on aluminum using the monomer of (3-Glycidyloxypropyl) trimethoxysilane (GPTS) organosilane. Traditional surface analysis tools are not capable of identifying the presence of SAM on a surface. Therefore, electrochemical impedance spectroscopy (EIS) has been used to determine their presence on the aluminum substrates. Furthermore, in the second section, superhydrophobic coatings incorporating TiO<sub>2</sub> nanoparticles were fabricated on SAM modified aluminum substrates by sol-gel/spin-coating process. The mechanical properties of these coatings were characterized according to American Standard Test Method (ASTM) D 3359-02.

### **6.1 Electrochemical impedance spectroscopy (EIS) studies of self-assembled monolayers (SAM) on aluminum substrates**

#### **6.1.1 Introduction**

Self-assembly [1] is defined as the spontaneous formation of complex hierarchical structures from pre-designed building blocks, typically involving multiple energy scales and multiple degrees of freedom. Generally speaking, SAMs are created by the chemisorption of "head groups" onto a substrate from either the vapor or liquid phase followed by a slow organization of "tail groups" of a molecule. Typically, head groups are connected to a molecular chain in which the terminal end can be

functionalized with groups such as  $-OH$ ,  $-NH_2$ ,  $-COOH$ , or  $-SH$  to vary the wetting and interfacial properties [2-4]. Though there exist several methods to prepare SAM [2, 3, 5-10], the two methods vapor phase [9, 10] and solution [5, 7] are commonly used. Recently, many articles have been published on the fabrication of superhydrophobic surfaces with SAM technology [8, 10-12]. J. D. Brassard [13] successfully obtained a superhydrophobic film by applying fluoroalkylsilane via self-assembly on monodispersive silica. SAMs are also reported as good candidates for anti-corrosion and adhesion promotion [5, 14]. However, papers on the characterization of SAM properties are rarely seen. The most commonly used substrate for SAM is silicon and the method implemented is scanning probe microscopy (SPM) such as atomic force microscope (AFM) [7, 15-17]. Luzinov et al. [7] have analyzed the epoxysilane SAMs' surface morphology and microstructure properties using scanning probe microscopy (SPM) and ellipsometry on single-crystal silicon wafers. SAMs have been used to improve the adhesion bonding of aluminum or plastics but no characteristic data have been presented yet [14, 18, 19]. Recently, Reis et al. [6] have studied SAM of alkane diphosphonate (Gardobond X4661) on Al 5052 alloy samples by EIS in a naturally aerated sodium sulfate solution.

In this work, SAM of (3-Glycidyloxypropyl)trimethoxysilane (GPTS) molecules were deposited on chemically cleaned AA6061 aluminum alloys surfaces by a spin-coating process. After the self-assembly process ended, we carefully studied these surfaces by EIS in the three electrode corrosion cell using diluted alkaline solutions to confirm the existence of SAM on aluminum substrates.

## 6.1.2 Experimental

One-inch-square aluminum (AA6061 alloy) substrates were ultrasonically degreased in a soap solution and cleaned in deionized water for 30 min. The clean Al substrates were prepared with etching in a 1 M sodium hydroxide alkaline solution for 5 min at room temperature, followed by oxide removal via an immersion in 10 vol. % HNO<sub>3</sub> for a minute as well as rinsing in deionized water and ethanol followed by drying at room temperature. An ethanolic solution containing 1 vol. % GPTS organosilane was prepared by stirring the mixture for 30 min before spin-coating. This solution was poured on Al substrates, covering them completely before the spinning was started. The spin coated GPTS films on aluminum substrates were dried at 110 °C, on a hotplate. This sample is called SAM/Al substrate in the manuscript.

The presence of SAMs were investigated via electrochemical experiments including open circuit potential (OCP), electrochemical impedance spectroscopy (EIS) and potentiodynamic polarization experiments (Tafel) in a  $1.0 \times 10^{-4}$  M NaOH solution (pH 10). Electrochemical experiments were carried out on a PGZ100 potentiostat and a 300 cm<sup>3</sup> –EG&G PAR flat cell (London Scientific, London, ON, Canada), equipped with a standard three-electrode system with an Ag/AgCl reference electrode, a platinum mesh as the counter electrode, and the sample as the working electrode at room temperature. The morphological and elemental analyses of the samples were performed using a scanning electron microscope (SEM, JEOL JSM-6480 LV) equipped with energy dispersive X-ray spectroscopy (EDX). The chemical composition of the surfaces was analyzed by Fourier Transform Infrared spectroscopy (FTIR, Agilent

Technologies Cary 630 FTIR).

### 6.1.3 Results and discussion

Figure 6.1 (a) shows an ATR-FTIR spectrum of pure GPTS organosilanes in the liquid state. The spectrum displays a strong band at  $1075\text{ cm}^{-1}$ , large bands between  $750\text{--}820\text{ cm}^{-1}$  assigned to be Si-O-CH<sub>3</sub> stretching[20, 21] and a strong characteristic band of O-CH<sub>3</sub> near  $1187\text{ cm}^{-1}$  [20]. In addition, the two main sharp absorption peaks which appeared at  $2836$  and  $2937\text{ cm}^{-1}$ , are ascribed respectively to the asymmetric and symmetric C-H stretching modes of the -CH<sub>2</sub> groups on the GPTS organosilanes monomers.

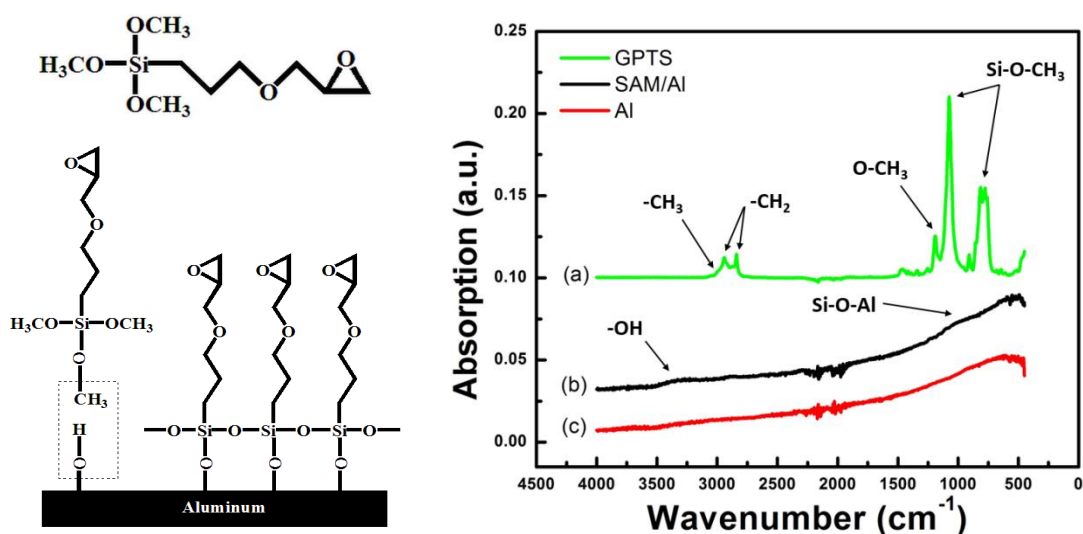


Figure 6. 1 Left-top shows the GPTS molecule, left-down shows the self-assembled monolayer (SAM) of GPTS on Al substrate. Right of Figure 6.1 shows ATR-FTIR spectra of (a) pure GPTS organosilanes (b) SAM of GPTS on aluminum substrate (SAM/Al) and (c) Al substrate

Additionally, a very small peak at  $2956\text{ cm}^{-1}$  is present in the spectrum due to the asymmetric in-plane C-H stretching mode of the  $-\text{CH}_3$  group of the same molecules [22]. Figure 6.1 (b) and (c) show the ATR-FTIR spectra of SAM/Al and Al substrates, respectively. Both the spectra show a shallow, broad peak between  $3000\text{-}3500\text{ cm}^{-1}$ , which is assigned to -OH bonds on the Al substrates due to the NaOH etching [23, 24]. Interestingly, the SAM/Al substrate shows a shallow and broad peak at  $750\text{-}1200\text{ cm}^{-1}$ , as a result of Si-O-Al stretching of GPTS as a SAM on Al substrate.

Figure 6.2 shows the images of scanning electron microscopy (SEM) and spectra of energy dispersive x-ray (EDX) analysis of the Al and SAM/Al substrates. The SEM images of the Al (Figure 6.2(a)) and SAM/Al substrates (Figure 6.2(c)) do not show any differences as the thickness or agglomeration of SAM on a surface are in the nanometer scale, and normally were studied by the atomic force microscope (AFM) [7]. Figure 6.2(b) and (d) show the EDX spectra of the Al and SAM/Al substrates, respectively. Both the spectra are dominated by Al  $\text{K}_\alpha$  peaks, found at  $1.48\text{ keV}$  due to the Al substrate and at  $2.1\text{ keV}$  due to Au  $\text{L}_\alpha$ , as a gold coating was used to minimize the charging due to the interaction of electrons with the insulated surface. It is to mention that no substantial increase of peak intensities related to C  $\text{K}_\alpha$  at  $0.28\text{ keV}$  and O  $\text{K}_\alpha$  at  $0.5\text{ keV}$  are visible in the spectra of SAM/Al (Figure 6.2(d)) when compared to Al (Figure 6.2(b)). Interestingly, a tiny peak appeared at  $1.74\text{ keV}$ , and may be due to the Si  $\text{K}_\alpha$  from the GPTS molecules (Figure 6.1) as SAM on Al substrates.

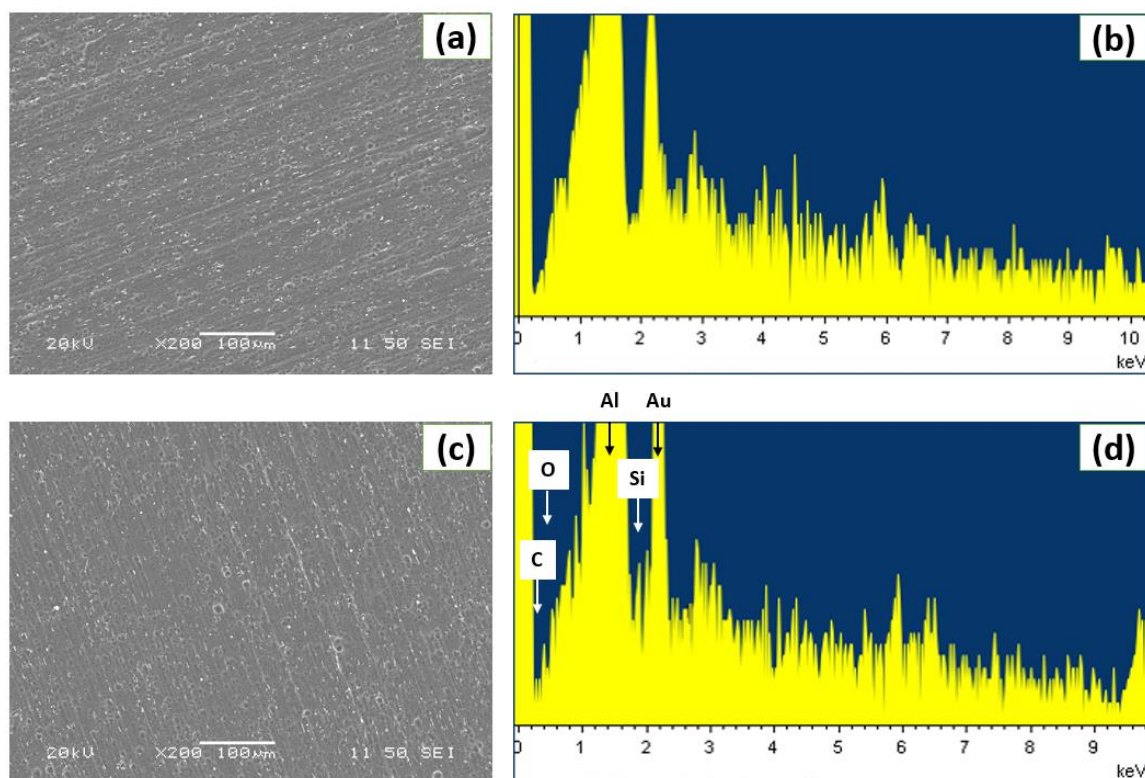


Figure 6. 2 SEM images of (a) Al and (c) SAM/Al substrate; EDX spectra of (b) Al and (d) SAM/Al substrate

Figure 6.3 illustrates the Nyquist plots as well as the electrical equivalent circuits for the EIS data from the Al and SAM/Al substrates in various immersion time in the conducting electrolyte, which is a diluted NaOH solution. Specifically, Figure 6.3 (a) and (b) show the Nyquist plots, which present the real component of impedance ( $Z_{\text{real}}$  or  $Z'$ ) versus the imaginary component ( $Z_{\text{imaginary}}$  or  $Z''$ ) on a linear scale, of the Al and SAM/Al substrates. The EIS results for the immersion times of 2, 4, 6, 8 and 10 h have been given in this manuscript. It is to mention that the OCP was monitored continuously between two consecutive EIS measurements. The Nyquist plots of the Al shown in Figure 6.3(a), indicate that the charge transfer resistance ( $R_{\text{ct}}$ ) (the diameter of the semi-circle) increases with the increase of the immersion time and stabilizes after a certain

time. This is due to the reaction of aluminum with NaOH and the formation of  $\text{Al(OH)}_3$  or  $\text{AlO}_x$  at the surface of the aluminum [25]. In our experiment it is found that six hours is sufficiently long enough to form a protective oxide or hydroxide layer on aluminum that provides a  $R_{ct}$  value of  $83.3 \text{ k}\Omega \text{ cm}^2$ . Any further increase in the immersion time does not increase the  $R_{ct}$  value on aluminum in the dilute NaOH solution. Figure 6.3(b) shows the  $R_{ct}$  of GPTS coated aluminum (SAM/Al) in various immersion times. The derived values of  $R_{ct}$  from the Nyquist plots show very similar tendencies for both the SAM/Al and Al substrates. Figure 6.3(c and d) provide the comparison of the  $R_{ct}$  values of both Al and SAM/Al substrates. It is found that the  $R_{ct}$  values of SAM/Al are always larger than that of the  $R_{ct}$  of Al for the immersion times of 2h and 10h. The larger values of  $R_{ct}$  for the SAM/Al substrate compared to the Al substrate are due to the presence of GPTS molecules on Al that behaves as a barrier against charge transfer at the interface of the liquid and solid surfaces of the SAM/Al substrates. Therefore, the relatively large value of  $R_{ct}$  in the SAM/Al substrate found when compared to the Al substrate confirms the presence of GPTS indirectly by EIS. An electrical equivalent circuit for Al and SAM/Al substrates is presented in Figure 6.3(e) and the derived components are presented in Table 6.1. In addition to studying the EIS, the OCP was also monitored with the immersion time. Figure 6.3(f) illustrates the variation of the open circuit potential (OCP) of the Al and SAM/Al substrates. It can be observed that the OCP values of the SAM/Al substrate were always positive when compared to the Al substrate. The average potential difference is found to be positive with a value of  $+106 \pm 33 \text{ mV}$  for SAM/Al with respect to the Al



substrate during the 10 hrs of immersion time. This increase of potential signifies the presence of GPTS molecules as a SAM on the Al substrate.

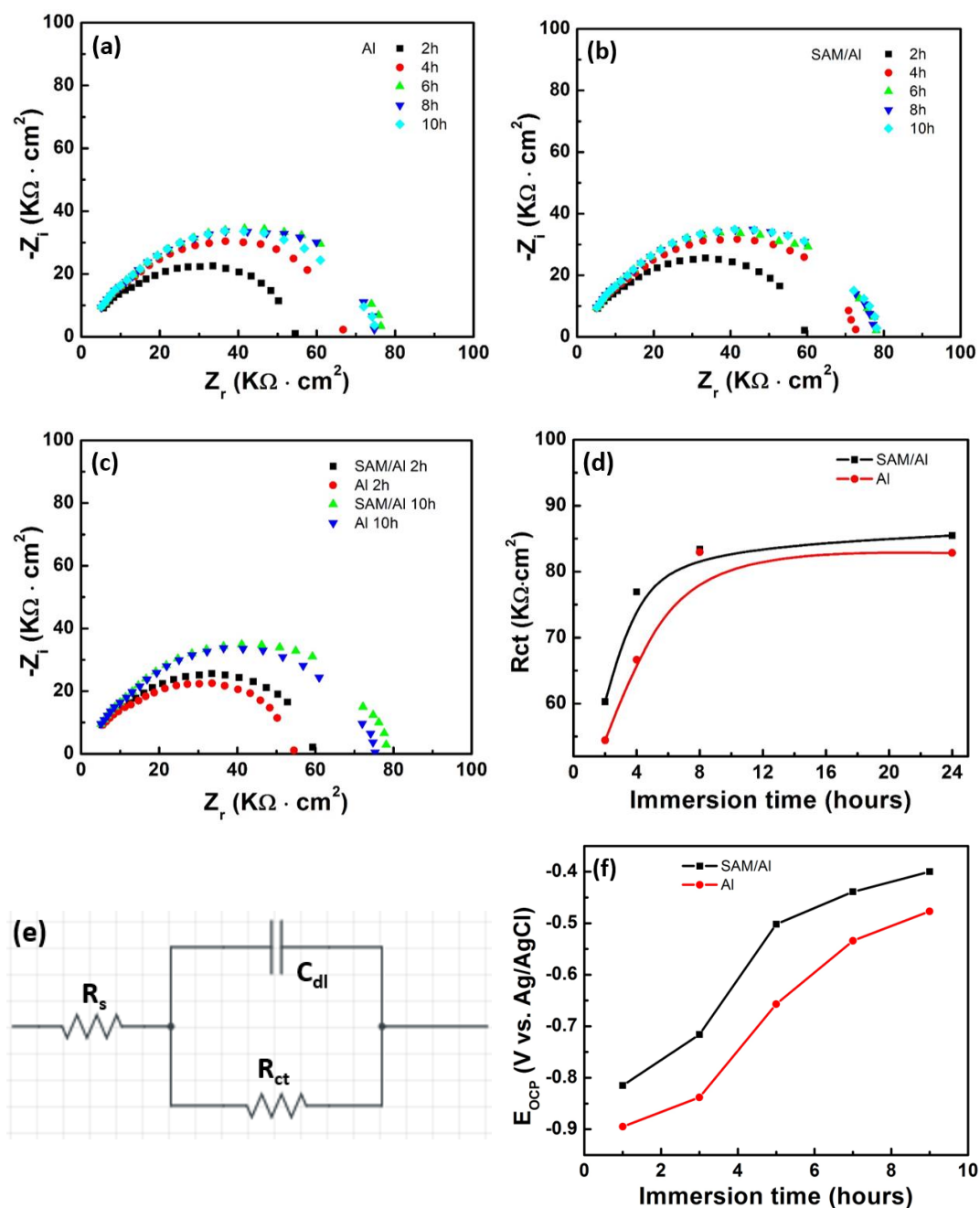


Figure 6. 3 (a-c) Nyquist plots for Al and SAM/Al substrates after immersion time in 10-4M NaOH aqueous solution of 2, 4, 6, 8, 10h respectively; (d) Charge transfer resistance ( $R_{ct}$ ) of Al and SAM/Al substrates as functions of immersion

time; (e) Electrical equivalent circuit model used for fitting of EIS dates of Al and SAM/Al substrates; (f) The variation of open circuit potential (OCP) with immersion time for Al and SAM/Al substrates

Figure 6.4 shows the potentiodynamic polarization curves of the Al and SAM/Al substrates immersed in the NaOH solution for 10hrs as we have used earlier [24, 26]. The corrosion current density ( $I_{corr}$ ) and corrosion potential ( $E_{corr}$ ) were calculated from the intersection point by extrapolating the anodic and cathodic curves. The polarization resistance ( $R_p$ ) was calculated by the Stern-Geary equation as given by

$$R_p = \frac{\beta_a \beta_c}{2.3 I_{corr} (\beta_a + \beta_c)} \quad (6.1)$$

where  $\beta_a$  and  $\beta_c$  are the anodic and cathodic Tafel slopes, respectively.

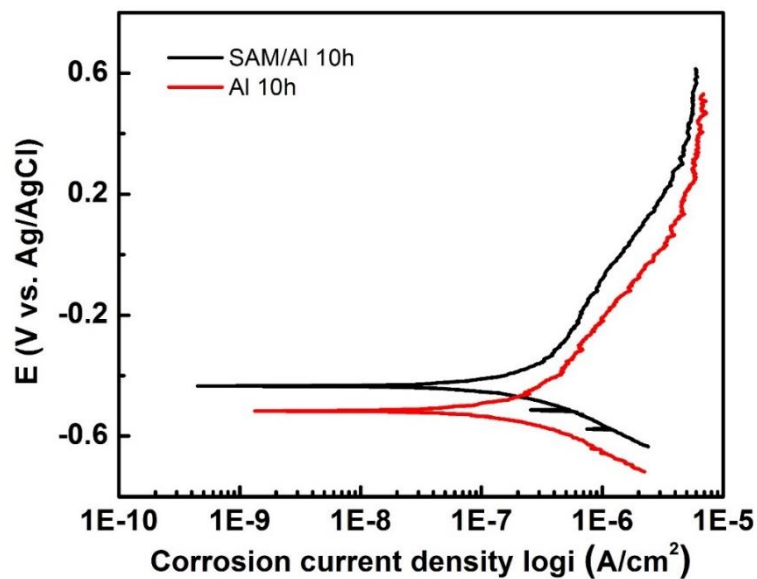


Figure 6. 4 Potentiodynamic polarization curves of Al and SAM/Al substrates after 10 h immersion time in  $10^{-4}$  M NaOH aqueous solution

Table 6. 1 Results of EIS and potentiodynamic polarization of Al and SAM/Al substrates after the immersion time of 10 hrs in  $10^{-4}$  M NaOH solution

<b>Systems</b>	<b>R<sub>s</sub></b> (kΩ . cm <sup>2</sup> )	<b>R<sub>ct</sub></b> (kΩ . cm <sup>2</sup> )	<b>C<sub>dl</sub></b> (pF/cm <sup>2</sup> )	<b>E<sub>corr</sub></b> (mV)	<b>I<sub>corr</sub></b> (μA/cm <sup>2</sup> )	<b>R<sub>p</sub></b> (kΩ . cm <sup>2</sup> )
<b>Al</b>	2.8	70	144	-520	81.1	203.3
<b>SAM/Al</b>	2.8	84	134	-438	79.9	207.6

The corrosion currents are found to be 81.1 and 79.9  $\mu\text{A}/\text{cm}^2$  for the Al and SAM/Al substrates, respectively. Similarly, the corrosion potentials are observed to be -520 mV and -438 mV for the Al and SAM/Al substrates, respectively. It is to mention that no substantial gain in the corrosion current due to the presence of SAM on Al is noticed. On the other hand, a large gain in corrosion potential is observed in the case of SAM/Al as compared to Al. The relatively higher values of corrosion potential of SAM/Al as compared to Al signifies the presence of SAM of GPTS on the Al surface. In the literature, it has been shown that the self-assembled monolayer can be used as a substitute of chromate conversion coatings to protect the metal substrates [6].

### 6.1.4 Summary

Self-assembled monolayers of GPTS were successfully fabricated on aluminum substrates by spin coating of GPTS organosilane monomer solutions. The model of chemical reaction of GPTS organosilane molecules with NaOH etched Al substrate

demonstrates the formation of SAM on Al. The presence of a tiny peak of Si  $K_{\alpha}$  in the EDX spectrum as well as the observation of a shallow peak of Si–O–Al stretching in the ATR-FTIR spectrum of SAM/Al substrate directly confirm the presence of GPTS organosilane molecules as SAM on Al substrate. EIS studies indirectly complement the formation of SAM on aluminum as the presence of an electrical barrier layer, which controls the charge transfer by increasing the charge transfer resistance ( $R_{ct}$ ) as well as the open circuit potential (OCP) of the SAM/Al substrate. Further works are underway using more surface sensitive techniques such as AFM and XPS to understand the formation of SAM of GPTS on Al substrates.

## 6.2 Mechanical durability test of superhydrophobic coatings on SAM modified aluminum substrates

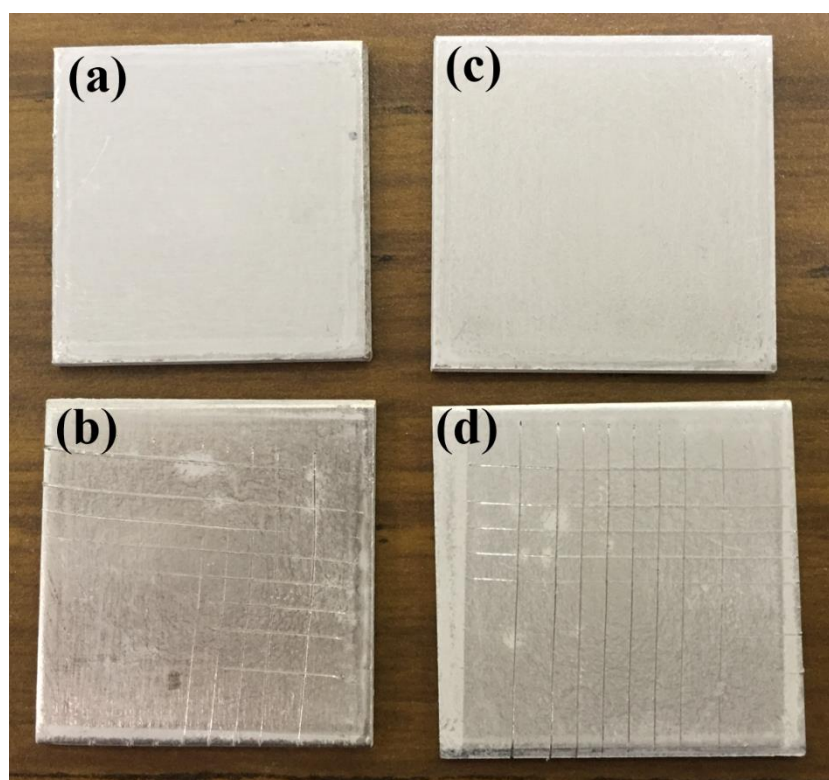


Figure 6. 5 Optical photographs of superhydrophobic PMHS/TiO<sub>2</sub> coatings on as-

received aluminum substrates (a) before and (b) after adhesive tape tests; on SAM modified aluminum substrates (c) before and (d) after adhesive tape tests

It should be mentioned that the mechanical properties of the superhydrophobic coatings are very significant for their applications against surface erosion, friction as well as corrosion protection[27, 28]. The typical hardness of the superhydrophobic coatings varies in the range of 2H to 9H and their adhesion strength is approximately 5B [27-30]. Following the American Standard Test Method (ASTM) D 3359-02, the Adhesion test of PMHS/TiO<sub>2</sub> superhydrophobic surface both on as-received aluminum and SAM modified aluminum surface were carried out carefully. The test results for them were found to be 0-2B. However, a little improvement on adhesion force could be detected by comparing the surfaces on as-received aluminum and SAM modified aluminum substrates after the removal of adhesive tape, as shown in Figure 6.5. Adhesion test is used to test the adhesion force between the superhydrophobic coatings with the substrates. The method used mostly for the test is according to American Standard Test Method (ASTM) D 3359-02 which is recognized worldwide. There are two methods described in this ASTM Specification. One is to make an X-cut pattern, which is primarily intended for use at job sites. After an X-cut is made through the film to the substrate, pressure-sensitive tape is applied over the cut and then removed, and adhesion is assessed qualitatively on the 0 to 5 scale. Another is to make a crosshatch pattern, which is more suitable for use in the laboratory but not suitable for films thicker than 125 $\mu$ m. Here, we mainly discuss about the latter one. The test process is depicted

as follow: A crosshatch pattern is made through the film to the substrate. Square grids with a side length of 1mm are cut on the coated substrate with a steel blade. Detached flakes of coating are removed by brushing with a soft brush. Pressure-sensitive tape is applied over the crosshatch cut. Tape is smoothed into place by using a pencil eraser or hand over the area of the incisions. Tape is removed by pulling it off rapidly back over itself as close to an angle of 180 °. It is to mention, there is still a lot of effort to devote on this topic before turning this technique into practical applications.

## Reference

- [1] Schreiber F. Structure and growth of self-assembling monolayers. *Progress in Surface Science*. 2000;65:151-256.
- [2] Chauhan AK, Aswal DK, Koiry SP, Gupta SK, Yakhmi JV, Sürgers C, et al. Self-assembly of the 3-aminopropyltrimethoxysilane multilayers on Si and hysteretic current–voltage characteristics. *Applied Physics A*. 2007;90:581-9.
- [3] Vashist SK, Lam E, Hrapovic S, Male KB, Luong JH. Immobilization of antibodies and enzymes on 3-aminopropyltriethoxysilane-functionalized bioanalytical platforms for biosensors and diagnostics. *Chemical reviews*. 2014;114:11083-130.
- [4] Ulman A. Formation and Structure of Self-Assembled Monolayers. *Chemical reviews*. 1996;96:1533-54.
- [5] Chen L, Yang B, Zhang J. Preparation and tribological properties of polymer film covalently bonded to silicon substrate via an epoxy-terminated self-assembled monolayer. *Journal of Adhesion Science and Technology*. 2014;28:1725-38.
- [6] Reis FM, de Melo HG, Costa I. EIS investigation on Al 5052 alloy surface preparation for self-assembling monolayer. *Electrochimica Acta*. 2006;51:1780-8.
- [7] Igor Luzinov DJ. Epoxy-Terminated Self-Assembled Monolayers: Molecular Glues for Polymer Layers *Langmuir*. 2000;16:504-16.
- [8] Cho WK, Park S, Jon S, Choi IS. Water-repellent coating: formation of polymeric self-assembled monolayers on nanostructured surfaces. *Nanotechnology*. 2007;18:395602.
- [9] Sugimura H, Hozumi A, Kameyama T, Takai O. Organosilane self-assembled monolayers formed at the vapour/solid interface. *Surface and Interface Analysis*. 2002;34:550-4.
- [10] Song X, Zhai J, Wang Y, Jiang L. Self-assembly of amino-functionalized monolayers on silicon surfaces and preparation of superhydrophobic surfaces based on alkanolic acid dual layers and surface

- roughening. *Journal of colloid and interface science*. 2006;298:267-73.
- [11] Siddaramanna A, Saleema N, Sarkar DK. A versatile cost-effective and one step process to engineer ZnO superhydrophobic surfaces on Al substrate. *Applied Surface Science*. 2014;311:182-8.
- [12] Pan C, Shen L, Shang S, Xing Y. Preparation of superhydrophobic and UV blocking cotton fabric via sol-gel method and self-assembly. *Applied Surface Science*. 2012;259:110-7.
- [13] Brassard JD, Sarkar DK, Perron J. Synthesis of monodisperse fluorinated silica nanoparticles and their superhydrophobic thin films. *ACS applied materials & interfaces*. 2011;3:3583-8.
- [14] Saleema N, Sarkar DK, Paynter RW, Gallant D, Eskandarian M. A simple surface treatment and characterization of AA 6061 aluminum alloy surface for adhesive bonding applications. *Applied Surface Science*. 2012;261:742-8.
- [15] Zhang Q. Boundary Lubrication and Surface Mobility of Mixed Alkylsilane Self-Assembled Monolayers. *J Phys Chem B*. 2003;107:13123-32.
- [16] Zhang Q. Interfacial Friction of Surfaces Grafted with One- and Two-Component Self-Assembled Monolayers. *Langmuir*. 2005;21:5405-13.
- [17] Moores B. AFM-assisted fabrication of thiol SAM pattern with alternating quantified surface potential. *Nanoscale Research Letters*. 2011;6.
- [18] Wang F, Xu J, Luo H, Wang J, Wang Q. A new organofunctional ethoxysilane self-assembly monolayer for promoting adhesion of rubber to aluminum. *Molecules*. 2009;14:4087-97.
- [19] Telegdi J. Inhibition of Copper Corrosion by self Assembled Amphiphiles. *Chem Biochem Eng Q*. 2007;21:77-82.
- [20] Yuan W. Characterization of Organofunctional Silane Films on Zinc Substrates. *Journal of colloid and interface science*. 185:197-209.
- [21] Eaton P, Holmes P, Yarwood J. In situ and ex situ FTIR-ATR and Raman microscopic studies of organosilane hydrolysis and the effect of hydrolysis on silane diffusion through a polymeric film. *Journal of Applied Polymer Science*. 2001;82:2016-26.
- [22] Damia C, Sarda S, Deydier E, Sharrock P. Study of two hydroxyapatite/poly(alkoxysilane) implant coatings. *Surface and Coatings Technology*. 2006;201:3008-15.
- [23] Saleema N, Sarkar DK, Gallant D, Paynter RW, Chen XG. Chemical nature of superhydrophobic aluminum alloy surfaces produced via a one-step process using fluoroalkyl-silane in a base medium. *ACS applied materials & interfaces*. 2011;3:4775-81.
- [24] Huang Y, Sarkar DK, Grant Chen X. Superhydrophobic aluminum alloy surfaces prepared by chemical etching process and their corrosion resistance properties. *Applied Surface Science*. 2015;356:1012-24.
- [25] Ahmad Z. CHAPTER 2 - BASIC CONCEPTS IN CORROSION. *Principles of Corrosion Engineering and Corrosion Control*. Oxford: Butterworth-Heinemann; 2006. p. 50-2.
- [26] Huang Y, Sarkar DK, Gallant D, Chen XG. Corrosion resistance properties of superhydrophobic copper surfaces fabricated by one-step electrochemical modification process. *Applied Surface Science*. 2013;282:689-94.
- [27] Kumar D, Wu X, Fu Q, Ho JWC, Kanhere PD, Li L, et al. Development of durable self-cleaning coatings using organic-inorganic hybrid sol-gel method. *Applied Surface Science*. 2015;344:205-12.

- [28] Xu QF, Wang JN, Sanderson KD. A general approach for superhydrophobic coating with strong adhesion strength. *Journal of Materials Chemistry*. 2010;20:5961.
- [29] Lakshmi RV, Bharathidasan T, Basu BJ. Superhydrophobic sol-gel nanocomposite coatings with enhanced hardness. *Applied Surface Science*. 2011;257:10421-6.
- [30] Geng Z, He J, Yao L. Fabrication of robust high-transmittance superamphiphobic coatings through dip-coating followed by spray-coating. *RSC Adv*. 2015;5:89262-8.



## 7. Conclusions

In conclusion, the work presented in this thesis provides several effective approaches for the fabrication of durable superhydrophobic coatings, while considering the aspects of anti-corrosion and UV durability, on aluminum substrates. Furthermore, efforts have been made to fabricate mechanically durable superhydrophobic coatings by depositing a self-assembled monolayer on aluminum substrates. These results will contribute to a better understanding of superhydrophobic phenomena and are expected to realize a wide application of superhydrophobic surfaces in the industrial world.

1. Corrosion resistant superhydrophobic cobalt stearate coatings were successfully fabricated on aluminum substrates via a simple, environment-friendly electrodeposition process in an ethanolic solution containing stearic acid and cobalt nitrate. It was found that the surface morphology, composition and wetting properties varied according to the molar ratio of Co/SA in the electrolyte. The optimum superhydrophobic surface was obtained from the cathodic aluminum substrate in the mixed solution with a Co/SA molar ratio of 0.2, with a maximum contact angle of  $161^\circ$  and a largest polarization resistance of  $1591 \text{ k}\Omega \text{ cm}^2$ .

2. UV durable superhydrophobic coatings have been fabricated using two different approaches. Initially, a simple and low-cost method was developed to fabricate UV durable superhydrophobic cobalt stearate coatings on aluminum alloy substrates simply by one-step electrodeposition in a mixed ethanolic solution containing cobalt nitrate and stearic acid. This non-fluorine superhydrophobic surface demonstrated

excellent UV resistance properties during the accelerated UV degradation test with no change in wettability, morphology or chemical compositions as confirmed by the contact angle test, SEM as well as ATR-FTIR, respectively.

3. Furthermore, inspired by the UV durable properties of cobalt stearate, another UV durable superhydrophobic nanocomposite coating has been fabricated simply by embedding CoSA-coated TiO<sub>2</sub> nanoparticles in a hydrophobic polymethylhydro-siloxane matrix on AA6061 aluminum substrates. When compared to the dramatically decreased water contact angle on the PMHS/TiO<sub>2</sub> surfaces, the PMHS/TiO<sub>2</sub>@CoSA superhydrophobic coatings exhibited a nearly constant water contact angle of 160° under continuous UV irradiation for 1 month. Our synthesized cobalt stearate not only increased the hydrophobicity of the TiO<sub>2</sub> nanoparticle surface, but also confined the photocatalytic efficiency of TiO<sub>2</sub> when it was decomposed to cobalt oxide. A plausible model has been suggested to explain the UV durable mechanism of superhydrophobic TiO<sub>2</sub> coatings. These promising results suggest that UV-durable superhydrophobic coatings incorporating TiO<sub>2</sub> nanoparticles can be utilized in wide practical applications e.g. non-wetting UV shield.

4. Self-assembled monolayers of GPTS were successfully fabricated on aluminum substrates by spin coating of GPTS organosilane monomer solutions. The model of chemical reaction of GPTS organosilane molecules with NaOH etched Al substrate demonstrates the formation of SAM on Al. The presence of a tiny peak of Si K $\alpha$  in the EDX spectrum as well as the observation of a shallow peak of Si–O–Al stretching into the ATR-FTIR spectrum of SAM/Al substrate directly confirm the

presence of GPTS organosilane molecules as SAM on Al substrate. EIS studies indirectly complement the formation of SAM on aluminum as the presence of an electrical barrier layer, which controls the charge transfer by increasing the charge transfer resistance ( $R_{ct}$ ) as well as the open circuit potential (OCP) of the SAM/Al substrate.

5. In order to improve the mechanical properties of the superhydrophobic surfaces, superhydrophobic PMHS/TiO<sub>2</sub> coatings were fabricated on SAM modified aluminum substrates. Following the American Standard Test Method (ASTM) D 3359-02, the Adhesion test of superhydrophobic PMHS/TiO<sub>2</sub> surfaces both on as-received aluminum and SAM modified aluminum surface were carried out carefully. The test results for both of them are found to be 2B. Some improvements on adhesion force could be detected by comparing the surfaces on as-received aluminum and SAM modified aluminum substrates after the removal of adhesive tape.

## 8. Recommendations

In the present project, durable superhydrophobic coatings have been fabricated using different methods including electrodeposition, sol-gel, self-assembled monolayer *etc.* Many interesting results have been obtained, but there are still some suggestions to put forward for further research, as shown below:

1. To better protect aluminum from chemical corrosion, the aluminum substrates can be pretreated with an anodization process or passivated with self-assembled silanes before the fabrication of a cobalt stearate (CoSA) film by electrodeposition.

2. In the study of UV durable superhydrophobic coatings, the molar ratio of CoSA/TiO<sub>2</sub> could be an interesting parameter to analyze in future research, which might affect the longevity of PMHS/TiO<sub>2</sub>@CoSA superhydrophobic coatings.

3. Self-assembled monolayer (SAM) was utilized to improve the mechanical durability and the adhesion force between the substrates and coatings. The results of 2B were not perfect. Progress could be made by reducing the thickness of the superhydrophobic coatings or increasing the density of SAM on the aluminum substrates.

## 9. Publications & Awards

### Scientific papers:

1. Electrochemical impedance spectroscopy (EIS) studies of self-assemble monolayers (SAM) on aluminum substrates (**Paper ID #: IMPC16-1021. Quebec city, 2016**, as an oral presentation and conference paper)
2. Ultraviolet-durable superhydrophobic nanocomposite thin films based on cobalt stearate-coated TiO<sub>2</sub> nanoparticles (submitted to *ACS applied materials & interfaces*)
3. Corrosion resistant properties of electrodeposited superhydrophobic cobalt stearate thin films on aluminum (submitted to *Applied surface science*)

### Posters:

4. Fabrication of superhydrophobic PMHS/TiO<sub>2</sub> coatings on Al and its behaviors in the UV lights **#poster, JER 2015**
5. UV durable superhydrophobic nanocomposite thin films on aluminium **#poster, JER2016**

### Awards:

6. The scholarship of the Québec Bursary Granting Exemption from Differential Tuition Fees
7. The scholarship awarded by X. Grant Chen, the Professor and NSERC chairholder
8. Fonds des étudiants REGAL 2016-2017
9. The prize for the best poster, on the 13<sup>th</sup> Journée des étudiants du REGAL 2016